

# Thermodynamics of mantle minerals – II. Phase equilibria

Lars Stixrude and Carolina Lithgow-Bertelloni

Department of Earth Sciences, University College London, London, United Kingdom. E-mail: l.stixrude@ucl.ac.uk

Accepted 2010 November 12. Received 2010 November 3; in original form 2010 May 4

## SUMMARY

We complete the development and description of a thermodynamic method for the computation of phase equilibria and physical properties of multiphase mantle assemblages. Our previous paper focused on the computation of physical properties. In this paper, our focus shifts to the phase equilibria. We further develop our theory to specify the ideal and excess contributions to solution properties and derive properties of multiphase assemblages. We discuss our global inversion strategy for determining the values of the free parameters in our theory and compare inverted parameter values with expectations based on scaling arguments. Comparisons between our method and experimental phase equilibria data encompass the pressure–temperature regime of Earth’s mantle. Finally, we present applications of our method that illustrate how it may be used to explore the origins of mantle structure and mantle dynamics. Continuing rapid advances in experimental and theoretical petrology and mineral physics have motivated an expansion of the scope of our model via the addition of several new phases, and of the soda component: an appendix lists all parameters in our model and references to the experimental and theoretical studies that constrain them. Our algorithm for global minimization of the Gibbs free energy is embodied in a code called HeFESTo, and is detailed in a second appendix.

**Key words:** Composition of the mantle; Elasticity and anelasticity; Equations of state; High-pressure behaviour; Phase transitions; Planetary interiors.

## 1 INTRODUCTION

Central to the goals of geophysics is an elucidation of the ways in which material behaviour governs planetary processes. Differentiation into crust, mantle and core, dynamics, thermal evolution and the generation of magnetic fields, are all controlled by the physical properties and phase equilibria of planetary materials. Material properties are the essential link between geophysical observation and the evolution of the interior: elastic wave propagation provides us with a rich source of information on interior structure, which may be related to the thermal and chemical state via knowledge of material properties.

Thinking of a planet as an experimental sample emphasizes the relationship between planetary processes and material behaviour via properties that control its response to natural perturbations. We may explore the response of the planet to a sudden increase in energy, provided, for example, by a giant impact of the type that is thought to have formed Earth’s moon (Canup 2004). Responses include an increase in temperature, controlled by the heat capacity, a decrease in density controlled by the thermal expansivity, and phase transformations controlled by the free energy. Phase transformations also contribute to changes in temperature and density via the heats and volumes of transformation. A giant impact also perturbs the stress state, to which the planet responds via compression (controlled by the bulk modulus), adiabatic heating (Grüneisen

parameter) and phase transformations (free energy). Internal dynamics, as manifested for example in mantle convection, are driven by lateral variations in the density that are linked to the thermal state via the thermal expansivity and heat capacity.

As experimental samples, planets present several challenges to thermodynamic description, including the extreme conditions of their interiors, and their heterogeneity, which exists over a wide range of length scales. In Earth’s mantle there are at least 6 essential chemical components ( $\text{SiO}_2$ ,  $\text{MgO}$ ,  $\text{FeO}$ ,  $\text{CaO}$ ,  $\text{Al}_2\text{O}_3$  and  $\text{Na}_2\text{O}$ ), that stabilize a large number of distinct and impure phases over the entire mantle pressure–temperature regime (Akaogi & Akimoto 1979; Irifune *et al.* 1986). The multiphase nature of the mantle is central to our understanding of its structure and dynamics: for example, in the transition zone, gravitational self-compression is accommodated mostly by solid–solid phase transformations. Many phase transformations occur over sufficiently narrow intervals of pressure that they are seismically reflective; the comparison of the depth of these reflectors to the pressure of phase transformations gives us one of our most powerful constraints on the composition of the deep interior. Because the pressure at which they occur depends on temperature, phase transformations may also contribute to laterally heterogeneous structure and influence mantle dynamics (Anderson 1987; Christensen 1995). Understanding planetary processes then demands a method that is able to interpolate among and extrapolate from the necessarily limited results of experiment

or first principles theory to the full chemical richness that is typical of silicate mantles.

The focus here is on thermodynamic equilibrium. Equilibrium is a reasonable assumption for many planetary processes because of the large temperature characteristic of planetary interiors. For example, thermodynamic equilibrium has proved to be a powerful means by which to understand mantle structure, the influence of phase transformations on dynamics, and the structure of exo-planets (Ringwood 1991; Christensen 1995; Valencia *et al.* 2006). Many important material properties lie beyond our scope including transport properties such as viscosity and diffusion. We note however, that thermodynamic equilibrium provides a basis for understanding these properties as well, insofar as thermodynamic equilibrium largely determines which phases are stable at a given pressure and temperature, and the transport properties of different phases may differ substantially. For example, the transformation from perovskite to post-perovskite may be accompanied by a large change in viscosity (Ammann *et al.* 2010), and garnet is expected to weaken with increasing majorite content (Hunt *et al.* 2010). Gibbs free energy differences computed by equilibrium thermodynamic models are also a foundation of theories of the kinetics of phase transformations that may be important in a number of processes including attenuation within phase coexistence loops (Li & Weidner 2008; Ricard *et al.* 2009) and the preservation of subducted metastable wedges (Kubo *et al.* 2009).

Our goal, beginning with our previous paper (Stixrude & Lithgow-Bertelloni 2005b) hereafter referred to as Paper I, has been to construct an equilibrium thermodynamic theory capable of self-consistent computation of phase equilibria and physical properties of mantle assemblages, including those most important for understanding dynamic processes and geophysical observations. Here we continue our description of a method that meets our goal. The method is complementary to experiment and first principles theory and uses results on simple systems to build up predictive power for more complex assemblages that are most relevant to understanding planets. In Paper I, we focused on the computation of physical properties. In this paper, we complete the theory, and shift our focus to phase equilibria: we specify the solution model and derive properties of multiphase assemblages. We discuss our global inversion strategy for determining the values of the free parameters in the theory and compare inverted parameter values with expectations based on scaling arguments. Comparisons between our method and experimental phase equilibria data encompass the pressure regime of Earth's mantle. Finally, we present applications of our method that illustrate how it may be used to explore the origins of mantle structure and mantle dynamics.

We have applied an earlier form of our method to understanding mantle structure and dynamics (Stixrude & Lithgow-Bertelloni 2005a; Stixrude & Lithgow-Bertelloni 2007; Xu *et al.* 2008; Cammarano *et al.* 2009), as have other groups (Khan *et al.* 2006; Cobden *et al.* 2008; Nakagawa *et al.* 2009). This paper describes the theory completely, which was not possible in these applications papers, and introduces a better solution model and Landau contributions. Moreover, continuing rapid advances in experimental and theoretical petrology and mineral physics have motivated an expansion of the scope of our model via the addition of several new phases, particularly those relevant to the core–mantle boundary and to the shallowest mantle, and of the soda component: an appendix lists all parameters in our model and references to the experimental and theoretical studies that constrain them. Our algorithm for global minimization of the Gibbs free energy is embodied in a code called HeFESTo, and is detailed in a second appendix.

## 2 OUR APPROACH AND PREVIOUS WORK

There have been many previous studies of aspects of mantle thermodynamics, but none that meet our goal of self-consistent computation of phase equilibria and geophysically relevant physical properties. Previous studies may be divided into two groups based on their primary motivations. In the first group are those focusing primarily on mantle phase equilibria. A complete review is beyond the scope of this paper as there have been many important contributions (Helgeson *et al.* 1978; Wood & Holloway 1984; Berman 1988; Fei *et al.* 1990; Stixrude & Bukowski 1993; Saxena 1996; Gottschalk 1997; Bina 1998; Chatterjee *et al.* 1998; Holland & Powell 1998; Fabrichnaya 1999; Matas 1999; Ricard *et al.* 2005; Jacobs & de Jong 2007; Piazzoni *et al.* 2007; Ganguly *et al.* 2009). Considerations of physical properties in these studies have typically been limited in scope, for example they do not include a self-consistent account of the elastic constant tensor other than the bulk modulus. In the second group are those studies focusing primarily on the physical properties of mantle phases. Syntheses of the physical properties of mantle phases, including their elasticity, typically do not permit computation of phase equilibria (Bass & Anderson 1984; Weidner 1985; Duffy & Anderson 1989). As determinations of the elastic structure of Earth's interior improve, there has been increasing interest in the development of methods that can relate seismic observations to the properties of multiphase assemblages. Several so-called hybrid models have appeared, in which a model of physical properties is combined with a description of phase equilibria from another source (Ita & Stixrude 1992; Cammarano *et al.* 2003; Hacker *et al.* 2003). An important disadvantage of these models is that they are not self-consistent. Our method, beginning with Paper I, overcomes these limitations of previous approaches to mantle thermodynamics as illustrated by application of earlier forms of the theory (Stixrude & Lithgow-Bertelloni 2005a; Khan *et al.* 2006; Stixrude & Lithgow-Bertelloni 2007; Cobden *et al.* 2008; Xu *et al.* 2008; Cammarano *et al.* 2009; Nakagawa *et al.* 2009).

Our approach makes use of the following four thermodynamic principles. Except for the last, which was introduced in Paper I, these principles are not new; it is their combination that we have found to be especially powerful in meeting our goal.

(i) *Fundamental thermodynamic relations:* A fundamental thermodynamic relation is a single functional relationship that contains complete information of all equilibrium properties of all equilibrium states of a system (Callen 1960). All thermodynamic properties are computed as derivatives of the fundamental relation with respect to its natural variables, guaranteeing self-consistency. For example

$$\frac{\partial^3 \mathcal{G}}{\partial P \partial P \partial T} = \frac{\partial^3 \mathcal{G}}{\partial T \partial P \partial P} = \frac{\partial}{\partial P} (V\alpha)_T = -\frac{\partial}{\partial T} \left( \frac{V}{K} \right)_P, \quad (1)$$

where  $\mathcal{G}$  is the Gibbs free energy,  $P$  is pressure,  $T$  is temperature,  $V$  is volume,  $\alpha$  is thermal expansivity and  $K$  is the isothermal bulk modulus. We write the fundamental relation in analytic form with analytically computable derivatives so that relations of this type are satisfied exactly. Another example of self-consistency is illustrated by the Clapeyron relation

$$\Gamma = \left( \frac{\partial P}{\partial T} \right)_{\text{eq}} = \frac{\Delta V}{\Delta S}, \quad (2)$$

where  $\Gamma$  is the Clapeyron slope, the subscript eq indicates equilibrium coexistence and  $\Delta$  indicates the finite change in properties across the transition. Most previous studies of mantle phase equilibria have satisfied thermodynamic self-consistency, although at least

one violates the Maxwell relations (Sobolev & Babeyko 1994), and the Clapeyron relation is violated by so-called hybrid methods (Ita & Stixrude 1992; Cammarano *et al.* 2003; Hacker *et al.* 2003). Self-consistency is important because  $\Delta V$  and  $\Delta S$  may change substantially over the mantle pressure–temperature regime, introducing significant curvature to phase boundaries, especially in the deep mantle. There are practical advantages as well: because so many thermodynamic quantities are intimately linked, diverse experimental and first principles results can be used independently to constrain more robustly the thermodynamic model. For example, phase equilibria, lattice parameter, and acoustic velocity data all constrain the volume of a phase, placing redundant constraints on the equation of state.

(ii) *Legendre transformations*: While the Gibbs free energy is the natural thermodynamic potential for treating phase equilibria, the Helmholtz free energy is much more useful for describing physical properties. Legendre transformations provide a simple way of moving from one thermodynamic potential to another (Callen 1960; Alberty 2001). We formulate our fundamental thermodynamic relation in terms of the Helmholtz free energy  $\mathcal{F}$  and compute  $\mathcal{G}$  by the Legendre transform

$$\mathcal{G}(P, T) = \mathcal{F}(V, T) + PV \quad (3)$$

as in our previous work (Stixrude & Bukowinski 1990). The transformation overcomes the need to use expressions for the equation of state in which  $P$  appears as the independent variable, such as a Taylor series expansion of  $V$  in  $P$ , the Murnaghan equation (Murnaghan 1944), or the Tait equation (Macdonald 1969), as used in some thermodynamic models popular in the Earth sciences (Ghiorso & Sack 1995; Holland & Powell 1998; Gerya *et al.* 2004). These other equations of state are adequate as long as the pressure is a small fraction of the bulk modulus, or if only phase equilibria are of interest as the Gibbs free energy is less sensitive than the density or the moduli to the form of the equation of state. For applications to the whole mantle the Eulerian finite strain theory (Birch 1978), in which  $V$  is the independent variable, is more suitable as it accurately accounts for the variation of the density and elastic constants with pressure (Stixrude & Lithgow-Bertelloni 2005b). The Legendre transformation has been described in terms of the mathematically equivalent operation of handling the Birch–Murnaghan equation of state via integration by parts, that is,  $\int V dP = -\int P dV + PV$  (Fei *et al.* 1990; Ghiorso *et al.* 2002). However, the Legendre transformation is a more powerful and general concept, which permits reformulation of the thermodynamic problem in terms of other potentials as well. For example, Legendre transformation to the internal energy  $\mathcal{U}(S, V) = \mathcal{F}(V, T) + TS$  is important in geodynamic applications (Connolly 2009).

(iii) *Euler form*: In our model the fundamental thermodynamic relation is written in Euler form, which is always possible because of the first order homogeneity of thermodynamic functions (Callen 1960). In the Euler form the thermodynamic potential appears as an absolute quantity. Following our earlier work, we write  $\mathcal{F}(V, T)$  directly in terms of a Taylor series expansion in the finite strain and an integral over the vibrational density of states (Stixrude & Bukowinski 1990). Thus integration from the differential form never appears, and all thermodynamic quantities are computed as derivatives of the original quantity  $\mathcal{F}(V, T)$ . Our approach contrasts with the more common use of the differential form

$$d\mathcal{G} = -SdT + VdP \quad (4)$$

which can be integrated

$$\Delta\mathcal{G}(P, T) = -\int_{T_0}^T S(P_0, T')dT' + \int_{P_0}^P V(P', T)dP' \quad (5)$$

to determine the value of  $\mathcal{G}$  at the pressure and temperature of interest. The integration is typically performed along a path that proceeds in two legs: first upwards in temperature at ambient pressure and second upwards in pressure at the temperature of interest (Helgeson *et al.* 1978; Wood & Holloway 1984; Berman 1988; Fei *et al.* 1990; Saxena 1996; Gottschalk 1997; Bina 1998; Chatterjee *et al.* 1998; Holland & Powell 1998; Fabrichnaya 1999; Matas 1999; Ricard *et al.* 2005; Piazzoni *et al.* 2007; Ganguly *et al.* 2009). The advantage of the differential approach is that it maintains close contact with experimental measurements of the volume and the heat capacity as a function of  $T$  at 1 bar. The differential approach is adequate as long as the temperature and pressure are not too high, but has at least three difficulties in application to Earth's mantle: (1) The temperature at the base of Earth's mantle may be 4000 K, far exceeding the melting points of silicates at ambient pressure. This means that the initial leg of the integration path must extend into the supersolidus regime where no thermodynamic data on the crystalline phase of interest exist and where the crystalline phase of interest may be mechanically unstable. Indeed, elastic instability has been considered as a criterion of melting (Born 1939; Cohen & Gong 1994), rendering the integral over  $SdT$  not only poorly constrained, but also ill-defined. As another way of avoiding the uncontrolled low-pressure  $SdT$  integral, Brosh *et al.* (2008) advocate an alternate integration path passing through infinite pressure, which however is also not well constrained experimentally. (2) While the  $SdT$  term dominates at low pressure, the term  $VdP$  dominates over most of Earth's mantle and must be treated with greater care than is possible using the differential form (Fig. 1). For example, the change in Gibbs free energy along a mantle isotherm exceeds the difference in Gibbs free energy between 300 and 2000 K at pressures as shallow as the transition zone. In the lower mantle, the increase in  $\mathcal{G}$  along an isotherm surpasses in magnitude even the Gibbs free energy of formation from the elements. This means

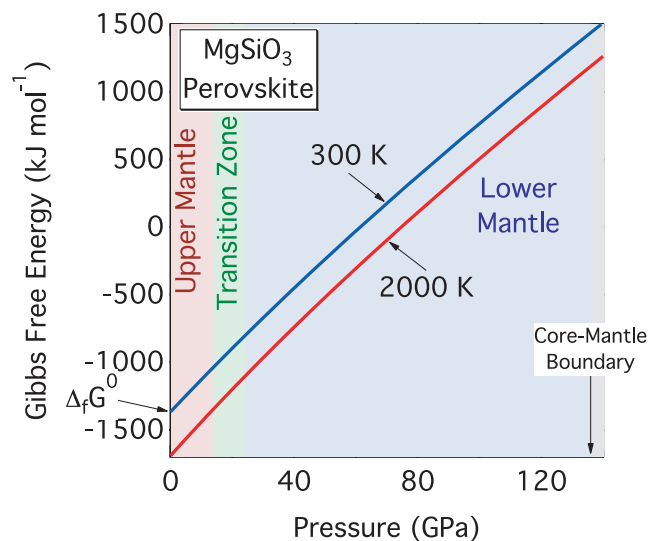


**Figure 1.** Bold lines: Gibbs free energy of  $\text{MgSiO}_3$  perovskite computed with our method along two different isotherms (300 and 2000 K). Indicated are the major regions of Earth's mantle, and its base at the core–mantle boundary, and the Gibbs free energy of formation from the elements of  $\text{MgSiO}_3$  perovskite  $\Delta_f G^0$ .

that in the differential approach, uncontrolled estimates of  $V$  as well as  $S$  at high temperature and low pressure can have a significant and ill-constrained influence on high pressure equilibria. (3) Some mantle phases (e.g. post-perovskite) are unquenchable to ambient pressure, so that the first integral and the low pressure portion of the second integral in eq. (3) are likely to remain unconstrained by experimental measurements at ambient pressure. In contrast, with the Euler form, integration through uncontrolled regions of  $P$ – $T$  space are avoided as the integrals do not appear and computation of the fundamental relation at high pressure and temperature is straightforward and well-posed. Although not as common as the differential form in the Earth Sciences literature, the Euler form is also used in studies of mantle phase equilibria by Jacobs & de Jong (2007), and for example, as the basis of the Steam Tables (Haar *et al.* 1984). The Euler form also has a venerable history in investigations of the high pressure physics of solids and serves as the basis for the derivation of the Birch–Murnaghan equation of state (Grüneisen 1912; Birch 1947; Anderson 1995). The Euler form also proved essential for the development of the anisotropic generalization in Paper I.

(iv) *Anisotropic generalization*: In Paper I, we generalized the thermodynamic machinery to the consideration of deviatoric stress and strain in such a way that fully self-consistent computation of phase equilibria and the elastic constant tensor is possible. This final step is essential for making contact with seismological observations and we are not aware of another thermodynamic model that has this capability. Previous mantle models have either not specified elastic moduli other than the bulk modulus (Stixrude & Bukowski 1993; Mattern *et al.* 2005; Piazzoni *et al.* 2007; Ganguly *et al.* 2009), or have done so non-self-consistently (Sobolev & Babeyko 1994; Kuskov 1995; Bina 1998; Hama & Suito 2001; Ricard *et al.* 2005). Our derivation is given in Paper I and builds on previous work in relating thermodynamic potentials to elasticity (Wallace 1972; Davies 1974). The analysis is based on the Euler form as a polynomial expansion of the thermodynamic potential in the Eulerian finite strain with special attention paid to the distinction between the large finite strain associated with Earth's internal pressure and the much smaller strain of general symmetry applied by a passing seismic wave.

### 3 THEORY

#### 3.1 Outline

The Gibbs free energy of a multiphase assemblage

$$\mathcal{G}(P, T, \vec{n}) = \sum_i^{\text{species}} n_i \mu_i(P, T, \vec{n}) = \sum_i^{\text{species}} n_i [\mathcal{G}_i(P, T) + RT \ln a_i(\vec{n})], \quad (6)$$

where  $n_i$ ,  $\mu_i$ ,  $\mathcal{G}_i$  and  $a_i$  are, respectively, the amount, chemical potential, Gibbs free energy in cation-ordered pure form, and activity of species  $i$  and  $\vec{n}$  is the vector containing all of the  $n_i$ . We assume that the quantity  $RT \ln f_\beta$  is independent of pressure and temperature, where  $f_\beta$  is the activity coefficient. This assumption permits non-ideal enthalpy of solution but neglects the contribution of non-ideality to other physical properties, such as the volume or entropy, because such contributions are small compared with uncertainties in these properties at mantle pressure and temperature (Ita & Stixrude 1992). We neglect surface energy, which may be significant for very small grains ( $\lesssim 1$  nm). We also neglect the possible

influence of electrical, magnetic, or gravitational external fields, which have been explored previously (Ringwood 1959; Bina & Kumazawa 1993; Kavner & Walker 2006). Our focus in this paper is on conditions of isotropic stress, although our approach may also be used to study phase equilibria under conditions of arbitrary stress.

We assume the following form for the chemical potential

$$\mu_i = \mathcal{G}_i - RT \sum_k^{\text{sites}} \left( S_{ik} \ln N_k - \sum_j^c s_{ijk} \ln N_{jk} \right) - \sum_{\beta > \alpha}^{\text{species}} W_{i\alpha\beta} (\delta_{i\alpha} - \phi_\alpha) (\delta_{i\beta} - \phi_\beta), \quad (7)$$

where

$$N_{jk} = \sum_i^{\text{species}} s_{ijk} n_i \quad (8)$$

$$N_k = \sum_j^c N_{jk} \quad (9)$$

$$S_{ik} = \sum_j^c s_{ijk} \quad (10)$$

are, respectively, the number of atoms of component  $j$  on site  $k$ , the total number of atoms on site  $k$ , and the sum over the stoichiometric coefficients of species  $i$  at site  $k$ ,  $s_{ijk}$  is the stoichiometric coefficient of component  $j$  on site  $k$  in species  $i$ , and  $c$  is the number of components. Sums over sites and species extend over all sites and species of the phase to which the species  $i$  belongs. In the sum over  $\alpha$ ,  $\beta$  only terms  $\beta > \alpha$  are included, that is, each pair interaction is counted once and like terms  $\propto W_{i\alpha\alpha}$  are excluded as these are assumed to be contained in  $\mathcal{G}_i$ . The size-weighted proportion of species  $\alpha$  (Holland & Powell 2003)

$$\phi_\alpha = \frac{n_\alpha d_\alpha}{\sum_\gamma n_\gamma d_\gamma}, \quad (11)$$

where  $d_\alpha$  is the size parameter and the sum is over all species in the phase containing species  $\alpha$ , the size-weighted interaction parameter

$$W_{i\alpha\beta} = \frac{2d_i}{d_\alpha + d_\beta} W_{\alpha\beta} \quad (12)$$

and  $\delta_{ij}$  is the Kronecker delta.

To relate our development to other studies of geological phase equilibria, we may evaluate the chemical potential of pure species  $i$  ( $n_i = 1$ ,  $n_{j \neq i} = 0$ )

$$\mu_i = \mathcal{G}_i - RT \sum_k^{\text{sites}} \left( S_{ik} \ln S_{ik} - \sum_j^c s_{ijk} \ln s_{ijk} \right), \quad (13)$$

where the second term accounts for possible cation disorder in the pure species. Thus our definition of  $\mathcal{G}_i$  is equivalent to  $\mu_{i0}$  in the usage of e.g. Cohen (1986) and is consistent with the choice of unit activity for cation-ordered pure species by, for example, Holland & Powell (1998). We prefer the notation  $\mathcal{G}_i$  to  $\mu_{i0}$  because it makes explicit contact with the particular form of the fundamental relation introduced in Paper I and summarized below (Section 3.3.1), and its Legendre transform.

### 3.2 Physical properties of multiphase assemblages

The physical properties of the multiphase assemblage are readily computed via derivatives of the fundamental relation (eq. 6)

$$S = -\left(\frac{\partial \mathcal{G}}{\partial T}\right)_P = \sum_i n_i S_i - n_i R \ln a_i \quad (14)$$

$$V = \left(\frac{\partial \mathcal{G}}{\partial P}\right)_T = \sum_i n_i V_i \quad (15)$$

$$\frac{V}{K_T} = -\left(\frac{\partial V}{\partial P}\right)_T = -\left(\frac{\partial^2 \mathcal{G}}{\partial P^2}\right)_T = \sum_i n_i \frac{V_i}{K_{Ti}} - \left(\frac{\partial n_i}{\partial P}\right)_T V_i \quad (16)$$

$$\begin{aligned} C_P &= T \left(\frac{\partial S}{\partial T}\right)_P = -T \left(\frac{\partial^2 \mathcal{G}}{\partial T^2}\right)_P \\ &= \sum_i n_i C_{Pi} + \left(\frac{\partial n_i}{\partial T}\right)_P (S_i - R \ln a_i) \end{aligned} \quad (17)$$

$$V\alpha = \left(\frac{\partial V}{\partial T}\right)_P = \left(\frac{\partial^2 \mathcal{G}}{\partial P \partial T}\right) = \sum_i n_i V_i \alpha_i + \left(\frac{\partial n_i}{\partial T}\right)_P V_i, \quad (18)$$

where all derivatives are taken at constant bulk composition. Other quantities such as the adiabatic bulk modulus  $K_S$ , isochoric heat capacity,  $C_V$  and Grüneisen parameter,  $\gamma$  are computed from the quantities already given (Ita & Stixrude 1992). The terms involving pressure and temperature derivatives of  $n_i$  are taken at chemical equilibrium, so that  $\mu_i dn_i = 0$ . These terms have been called the ‘metamorphic’ contributions to thermodynamic properties and appear only in multiphase, multicomponent systems and for processes that are sufficiently slow for chemical equilibrium to be maintained (Stixrude & Lithgow-Bertelloni 2007). Generalized expressions written in terms of the full stress and strain tensors and expressions for the elastic moduli are given in Paper I. While it will not be the focus of this paper, we note that our theory may also be applied to phase equilibria under conditions of anisotropic stress, for example, to phase transformations induced by shear, such as may be relevant to understanding the passage of a seismic wave through a region of phase coexistence, or to localized regions of large deviatoric stress such as in the vicinity of faults.

### 3.3 Contributions to the chemical potential

We now consider further the contributions to the chemical potential: the three terms on the right hand side of eq. (7), the first term expressing the Gibbs free energy of the pure cation-ordered species, the second term expressing the ideal contribution, and the third term expressing the excess contribution.

#### 3.3.1 End-member contribution

The first term on the right-hand side of eq. (7)  $\mathcal{G}_i$  is the term due to the pure end-member species, and is specified (less the Landau contribution discussed below) by the Legendre transformation of the Helmholtz free energy

$$\begin{aligned} \mathcal{F}(\rho, T) &= \mathcal{F}_0 + \frac{1}{2\rho_0} b_{iikk}^{(1)} f^2 + \frac{1}{6\rho_0} b_{iikkmm}^{(2)} f^3 \\ &+ \dots + 9nk\Delta \left[ T D \left( \frac{\theta}{T} \right) \right] + \Delta \mathcal{F}_{mag}(\rho, T), \end{aligned} \quad (19)$$

where subscript 0 indicates values in the natural configuration, here taken to be that at ambient conditions

$$f = \frac{1}{2} \left[ \left( \frac{\rho}{\rho_0} \right)^{2/3} - 1 \right] \quad (20)$$

is the scalar part of the Eulerian finite strain, the density  $\rho = 1/V$ , the coefficients of the cold part are

$$b_{iikk}^{(1)} = 9K_{T0} \quad (21)$$

$$b_{iikkmm}^{(2)} = 27K_{T0} (K'_{T0} - 4) \quad (22)$$

primes indicate pressure derivatives,  $k$  is the Boltzmann constant,  $\theta$  is the characteristic vibrational temperature, and  $D(x)$  is the Debye free energy function, which is related to an integral over the vibrational density of states (Born & Huang 1954)

$$D(x) = x^{-3} \int_0^x \ln(1 - \exp^{-t}) t^2 dt. \quad (23)$$

We assume that  $\theta$  varies with strain as

$$\theta^2 = \theta_0^2 \left( 1 + a_{ii}^{(1)} f + \frac{1}{2} a_{iikk}^{(2)} f^2 + \dots \right) \quad (24)$$

with coefficients

$$a_{ii}^{(1)} = 6\gamma_0 \quad (25)$$

$$a_{iikk}^{(2)} = -12\gamma_0 + 36\gamma_0^2 - 18q_0\gamma_0, \quad (26)$$

where  $\gamma$  is the isotropic component of the Grüneisen tensor, and  $\gamma q$  is the isotropic component of the strain derivative of the Grüneisen tensor. In eqs (19)–(26) the subscripts  $i, j, k, \dots$  refer to the Cartesian indices of the general strain tensor as they appear in the original, fully anisotropic form of the fundamental relation in Paper I. We have retained the Cartesian subscripts in order to emphasize the connection between the equations we present here and the theory valid under more general strain derived in Paper I. The expression for the Helmholtz free energy, aside from the magnetic contribution, which we now discuss, is derived in Paper I and evaluated here under conditions of isotropic initial stress. Expressions for the full elastic constant tensor are found by taking the appropriate strain derivatives of  $\mathcal{F}$  and are given in Paper I.

The magnetic contribution, which we assume to have the form

$$\mathcal{F}_{mag} = -T \sum_i r_i \ln(2S_i + 1) \quad (27)$$

accounts for configurational entropy of spin degeneracy, where  $r_i$  and  $S_i$  are the stoichiometric coefficient and spin quantum number of element  $i$ , respectively, and the sum is over all atoms in the formula unit (Ulbrich & Waldbaum 1976). This high temperature form is expected to be accurate for all mantle phases, which have magnetic disordering temperatures far below room temperature. We assume  $S = 2$  for high spin Fe, and  $S = 0$  for all other cations considered in this paper. In this study, we have ignored variations in  $S$  on compression, which have been found experimentally (Badro *et al.*, 2003; Badro *et al.* 2004). The details of spin-pairing transitions are still uncertain in ferropericlase (Persson *et al.* 2006) and even more so in the case of perovskite and post-perovskite (Bengtson *et al.* 2005). Moreover, as the spin transition is likely to affect partitioning, it seemed premature to include its effects on one phase and not others. As experimental and theoretical evidence of the nature of spin-pairing transitions continues to be gathered, this information will be readily incorporated in our model.

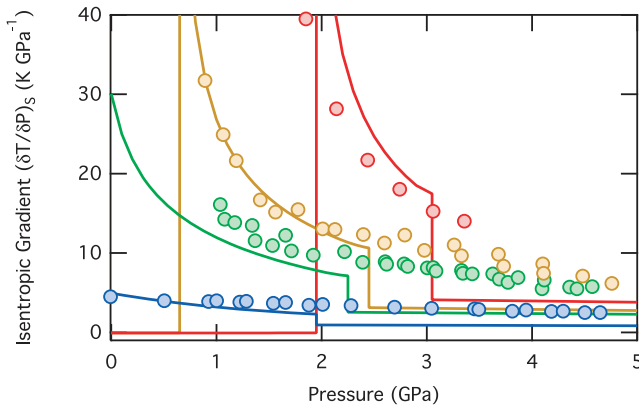


**Figure 2.** Isentropic gradient of  $\text{SiO}_2$  in the vicinity of the  $\alpha$  to  $\beta$  transition in quartz computed with our method (lines) and measured experimentally (Boehler 1982) (circles) at: (blue) 300 K, (green) 800 K, (gold) 1000 K, (red) 1300 K. The sudden increase in the isentropic gradient with increasing pressure marks the  $\alpha$  to  $\beta$  transition, and the sudden, smaller decrease marks the quartz to coesite transition. Agreement with experimental data is comparable to that of the system-specific model of Dorogokupets (1995). The decrease in the isentropic gradient at the  $qtz$ - $coes$  transition does not appear in the experimental data, possibly due to kinetic hindrances in the experiments.

Following Putnis (1992), we assume a contribution to the free energy associated with displacive transitions such as  $\alpha$ - $\beta$  quartz and stishovite to  $\text{CaCl}_2$ -structured silica of the tricritical Landau form, which provides a remarkably good account of isotropic thermodynamic properties along typical geotherms (Fig. 2)

$$\mathcal{G}_L(P, T) = S_D \left[ (T - T_C) Q^2 + \frac{1}{3} T_{C0} Q^6 \right] \quad (28)$$

$$Q^4 = (1 - T/T_C) \quad (29)$$

$$T_C = T_{C0} + \frac{V_D}{S_D} P, \quad (30)$$

where  $S_D$  and  $V_D$  are, respectively, the maximum excess entropy and volume,  $T_C$  is the transition temperature,  $Q$  is the order parameter and  $\mathcal{G}_L = 0$  for  $T > T_C$ . The total Gibbs free energy for phases with a Landau contribution is then

$$\mathcal{G}_{\text{total}}(P, T) = \mathcal{G}(P, T) + \mathcal{G}_L(P, T), \quad (31)$$

where  $\mathcal{G}$  is the Gibbs free energy of the high-temperature phase, computed as for other phases from the Legendre transformation of the Helmholtz free energy (eq. 19), and we have suppressed the species subscript  $i$ . From these relationships, all other thermodynamic contributions may be derived including the contribution to the volume via the identity  $V = (\partial \mathcal{G} / \partial P)_T$

$$V_L(P, T) = -V_D Q^2 \left[ 1 + \frac{1}{2} \frac{T}{T_C} (1 - T_{C0}/T_C) \right] \quad (32)$$

as well as to the entropy, thermal expansivity, bulk modulus and heat capacity, which can be found via pressure and temperature derivatives of  $\mathcal{G}_{\text{total}}$ , and application of eqs (14)–(18). As in, for example, Holland & Powell (1998) we have truncated the Landau expansion at the lowest order that yields a transition and have therefore neglected other contributions including higher order terms in the order parameter, order parameter–strain coupling, and fluctuation-induced softening (Carpenter *et al.* 1998, 2000). These higher order terms are particularly important in reproducing the variation of the

elastic constant tensor through the transition. As elasticity is not the focus of this paper, such extensions fall outside our present scope, although they are readily included in our formulation. Although Landau terms contribute to few phases in this paper ( $qtz$ ,  $st$ ), we anticipate Landau contributions becoming more important as we expand our model to include behaviour associated with magnetic collapse in future work.

### 3.3.2 Ideal contribution

The second term on the right-hand side of eq. (7) is the ideal contribution to the chemical potential. We have derived this term by assuming that crystallographic sites and atoms of different elements are distinguishable, while atoms of the same element are indistinguishable (Kerrick & Darken 1975). We further assume that the quantum energy levels of a solid solution of a fixed composition are the same for all configurations. The number of distinguishable configurations in one phase is then

$$\Omega = \prod_k \frac{(\sum_j^c N_{jk})!}{\prod_j^c N_{jk}!}. \quad (33)$$

Applying Stirling's approximation to  $S_{\text{conf}} = k \ln \Omega$ , we find the configurational entropy

$$S_{\text{conf}} = R \sum_k \left( N_k \ln N_k - \sum_j^c N_{jk} \ln N_{jk} \right), \quad (34)$$

The ideal contribution to the chemical potential then follows from the definition

$$\mu_i = \left( \frac{\partial \mathcal{G}}{\partial n_i} \right)_{n'_i} \quad (35)$$

where the subscript on the derivative means that the amounts of all other species are held constant, and we have made use of the results  $\partial N_{jk} / \partial n_i = s_{ijk}$  and  $\partial N_k / \partial n_i = S_{ik}$ .

The expression for the ideal contribution to the chemical potential is closely related to that of the 'sublattice' model (Hillert & Staffansson 1970; Sundman & Agren 1981) and the 'random entropy' model (Thompson 1969; Cohen 1986), also known as the 'mixing-on-sites' model. We have derived the general expression explicitly in terms of the molar amounts of the end-member species, rather than writing expressions that are limited in the number of components, or written in terms of component site-fractions only, as in these previous publications, because the solution properties of some mantle phases are fairly complex with many components on several different sites. The general expression is also valid in the case of phases that contain end-members with cation disorder.

### 3.3.3 Excess contribution

The third term on the right-hand side of eq. (7) is the non-ideal or excess contribution. This term follows the asymmetric van Laar formulation (Powell 1974; Saxena & Fei 1988; Aranovich & Newton 1999; Holland & Powell 2003), and originates in pairwise interactions among species in solid solution for which the excess Gibbs free energy

$$\mathcal{G}_{xs} = \sum_{\beta > \alpha} \phi_\alpha \phi_\beta B_{\alpha\beta}, \quad (36)$$

where

$$B_{\alpha\beta} = 2 \frac{\sum_{\gamma} d_{\gamma} x_{\gamma}}{d_{\alpha} + d_{\beta}} W_{\alpha\beta} \quad (37)$$

and  $x_{\alpha} = n_{\alpha} / \sum_{\gamma} n_{\gamma}$ . The form of eq. (36) illustrates the relationship to the symmetric regular solution model to which the excess contribution reduces in case all the size parameters  $d_{\alpha}$  are equal.

#### 4 APPLICATION OF THE SOLUTION MODEL TO MANTLE PHASES

We complete the specification of the solution model, consisting of the ideal and excess contributions to the chemical potential: the second and third terms on the right hand side of eq. (7), and test the assumed form of this aspect of our model against crystallographic, thermochemical, and phase equilibrium data on mantle phases.

##### 4.1 Ideal contribution

The ideal contribution to the chemical potential is completely specified by the choice of end-member species, the number of mixing sites, and the cations that occupy them. Our general strategy in choosing end-member species has been to: (1) adopt species compositions that have been studied experimentally in pure form, whenever possible (2) to choose the minimal set of end-members that spans the range of phase compositions that are likely to exist in the mantle and (3) to choose end-members that permit an accurate account of crystallographic, thermochemical and phase equilibria data where these are available. These choices are illustrated with the following examples and specified in Table A1.

The form of the ideal contribution that we have chosen is specified by the chemical formulae of the end-member species. The formulae as written in Table A1 therefore convey not only chemical, but also structural information related to the number of mixing sites, the cations that occupy them, and the nature of the mixing. In order to convey this information, we have found it convenient to adopt the following conventions for writing the chemical formulae. (1) Sites are specified by the stoichiometric coefficients: one coefficient for each site (we follow the usual chemical convention of suppressing unit coefficients). (2) The number of sites of each end-member of a given phase are the same. (3) The sites appear in the same order in all end-members. (4) Two or more distinct cations that occupy the same crystallographic site in random arrangement are joined by parentheses. (5) Two or more distinct cations that occupy the same site and do not mix are surrounded by square brackets. We note that no standard exists for the writing of crystal-chemical formulae. Although ours bears some relationship to other schemes that have been proposed for structural formulae (Limadefaria *et al.* 1990), it is also distinct because its motivation is different: to specify an ideal solution model, rather than to convey crystallographic information. Computation of the configurational entropy for various alternative models of the *en-mgts* solution illustrates our notation (Fig. 3).

For many phases, crystallography makes clear the form of the ideal contribution. For example, in the case of Mg–Fe olivine X-ray and neutron diffraction show that Mg and Fe are nearly randomly distributed over the two crystallographically distinct octahedral sites (M1, M2) for mantle-like compositions (Heinemann *et al.* 2007). Following many previous studies (Wiser & Wood 1991; Frost 2003b), we therefore approximate olivine as having a single mixing site for divalent cations. We have chosen to neglect

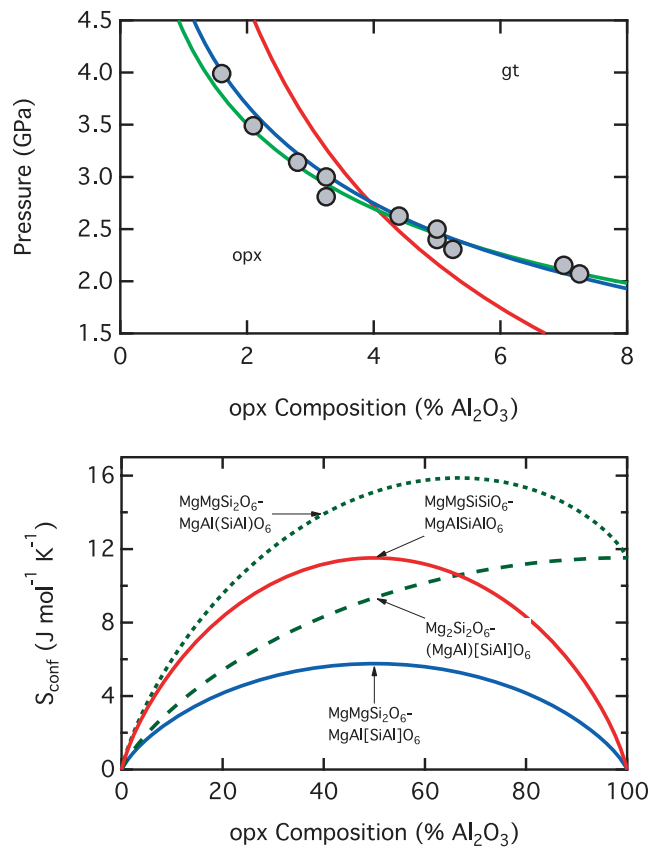


**Figure 3.** Top: composition of *opx* coexisting with *py* on the  $\text{Mg}_4\text{Si}_4\text{O}_{12}$ – $\text{Mg}_3\text{Al}_2\text{Si}_3\text{O}_{12}$  join at 1373 K computed from our model (blue,  $m = 1$  cf. eq. 38); and from alternative models with (green) a different estimate of  $V_0(\text{mgts}) = 60.4 \text{ cm}^3 \text{ mol}^{-1}$  (Brey *et al.* 1999); and (red) cation mixing permitted independently on two sites ( $m = 2$ ); compared with experimental data (black circles) (Perkins *et al.* 1981). Bottom: configurational entropy of four different models of cation disorder in *en-mgts opx*, specified by the indicated formulae according to the conventions described in the text: (blue) our model with mixing on only one octahedral site ( $m = 1$ ), which is equivalent to correlated cation disorder on one octahedral and one tetrahedral site; (red)  $m = 2$  with independent cation mixing on one octahedral and one tetrahedral sites; (black long-dashed) mixing across octahedral sites, with octahedral Mg–Al disorder in the *mgts* end-member; (black short-dashed) mixing across tetrahedral sites and on one octahedral site, with tetrahedral Al–Si disorder in the *mgts* end-member. For both figures the composition is given as the mole fraction:  $\text{Al}_2\text{O}_3/(\text{Al}_2\text{O}_3 + \text{MgSiO}_3)$ .

the slight observed Mg–Fe intersite partitioning because the contribution to the configurational entropy is small and less than the uncertainty in the total entropy. We have assumed complete intersite Mg–Fe disorder on Mg–Fe binary joins in all phases considered in this study, consistent with experimental findings of weak inter-site Mg–Fe partitioning in other phases (Kroll *et al.* 1997). In the case of phases containing more than two mixing cations, Mg–Fe partitioning among sites may arise in our formulation due to mass balance, for example in *opx*, where our choice of aluminous end-member (*mgts*) leads to relative Mg enrichment in the Al-free octahedral site. Thus intersite Mg–Fe partitioning in our approach is that consistent with the constraints of mass balance and minimization of the Gibbs free energy: we do not arbitrarily assume equipartition of Mg–Fe among sites in multicomponent systems and thus avoid the logical inconsistency that this entails (Holland & Powell 2006). The ideal term for clinopyroxenes of the diopside-clinoenstatite series is

also crystallographically constrained: Ca–Mg partitioning between the two divalent cation sites is very strong and almost all Ca occupies the larger of the two sites. We therefore assume that Ca–Mg mixing occurs only on the large site. Holland *et al.* (1979) explored a model that permitted small amounts of Ca–Mg exchange between the large site and the octahedral site, but the influence on phase equilibria is smaller than that of uncertainties in the excess Gibbs free energy.

For some other phases, equilibria provide the best constraints on the form of the ideal contribution. Orthopyroxenes on the  $\text{MgMgSiSiO}_6$ – $\text{MgAlAlSiO}_6$  join have in principle four crystallographically distinct cation sites. Information from X-ray crystallography is limited because  $\text{Mg}^{2+}$ ,  $\text{Al}^{3+}$  and  $\text{Si}^{4+}$  are isoelectronic, and there are no thermochemical measurements of the ideal entropy of solution because equilibrium states of order are difficult to achieve. Phase equilibria point to a model in which Mg–Al disorder is correlated with Si–Al disorder via local charge balance (Al-avoidance). The configurational entropy in the case of perfect correlation is equivalent to assuming complete disorder on the octahedral site and none on the tetrahedral site. The influence on phase equilibria of correlated cation disorder (Fig. 3) is illustrated by the reaction  $\text{en} + \text{mgt} = \text{py}$  for which the equilibrium value of  $x = n_{\text{mgt}}/(n_{\text{mgt}} + n_{\text{en}})$  is given by

$$\ln x(1-x) = \frac{\Delta G}{mRT}, \quad (38)$$

where  $\Delta G = G_{\text{py}} - G_{\text{en}} - G_{\text{mgt}}$  and  $m$  is the number of independent mixing sites:  $m = 1$  for correlated cation disorder and  $m = 2$  for uncorrelated disorder. The pressure dependence of  $x$  in the limit of small  $x$

$$\left( \frac{\partial \ln x}{\partial P} \right)_T = \frac{\Delta V}{mRT} \quad (39)$$

so that with two mixing sites instead of one, the pyroxene composition varies more slowly with increasing pressure in a way that does not match experimental data. The influence of doubling the number of mixing sites far exceeds the effects of uncertainty in the volume of the fictive *mgt*s end-member. These results are consistent with previous analyses of phase equilibria and with inferences based on X-ray diffraction measurements of bond lengths (Ganguly & Ghose 1979; Wood & Holloway 1984). Other solution models are of course possible and Ganguly & Ghose (1979) have argued for an alternate choice of aluminous orthopyroxene end-member with pyrope composition; but agreement with phase equilibria data using this alternative is no better (Wood & Holloway 1984).

For other phases, thermochemical information from experiment or theory constrains the form of the ideal contribution. In the case of clinopyroxene, thermochemical and X-ray diffraction data indicate Si–Al disorder in end-member Ca–Tschermak's pyroxene (Okamura *et al.* 1974; Haselton *et al.* 1984), which we have included. In the case of end-member  $\text{Mg}_3(\text{MgSi})\text{Si}_3\text{O}_{12}$  majorite, we assume complete Mg–Si order on the octahedral site, which closely approximates the results of recent semi-empirical theory at mantle temperatures (Vinograd *et al.* 2006). In the case of  $\text{MgSiO}_3$ – $\text{AlAlO}_3$  perovskite, experimental data is very limited or contradictory and we have relied heavily on first principles theory, which indicates that complete, uncorrelated disorder on the large site and the octahedral site, while overestimating slightly the entropy computed from first principles, is a reasonable approximation at typical lower mantle temperatures (Panero *et al.* 2006; Jung *et al.* 2010).

In the case of garnet, we have chosen a set of end-member species that spans the range of compositions likely to exist in the mantle, within the context of the NCFMAS system (Fig. 4). To our knowledge, our range spans all NCFMAS garnets synthesized so far, including compositions that are unlikely to occur in the mantle such

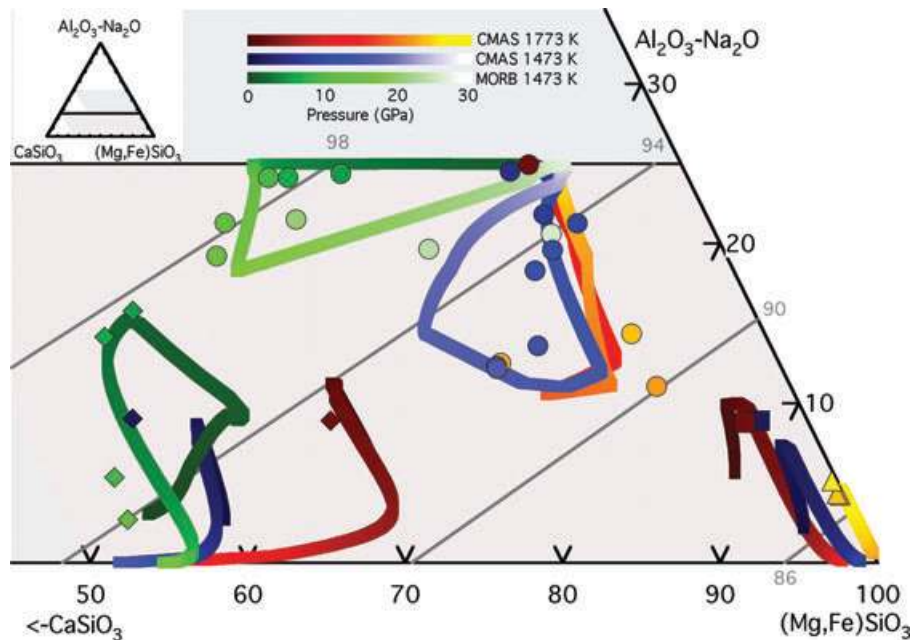


**Figure 4.** Experimental measurements of the compositions of coexisting *cpx* (lower left, diamonds) *opx* (lower right, squares), *gt* (upper middle, circles), and *py* (extreme lower right, triangles) in CMAS at 1773 K (low pressure reds Klemme & O'Neill 2000); pyrolyte at 1773 K (high pressure reds Irifune 1994), CMAS at 1473 K (*opx* and *cpx* blues Sen 1985), pyrolyte minus olivine at 1473 K (*gt* blues Irifune 1987) and a MORB composition (olivine tholeiite A) at 1473 K (greens Irifune *et al.* 1986), compared with the results of our model (lines) for CMAS at 1773 K (reds), CMAS at 1473 K (blues), and olivine tholeiite A at 1473 K (greens). Colour shading of lines and symbols correspond to pressure according to the indicated scales. Background shading shows the range of compositions spanned by our model for *gt* (red and grey) and *cpx/opx* (red and blue). Grey contour lines show the variation with composition of the shear modulus of garnet at ambient conditions.

as Al-free Mg–Ca majorite (Hazen *et al.* 1994) and Al-free Mg–Fe majorite (Ohtani *et al.* 1991). Pure  $\text{CaSiO}_3$  and pure  $\text{FeSiO}_3$  garnets, for example, fall outside our range, but these compositions are known to be unstable. Our choice is not unique and, while not violating X-ray crystallographic data, does not fully capture crystal chemical expectations. For example, our choice precludes cations other than Mg, Si or Al on the octahedral site, whereas it seems likely that Fe would also enter the octahedral site. To include additional end-members to allow for more flexibility in octahedral site occupation, or to span a still wider range of garnet compositions, as done by Ita & Stixrude (1992), seemed unjustified at this point given the inevitable uncertainties in the properties of the additional end-members.

#### 4.2 Excess contribution

We have chosen the asymmetric van Laar formulation because it is parametrically compact while solving a long-standing problem in the representation of the excess properties of solutions with more than two components (Holland & Powell 2003). Many alternative formulations of multicomponent, and/or multisite solutions involve three-site or site-exchange terms that cannot be constrained even in principle from observations on binary joins (Powell & Holland 1993; Ganguly 2001). The difficulty in constraining these terms is serious because many mantle solid solutions involve more than two species and more than one mixing site, and because experimental data on binaries are far more common than data on ternary or quaternary solutions. Not only does the asymmetric van Laar formulation offer a parametrically compact description in which parameters can be related directly to data on binaries, it also affords a convenient starting point for approximations in those cases where data on the relevant binary do not exist.

The asymmetric van Laar formulation differs from others that are used more widely, yet matches experimental data at least as well if not better. The differences are illustrated by the di-cats join (Fig. 5). The asymmetric van Laar formulation matches the thermochemical data marginally better ( $\chi^2 = 0.40$ ) than either the two-parameter Margules ( $\chi^2 = 0.54$ ) or Redlich & Kister (1948) ( $\chi^2 = 0.42$ ) fits that have appeared in the literature (Benisek *et al.* 2007; Cohen 1986). The value of  $\chi^2$  is sufficiently small in this case that no choice can be made as to which of the three forms is superior: they all fit the data well within the uncertainty of the measurement. We prefer the asymmetric van Laar formulation given the advantages outlined above, and since it at least does no worse in fitting experimental data along binaries.

We have assumed that the excess interaction parameters are independent of pressure and temperature. It is common practice to assign pressure and temperature variations to the interaction parameters, that is,  $W = W_U + PW_V - TW_S$  where  $W_V$  and  $W_S$  are the excess volume and entropy, respectively. However, the pressure and temperature dependence of  $W$  is usually either small or poorly constrained experimentally (Geiger 1999). For example, the excess entropy term has not been measured thermochemically and must be inferred from phase equilibria data. Inferences are sufficiently non-unique that different determinations disagree on the magnitude and the sign of  $W_S$ . Thermochemically, it is more straightforward to assess the vibrational contribution to the excess entropy: this contribution appears to be indistinguishable from zero where it has been measured (Bosenick *et al.* 1996; Etzel *et al.* 2007). The quantity  $W_V$  can be determined with much greater precision via X-ray diffraction. However,  $W_V$  is rarely determined except at

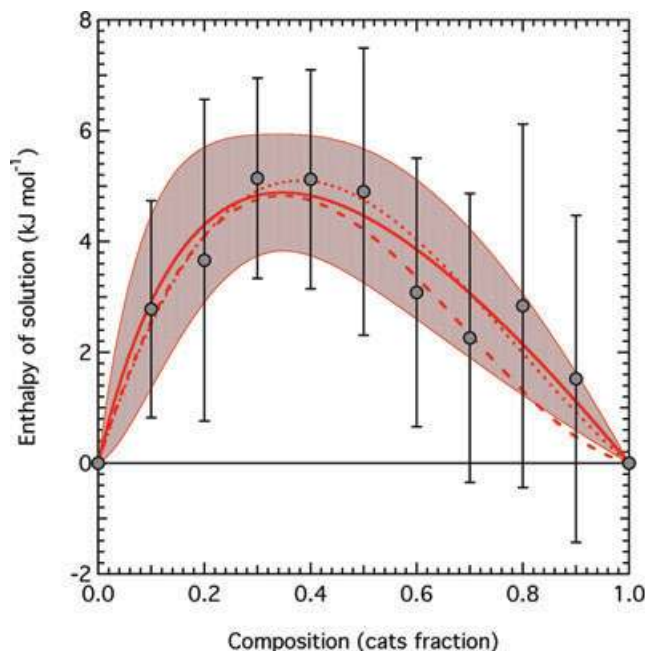


**Figure 5.** Enthalpy of solution on the *di-cats* join as experimentally measured (symbols) (Benisek *et al.* 2007), compared with our best fit using the asymmetric van Laar formulation (bold red line and shaded  $1\sigma$  confidence band), the Margules formulation fit of Benisek *et al.* (2007) (long dashed line) and the Redlich–Kister formulation fit of Cohen (1986) to the earlier experimental data of Newton *et al.* (1977) (short dashed line).

ambient conditions. As we are interested in large ranges of pressure and temperature and since  $W_V$  may very well change sign over the relevant range, we thought it most prudent to set  $W_V = 0$  for all phases. We note that pressure and temperature dependence of the  $W_{\alpha\beta}$  is a feature readily added to our formulation as more knowledge is gained from experiment and theory (Tsuchiya & Tsuchiya 2008).

#### 5 PARAMETER ESTIMATION

We explore further the properties of the thermodynamic model outline above. The model contains nine species-specific parameters:  $\mathcal{F}_0$ ,  $V_0$ ,  $K_{T0}$ ,  $K'_{T0}$ ,  $\theta_0$ ,  $\gamma_0$ ,  $q_0$ ,  $G_0$ ,  $G'_0$ ,  $\eta_{S0}$ , the regular solution parameters  $W_{\alpha\beta}$  and  $d_\alpha$  and the Landau parameters,  $T_{C0}$ ,  $V_D$ , and  $S_D$ . The shear modulus,  $G$ , its pressure derivative,  $G'_0$ , and  $\eta_S$ , the shear part of the strain derivative of the Grüneisen tensor, appear in derivatives of the fundamental relation with respect to anisotropic strain (Paper I). Most or all of these parameters are now constrained by experimental measurements for at least some of the compositional range of all major mantle phases.

We perform an iterative global least-squares inversion of experimental data for the values of all of these parameters (Table A1–A3). We supplement experimental measurements with the results of first principles calculations for properties that have not yet been measured experimentally. When neither experimental or first principles results exist, we rely on systematic relationships, as discussed in Paper I. Values have been updated in many cases from our previous studies (Stixrude & Lithgow-Bertelloni 2005a, 2007; Xu *et al.* 2008) as more experimental data has become available, as we have included more species, phases, and components into our scheme, and as we have improved the solution model. The global inversion strategy is detailed in Appendix A.

To provide a means of gauging the robustness of the model parameters determined from the global inversion, we analyse: (i) the sensitivity of various experimentally measured quantities to the values of the parameters and (ii) the physics underlying the parameters and estimates of their most likely values. We focus our analysis here on the parameters that are most closely related to phase equilibria:  $\mathcal{F}_0$ ,  $\theta_0$  and  $W_{\alpha\beta}$ ; the other parameters have been discussed in detail in Paper I. Our discussion also serves to illustrate the relationship between experiment and parameters such as  $\theta_0$  that are difficult to measure directly, although as we show, each may be related to commonly measured quantities. The value of these illustrations is heuristic and supplements the full global inversion.

### 5.1 Parameter sensitivity

We anticipate that positions of univariant phase transitions are primarily sensitive to the values of  $\mathcal{F}_0$  and  $\theta_0$ . The dependence on  $\mathcal{F}_0$  of the high-pressure phase to leading order is

$$dP_{tr} = \frac{d\mathcal{F}_{0j}}{\Delta V}, \quad (40)$$

where the subscript  $tr$  refers to the transition, and  $\Delta V = V_i - V_j$  where, without loss of generality,  $i, j$  refer to the low and high pressure phases, respectively. For example, taking nominal values of the uncertainty in the location of a high pressure phase transformation  $dP_{tr} = 1$  GPa and  $\Delta V = 0.3 \text{ cm}^3 \text{ mol}^{-1} \text{ atom}^{-1}$ , we should expect uncertainties in inverted values of  $\mathcal{F}_0$  to be  $d\mathcal{F}_0 = 0.3 \text{ kJ mol}^{-1} \text{ atom}^{-1}$ . Numerical calculations bear out these expectations (Fig. 6).

The value of  $\theta_0$  influences phase equilibria through the Clapeyron slope (Fig. 6). To lowest order in  $\theta_0/T$ , the dependence of the Clapeyron slope  $\Gamma$  on the Debye temperature of the high pressure phase  $j$  is (Jeanloz 1987)

$$d\Gamma = \frac{3nRd \ln \theta_{0j}}{\Delta V}, \quad (41)$$

In detail, variations in the value of  $\theta_0$  will also influence the value of  $\Delta V$  through the influence of  $\theta_0$  on the thermal expansion, but this effect is small (Stixrude & Lithgow-Bertelloni 2005b). For example, taking nominal values of  $d\Gamma = 1 \text{ MPa K}^{-1}$  and  $\Delta V = 0.3 \text{ cm}^3 \text{ mol}^{-1} \text{ atom}^{-1}$ , we should expect uncertainties in values of  $\theta_0$  constrained only by phase equilibrium data to be  $d \ln \theta_0 = 1$  per cent, which is born out by numerical calculations (Fig. 6).

Uncertainties in  $\theta_0$  and  $\mathcal{F}_0$  are correlated: there exists a trade-off between the best-fitting values of the two parameters. To lowest order in  $\theta/T$  and  $P/K_T$ , the value of  $\mathcal{G}(P, T)$  is invariant if  $\mathcal{F}_0$  and  $\theta_0$  vary according to

$$d\mathcal{F}_0 = 3nRT d \ln \theta_0. \quad (42)$$

The trade-off is particularly evident for phase transformations for which the Clapeyron slope is poorly constrained by experiment, including several high pressure phase transformations, the measurements being concentrated over too narrow a range of temperature to define a slope. An example is the transformation to the *seif* form of silica (Murakami *et al.* 2003). In such cases we have supplemented experimental data with the results of first principles calculations at low temperature (Karki *et al.* 1997a) in order to better constrain the slope of the transition.

### 5.2 Analysis of parameter values

We anticipate the value of  $\theta_0$  via analysis of the vibrational spectra of minerals (Kieffer 1980). The vibrational spectrum may be used to estimate thermochemical quantities via the moments of the vibrational density of states. The moment most relevant here is the zeroth moment

$$\theta(0) = \frac{\hbar}{k} \exp \left[ \frac{1}{3} + \frac{\int_0^\infty \ln \omega g(\omega) d\omega}{\int_0^\infty g(\omega) d\omega} \right] \quad (43)$$

since our values of  $\theta_0$  are most sensitive to the entropy and the free energy, both of which depend to leading order on  $\theta(0)$ . The quasi-harmonic Helmholtz free energy per atom can be written exactly as the infinite series (Barron *et al.* 1957)

$$\mathcal{F}_q = 3RT \left\{ -\frac{1}{3} + \ln \frac{\theta(0)}{T} - \frac{1}{40} \left[ \frac{\theta(2)}{T} \right]^2 + \dots \right\}, \quad (44)$$

where  $\theta(p)$  is the  $p$ th moment of the vibrational density of states. For typical values of  $\theta(p) = 750 \text{ K}$  and  $T = 1000 \text{ K}$ , the term involving  $\theta(2)$  and higher order terms contribute only 4 per cent of the total so that the value of  $\mathcal{F}_q$  is almost entirely determined by the leading order term involving  $\theta(0)$ . In Paper I, we presented a similar analysis in which we showed that the leading order term involving  $\theta(0)$  accounts for more than 99 per cent of the entropy (Stixrude & Lithgow-Bertelloni 2005b).

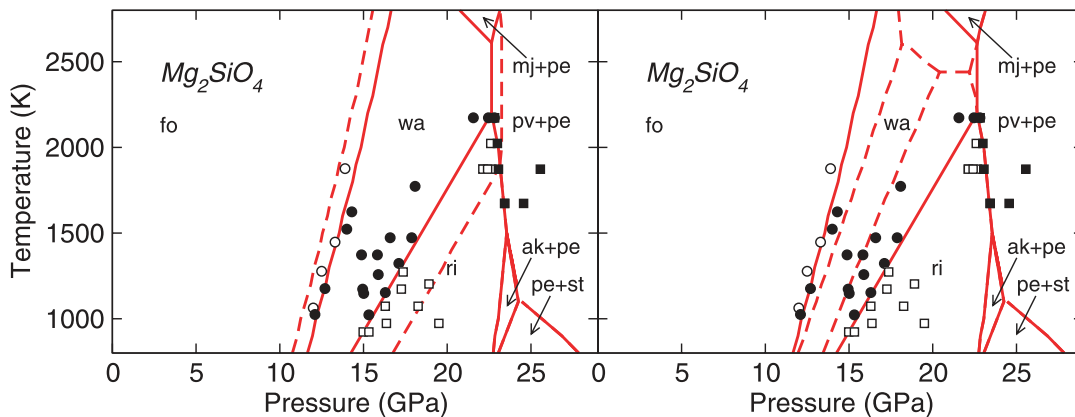


**Figure 6.** Solid lines:  $\text{Mg}_2\text{SiO}_4$  phase diagram computed with our model and (dashed lines) with perturbed values of the parameters of *mgwa*. Left:  $\mathcal{F}_0$  reduced by  $2 \text{ kJ mol}^{-1}$ , and right:  $\theta_0$  increased by  $7 \text{ K}$ . Symbols are experimental observations of stability of *fo* (open circles), *wa* (closed circles), *ri* (open squares) and *pv+pe* (closed squares) (Morishima *et al.* 1994; Suzuki *et al.* 2000; Fei *et al.* 2004).

Our inverted values of  $\theta_0$  agree with values of  $\theta(0)$  computed from eq. (43) and model vibrational densities of states (Kieffer 1980) to within the uncertainty of the analysis of Kieffer (1980) for all phases except *qtz*, *an*, *ab* and *al* (Fig. 7). In the case of these four species, our theory yields vibrational entropies in agreement with experiment while that of Kieffer (1980) yields vibrational entropies that are systematically lower than experiment. Our estimates of  $\theta_0$  are more accurate than those derived from model vibrational densities of states because experimental information on the form of  $g(\omega)$  is incomplete. While the Brillouin zone centre is easily acces-

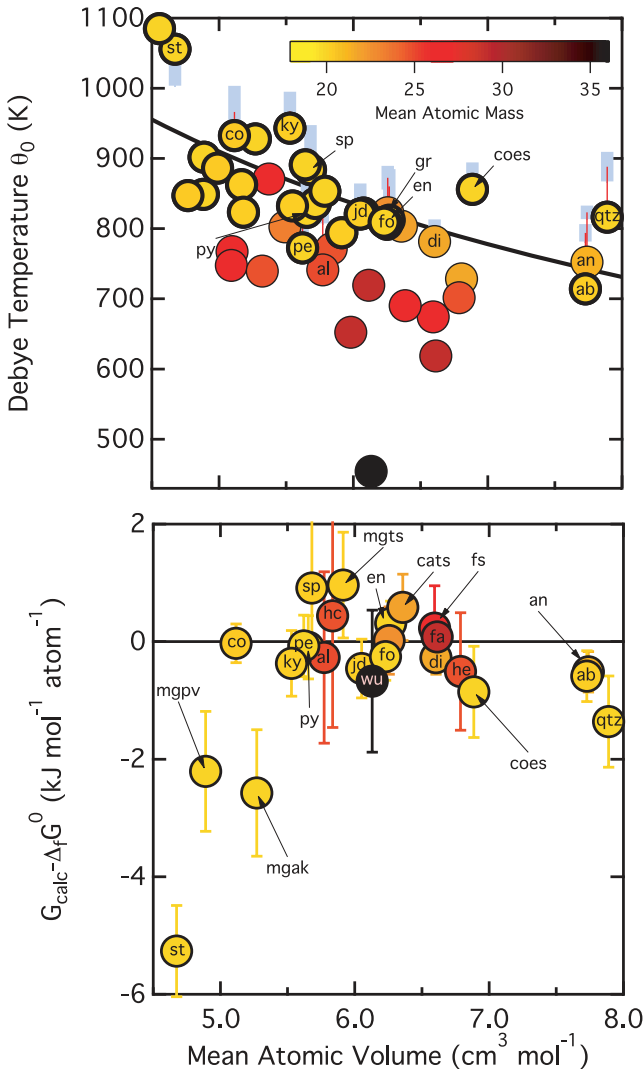


**Figure 7.** Top: our inverted values of  $\theta_0$  (circles) plotted against  $\bar{v}$  for all mantle species with colours indicating values of  $\bar{m}$  according to the scale shown. The blue bars indicate values of  $\theta(0)$  computed from the model vibrational density of states of Kieffer (1980) from eq. (43) in the two approximations featured in that study: either including or neglecting estimated Brillouin zone dispersion of the lower boundary of the optical continuum. Species names label those for which values of  $\theta(0)$  are available, and thin red lines connect estimates to our values of  $\theta_0$ . The black line is the best power-law fit to those species with  $20 < \bar{m} < 21$ , which are outlined in a bold black circle. Bottom: difference between  $\mathcal{G}$  computed from our model at  $P = 0$  and  $T = 298$  K ( $\mathcal{G}_{\text{calc}}$ ) and the experimentally determined Gibbs free energy of formation from the elements  $\Delta_f G^0$  plotted as a function of  $\bar{v}$ .

sible to optical spectroscopy, the remainder of the Brillouin zone can be accessed only by much more specialized techniques such as inelastic neutron scattering (Chaplot *et al.* 2002). This means that experimental knowledge of the dispersion of vibrational modes through the Brillouin zone is lacking for nearly all minerals. In the analysis of Kieffer (1980) two different approximations were explored for the lower limit of the optical continuum: no dispersion, and a decrease in frequency with wave vector proportional to a simple two-mass model. The difference between these approximations exceeds in most cases the uncertainty in our values of  $\theta_0$ .

As expected of a characteristic vibrational frequency, our inverted values of  $\theta_0$  tend to increase with decreasing mean atomic volume  $\bar{v}$  and decreasing mean atomic mass  $\bar{m}$  (Fig. 7). The dependence of  $\theta_0$  on  $\bar{v}$  for those minerals with  $20 < \bar{m} < 21$  can be described as  $\theta_0 \sim A\bar{v}^{-\gamma_{\text{eff}}}$  where  $\gamma_{\text{eff}} = 0.5$  may be thought of as an effective Grüneisen parameter describing, in this case, the variation of characteristic frequency among a suite of structures, rather than the influence of compression in a single structure. While  $\gamma_{\text{eff}}$  has the same magnitude as  $\gamma_0$  of the species that we have considered, it is significantly smaller reflecting the important influence of variables other than  $\bar{v}$  and  $\bar{m}$  including the details of crystal structure. For example,  $\theta_0$  of *mgpv* is less than that of *mgak* even though *mgpv* is the denser phase, reflecting the presence of low frequency octahedral rotational modes in *mgpv* that are absent in *mgak* (Wentzcovitch *et al.* 2004b). Comparable previous analyses of systematic relationships have been performed in terms of the entropy rather than  $\theta_0$ . These analyses have justified relationships between entropy and volume or mass by appeal to the characteristic vibrational frequency, which we instead analyse directly. In any case, the patterns are found to be similar considering the inverse relationship between entropy and  $\theta_0$  (Barron *et al.* 1957): entropy tends to increase with  $\bar{v}$  and with  $\bar{m}$  (Holland 1989; Latimer 1951).

We anticipate values of  $\mathcal{F}_0$  via thermochemical measurements of the Gibbs free energy of formation from the elements  $\Delta_f G^0$  at ambient conditions (Robie & Hemingway 1995) (Fig. 7). The comparison is direct since

$$\mathcal{F} = \mathcal{G} \quad (45)$$

at zero pressure and the quantity  $\mathcal{G} - \mathcal{F} = PV < 1 \text{ J mol}^{-1} \text{ atom}^{-1}$  for minerals at 1 bar, far below experimental uncertainty. Species for which the difference falls outside the combined uncertainty include: (1) High pressure phases for which the experimental values are not measured, but inferred from phase equilibria (*mgak*, *mgpv*). Our determinations are likely to be more accurate in this category as we have considered the physical properties of the phases and the quality of the experimental phase equilibria data in much more detail than previous studies (Appendix A). (2) Stishovite, which shows the largest difference. Our value is likely to be more accurate in this case. The value in Robie & Hemingway (1995) is taken from the study of Holm *et al.* (1967) which differs markedly from more recent determinations which found that the enthalpy of the coesite to stishovite transition was 35 per cent smaller (Akaogi *et al.* 1995; Liu *et al.* 1996). If we assume that all the error in the Holm *et al.* (1967) Gibbs free energy difference lies with stishovite, then the revised value of  $\Delta_f G^0(\text{st}) = -818.5 \text{ kJ mol}^{-1}$  in perfect agreement with our value of  $\mathcal{F}_0$  for *st*. (3) Phases with large mean atomic volume in which the differences are most likely explained by our simplifying assumptions regarding the form of the vibrational density of states (*an*, *ab*, *qtz*). As we argued in Paper I, the errors due to these simplifying assumptions are unlikely to influence the computation of physical properties or phase equilibria at mantle conditions and are likely to be magnified at much lower temperatures than those

relevant to the mantle, and in some cases will exceed experimental uncertainty at temperatures as low as 300 K. The errors are likely to be largest for those solids that have been described as non Debye-like and which can be characterized by the ratio  $r_{20} = \theta(2)/\theta(0)$ . This ratio is unity for a Debye-like solid, i.e. one for which all  $\theta(p)$  are equal by definition (Anderson 1995). The ratio tends to exceed unity for phases with molecular-like modes, such as tectosilicates. Indeed, our analysis of the model vibrational spectra of Kieffer (1980) show  $r_{20} = 1.44$  for anorthite and  $r_{20} = 1.45$  for quartz. These are the largest values of  $r_{20}$  of any species in our study and far exceed the values for closely-packed solids such as *co* (1.04), *pe* (1.05), or even non-close-packed solids such as *fo* (1.23).

The inverted values of the  $W_{\alpha\beta}$  parameters show a tendency to increase with the volume difference between the interacting species (Fig. 8). Such a relationship was previously pointed out by Davies & Navrotsky (1983). The notion underlying the correlation is that the volume difference captures the essential aspects of the energetics of species interactions in solid solutions including mismatch of ionic sizes, coordination number and crystal structure type. Agreement between our values and the best-fitting relationship for homovalent binary compounds with the rock-salt structure (Davies & Navrotsky 1983) is remarkably good for many phases, particularly those involving homovalent cation exchange in *fp*, *fo*, *wa*, *ri*, *gt* (*py-gr*) and *sp*. An exception is homovalent Ca–Mg exchange in *opx* and *cpx*, which fall well above the rock-salt trend. Many other mantle phases also fall above the rock-salt trend, a tendency also evident in the analysis of complex compounds including silicates by Davies & Navrotsky (1983). In the case of solutions related by the  $\text{MgSi} \leftrightarrow \text{AlAl}$  Tschermak substitution [*cpx* (*di-cats*), *ak*, *pv*, *ppv*] this tendency is easily rationalized (Panero *et al.* 2006): heterovalent Mg–Al and Si–Al interactions produce large interaction parameters while affecting the volume only slightly

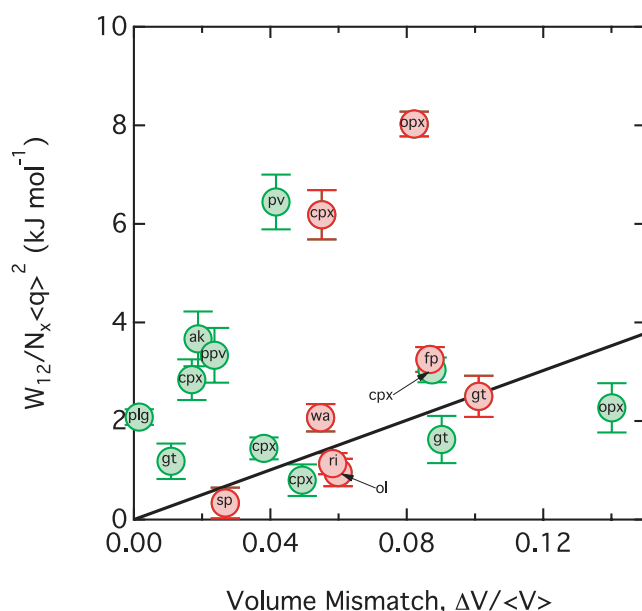


**Figure 8.** Interaction parameters  $W_{12}$  between species plotted against the normalized volume difference  $2|V_2 - V_1|/(V_2 + V_1)$ . To facilitate comparison, the interaction parameters are divided by  $N_x$ , the number of exchangeable cations per species, and the square of  $\langle q \rangle$  the mean charge of the exchangeable cations. Red symbols are for divalent cation exchange on a single site. The solid line is the best fit to divalent compounds from Davies & Navrotsky (1983).

since the mean cation radius on either side of the exchange is similar.

## 6 COMPUTATION

We have developed a method for solving our central problem: given a closed system of known composition, pressure and temperature, find the equilibrium phase assemblage, that is the amounts and compositions of all coexisting phases, and the physical properties of the assemblage. The solution is completely specified by the theory we have described here and in Paper I and by the values of the parameters determined in our global inversion. The computationally challenging part of this problem is the determination of the phase equilibria. Once we know the equilibrium assemblage, physical properties are easily computed via eqs (14)–(18), and equations for the elastic constants given in Paper I.

Minimization of the Gibbs free energy (eq. 6) over the amounts of the species,  $n_i$ , presents at least four numerical challenges:

- (i) The constraint of fixed bulk composition

$$r_{ij}n_j = b_i, \quad (46)$$

where  $r_{ij} = \sum_k s_{ijk}$  is the stoichiometric coefficient matrix, and  $b_i$  is the bulk composition vector.

- (ii) The large number of dimensions. The dimensionality is set by the total number of species, which is in principle almost arbitrarily large and in our present model is 47.

- (iii) The non-negativity constraint

$$\forall j, k : n_{jk} \geq 0. \quad (47)$$

- (iv) The non-linearity of the inversion caused by the logarithmic terms in the chemical potential (eq. 7).

The algorithm that we have developed to meet these challenges is briefly described here and detailed in Appendix B.

We satisfy the bulk composition constraint by performing our minimization search over the null space of the underdetermined linear problem eq. (46). The null space is spanned by vectors corresponding to the linearly independent set of chemical reactions that leave the bulk composition invariant. This strategy also has the advantage of reducing the dimensionality of the minimization problem from  $s$ , the number of species, to  $s - c$ . The non-negativity constraint is addressed by explicitly removing species when their abundance falls below a threshold that depends on machine precision. Removal of species also further reduces the dimensionality of the search space and serves as an effective means of handling the divergence of the logarithmic term in the limit of vanishingly small  $n_i$ . Species are added when their chemical affinity becomes favourable. We have found this algorithm to be efficient and robust. Some examples illustrating the minimization algorithm are given in Appendix B.

## 7 MANTLE PHASE EQUILIBRIA

We compare the results of our method to experimental phase equilibria in a wide variety of systems spanning the entire mantle pressure–temperature range in order to: (1) demonstrate the quality of the global inversion, (2) highlight regions where further experimental constraints are needed but do not yet exist, (3) illustrate predictions of the model beyond what is uniquely constrained by present experimental data and (4) point out areas of discrepancy where further developments in the model or in experimental methodology may be required.

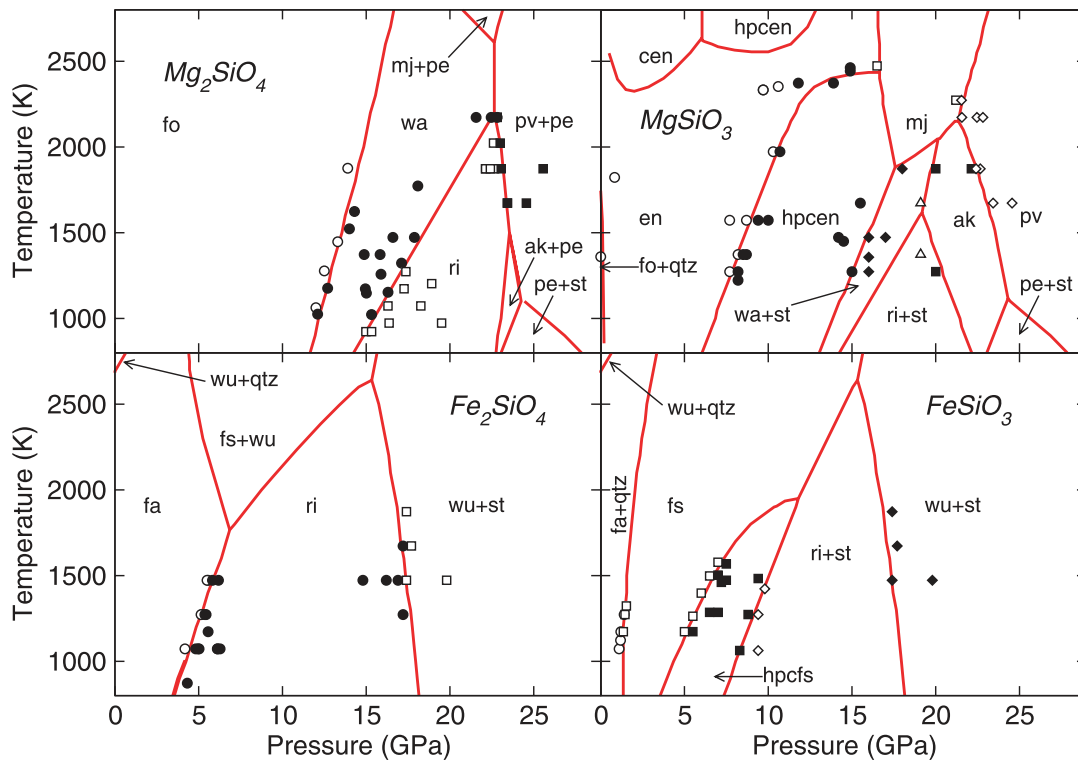


**Figure 9.** Phase diagrams computed with our model (red) compared with experimental observations as follows.  $\text{Mg}_2\text{SiO}_4$  diagram: *fo* ○; *wa* ●; *ri* □; *pv+pe* ■.  $\text{MgSiO}_3$  diagram: *en* ○; *hpcen* ●; *mj* □; *wa+st* ◆; *ri+st* △; *ak* ■; *pv* ◇.  $\text{Fe}_2\text{SiO}_4$  diagram: *fa* ○; *ri* ●; *wu+st* □.  $\text{FeSiO}_3$  diagram: *fa+qtz* ○; *fs* □; *hpcfs* ■; *ri+st* ◇; *wu+st* ◆. References to experimental data are given in Table A4. We identify phases by unique end-member names when they exist (e.g. *fa*, *fo*, *en*, etc., rather than *ol*, *ol*, *opx*), and use the phase name where no specific end-member name exists (*wa*, *ri*, etc., rather than *mgwa*, *mgri*).

Comparison with experimental data for  $\text{Mg}_2\text{SiO}_4$ ,  $\text{MgSiO}_3$ ,  $\text{Fe}_2\text{SiO}_4$  and  $\text{FeSiO}_3$  bulk compositions show excellent agreement with experimental data (Fig. 9). These computed phase diagrams serve to illustrate some aspects of our approach. We identify all phase stability fields within our model, not only the subset of these that have been experimentally observed. For example, the stability field of *ak+pe* in  $\text{Mg}_2\text{SiO}_4$  has not been observed experimentally, yet it does not violate experimental observations. Moreover, this stability field is required if the *ak* = *pv* transition has a more negative  $dP/dT$  Clapeyron slope than the *ri* = *pv* + *pe* transition, as our model and experiments indicate (Fei *et al.* 2004). The presence of an *ak+pe* stability field was previously predicted on the basis of a Schreinemaker-type analysis (Jeanloz & Thompson 1983).

We compute solid-state phase equilibria to temperatures much greater than the melting curve in which case our computed equilibria are fictive. Computing phase transitions in this regime serves important purposes: (1) It can reveal energetic relationships among phases in a way that might not be apparent within the experimentally accessible subsolidus  $P$ – $T$  regime. (2) It can reveal relationships between simple bulk compositions and more complex bulk compositions. As an illustration of the latter, consider the appearance of the fictive *mj+pe* stability field in  $\text{Mg}_2\text{SiO}_4$  at supersolidus conditions. We anticipate that this stability field will expand substantially upon the addition of Al, which will tend to stabilize garnet at the expense of the orthosilicates. The fictive supersolidus stability fields of *hpcen* and *cen* highlight open questions of the relative stability of a large number of pyroxene polymorphs that differ by very subtle structural distortions (Jackson *et al.* 2004). We have not included all of these modifications in our model, including the well known

proto-pyroxene (Boyd *et al.* 1964) or low clinopyroxene (Grover 1972), or the less well established high-temperature clinopyroxene (*htcpx*) (Shimobayashi & Kitamura 1991) and high temperature orthopyroxene (*htopx*) (Miyake *et al.* 2004; Ohi *et al.* 2008), because they are not likely to have wide stability fields in whole rock compositions. The appearance of *fo+qtz* at very low pressures on the  $\text{MgSiO}_3$  diagram is likely due to our neglect of the low clinopyroxene phase.

The  $\text{Mg}_2\text{SiO}_4$ – $\text{Fe}_2\text{SiO}_4$  system provides a first order understanding of seismic discontinuities near 410 and 660 km depth (Fig. 10). Our model reproduces the very sharp divariant transition from *ol* to *wa* and the even sharper transition from *ri* to *pv+fp* that has been seen in previous studies (Ito & Takahashi 1989; Frost 2003b). As compared with the  $\text{MgO}$ – $\text{SiO}_2$  system, the effect of adding FeO is to destabilize *wa* and *pv* in favour of *ri* and *fp+st*, respectively, in agreement with experiment. Our model matches experimental data on *ol*–*wa*–*ri* compositions as well as the system-specific model of Frost (2003b). Our computed *pv+fp* = *fp+st* compositions are consistent with experimental data, although agreement could be marginally improved by including a non-zero  $W_{\text{mgpv} \rightarrow \text{fevp}}$  in our model. We have not added this parameter, because it is poorly constrained, and because *pv* = *fp* Fe partitioning will probably be influenced by spin-pairing transitions, which we have not yet included in our model.

Addition of the  $\text{Al}_2\text{O}_3$  component to  $\text{MgSiO}_3$  stabilizes garnet at the expense of other phases (Fig. 10). Comparison with experiment illustrates a potentially valuable application of thermodynamic models. At high pressure ( $P > 20$  GPa) there is a tendency for our model to predict narrower one-phase fields in this diagram than are indicated experimentally. This may signal a systematic bias in

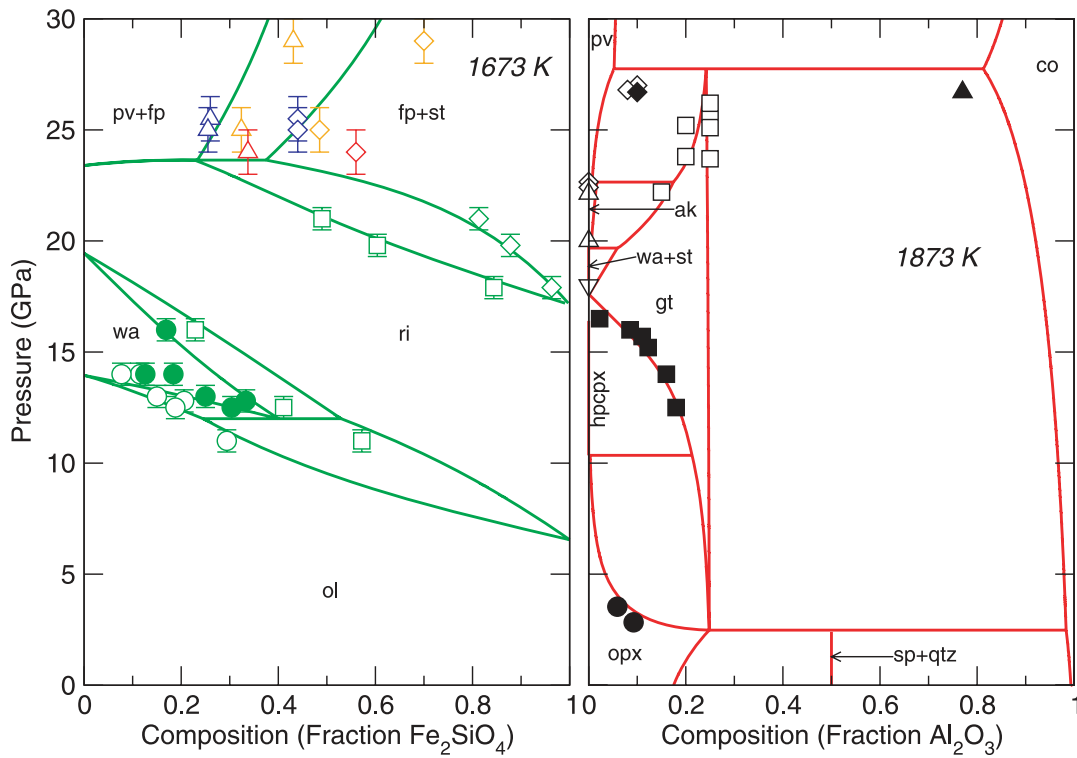


**Figure 10.** Left:  $\text{Mg}_2\text{SiO}_4$ – $\text{Fe}_2\text{SiO}_4$  phase diagram computed with our model at 1673 K (green) compared with experimental observations of the compositions of the following phases in divariant coexistence: *ol* (open circles); *wa* (closed circles); *ri* (open squares); *fp* (open diamonds); *pv* (open triangles) at: 1373 K (blue); 1673 K (green); 1773 K (orange); 1873 K (red). Experimental data:  $P < 17$  GPa (Frost 2003b);  $P = 17 - 22$  GPa (Matsuzaka *et al.* 2000);  $P > 22$  GPa:  $T = 1373, 1873$  K (Ito & Takahashi 1989);  $T = 1773$  K (Tange *et al.* 2009). Composition is plotted as the mole fraction  $\text{Fe}_2\text{SiO}_4/(\text{Mg}_2\text{SiO}_4 + \text{Fe}_2\text{SiO}_4)$ . Right:  $\text{MgSiO}_3$ – $\text{Al}_2\text{O}_3$  phase diagram computed with our model at 1873 K (red) compared with experimental observations of the compositions in divariant coexistence (closed symbols) or stability (open symbols) of the following assemblages: *opx* (circles); *gt* (squares); *pv* (diamonds); *ak-co* (triangles); *wa+st* (downward-pointing triangles). Experimental data: *opx* (at 1773 K Perkins *et al.* 1981); *gt* compositions (upper bound on *pv* contents at 1923 K Gasparik 1989); *gt* stability (Kubo & Akaogi 2000); *wa+st* (Ito & Navrotsky 1985); *ak* stability (Ito & Navrotsky 1985; Fei *et al.* 2004); *mgpv* stability (Fei *et al.* 2004); other *pv* stability, *pv* composition, and *co*-rich *ak* composition (Kubo & Akaogi 2000). Composition is plotted as the mole fraction  $\text{Al}_2\text{O}_3/(\text{MgSiO}_3 + \text{Al}_2\text{O}_3)$ .

our model, or systematic experimental error. The latter might arise from kinetic hindrances to disproportionation reactions, which may be particularly severe in this system: for example, formation of coexisting *pv*+*gt* from an initially homogeneous sample requires diffusion of Al on the grain scale, which can be slow (Kubo *et al.* 2008).

Addition of  $\text{Na}_2\text{O}$  and  $\text{CaO}$  components to  $\text{MgSiO}_3$  stabilizes garnet and clinopyroxene at the expense of other phases (Fig. 11). For example *cpx* is stabilized deep into the transition zone near the diopside and jadeite end-members (to 18 and 24 GPa, respectively). Phase equilibria on the *en-di* composition join agree with those of Gasparik (1990a) except that we have not included the high-pressure Ca-rich ‘CM’ phase found in that study, but not in other studies of mantle phase equilibria. The topology of our computed *en-jd* composition join is similar to that of Gasparik (1992) except that our *cpx*+*gt* coexistence field is shifted to more *en*-rich compositions. This disagreement may point to the need to include a non-ideal *mgmj*–*jdmj* interaction parameter, which we have neglected, or for the need for further experiments to reproduce the details of high pressure equilibria on this join. A large non-ideal interaction would also be necessary to reproduce the two-garnet miscibility gap computed by Gasparik (1992).

The transformations from *plg*- to *sp*- to *gt*-bearing peridotite in the CMAS system demonstrate that accurate description of complex phase equilibria can be accomplished with a limited and therefore robust set of parameters that are constrained almost

entirely by measurements on binary joins (Fig. 12). Our results agree very well with experimental measurements of phase compositions. Disagreements are generally due to mutual inconsistency of different experiments. We have fit to the data of Perkins & Newton (1980) and Klemme & O’Neill (2000) because the greatest care was taken in these experiments to ensure equilibrium. Our model shows the well known patterns in this system: Al content of the pyroxenes are similar and increase with pressure in the *plg* stability field, remain nearly constant with pressure in the *sp* stability field and decrease with increasing pressure in the *gt* stability field. The boundaries of the *sp* stability field in these curves are marked by breaks in slope, which demonstrate that our model correctly reproduces the positive Clapeyron slope of the *sp*-peridotite to *gt*-peridotite transition (Klemme & O’Neill 2000), and predicts a negative Clapeyron slope for the *plg*-peridotite to *sp*-peridotite transition between 1173 K to the solidus, which is consistent with limited experimental data (Kushiro & Yoder 1966). As an illustration of the power of the asymmetric van Laar formulation, our solution model for CMAS *cpx* consists of only four parameters:  $W_{di-cats}$ ,  $W_{di-cen}$ ,  $W_{cats-cen}$ ,  $d_{cats}$ , all of which are assumed to be independent of  $P$  and  $T$ , and fewer for *opx* and *gt*. In comparison, the model of Gasparik (1984b), which fits the experimental data no better, invokes eight parameters for CMAS *cpx* ( $A_{cen-di}$ ,  $B_{cen-di}$ ,  $A_{cen-di}^V$ ,  $B_{cen-di}^V$ ,  $A_{cen-alumina}$ ,  $A_{cen-alumina}^S$ ,  $B_{cen-alumina}$ ,  $C_{cen-alumina}$ ), where the latter four are constrained only by measurements in the full CMAS system.

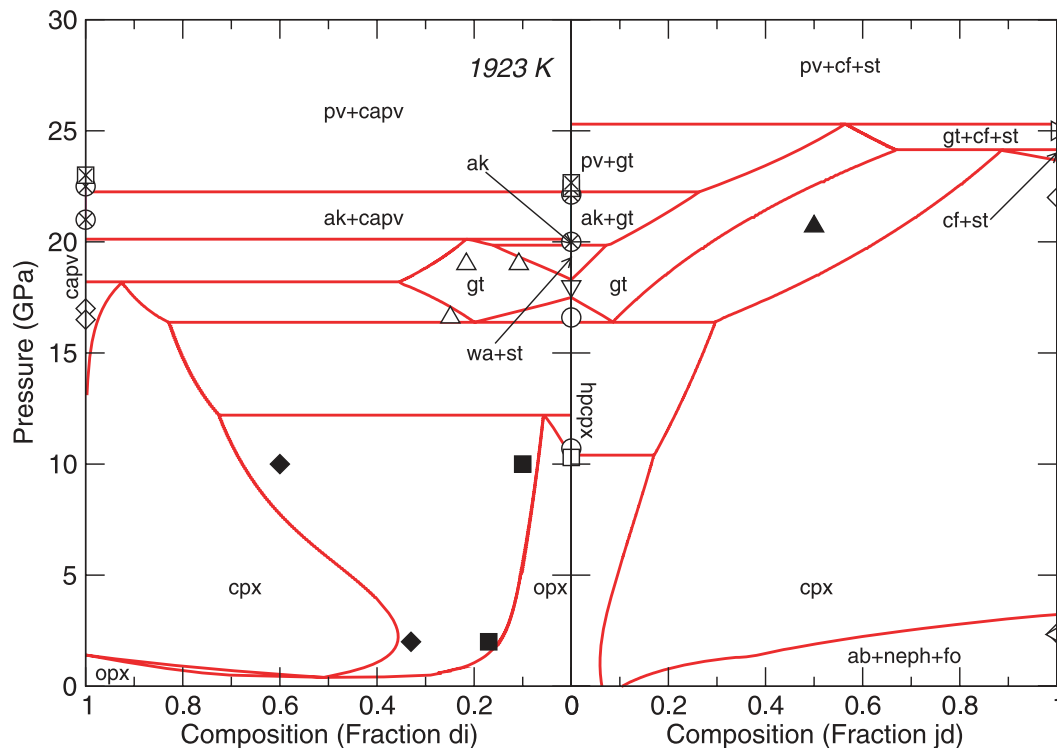


**Figure 11.** Left:  $\text{CaMgSi}_2\text{O}_6$ – $\text{Mg}_2\text{Si}_2\text{O}_6$ . Right:  $\text{Mg}_2\text{Si}_2\text{O}_6$ – $\text{NaAlSi}_2\text{O}_6$  phase diagrams computed with our model at 1923 K (red) compared with experimental observations of compositions in divariant coexistence (closed symbols) or stability (open symbols) of the following assemblages: *opx* (squares); *cpx* (diamonds); *hpcpx* (circles); *gt* (up triangles); *wa+st* (down triangles); *ak ± capv* (crossed circles); *pv ± capv* (crossed squares); *ab+neph* (left triangle); *cf+st* (right triangle). Experimental data  $1873 \leq T \leq 1973$  K unless otherwise noted: *opx* and *cpx* compositions (Gasparik 1990b); *opx* and *hpcpx* stability ( $P < 12$  GPa Pacalo & Gasparik 1990); other *hpcpx* stability (Gasparik 1990a); *cpx* stability (Canil 1994; Akaogi *et al.* 2004; Liu 2006), (at 1473 K Gasparik 1985); *ab+neph* stability (at 1473 K Gasparik 1985); *cf+st* stability (Liu 2006); *wa+st* (Ito & Navrotsky 1985); *gt* stability (Gasparik 1990a; Akaogi *et al.* 2004); *gt* composition (Gasparik 1992); *ak* stability (Ito & Navrotsky 1985; Fei *et al.* 2004); *pv* stability (Fei *et al.* 2004); *ak+capv* and *pv+capv* stability (Akaogi *et al.* 2004). Composition is plotted as the mole fraction (left)  $\text{CaMg}/(\text{CaMg}+\text{MgMg})$ ; (right)  $\text{NaAl}/(\text{NaAl}+\text{MgMg})$ .

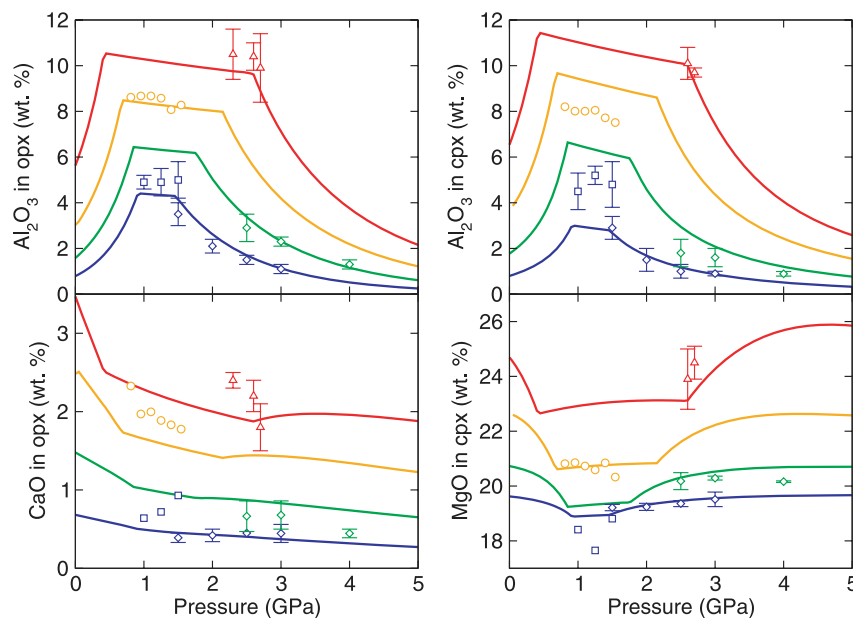


**Figure 12.** Variation of pyroxene composition with pressure computed from our model along the isotherms: (red) 1773 K; (orange) 1573 K; (green) 1373 K; (blue) 1173 K; compared with experimental data: (triangles Klemme & O'Neill 2000); (circles Gasparik 1984a); (diamonds Perkins & Newton 1980) and (squares Sen 1985).

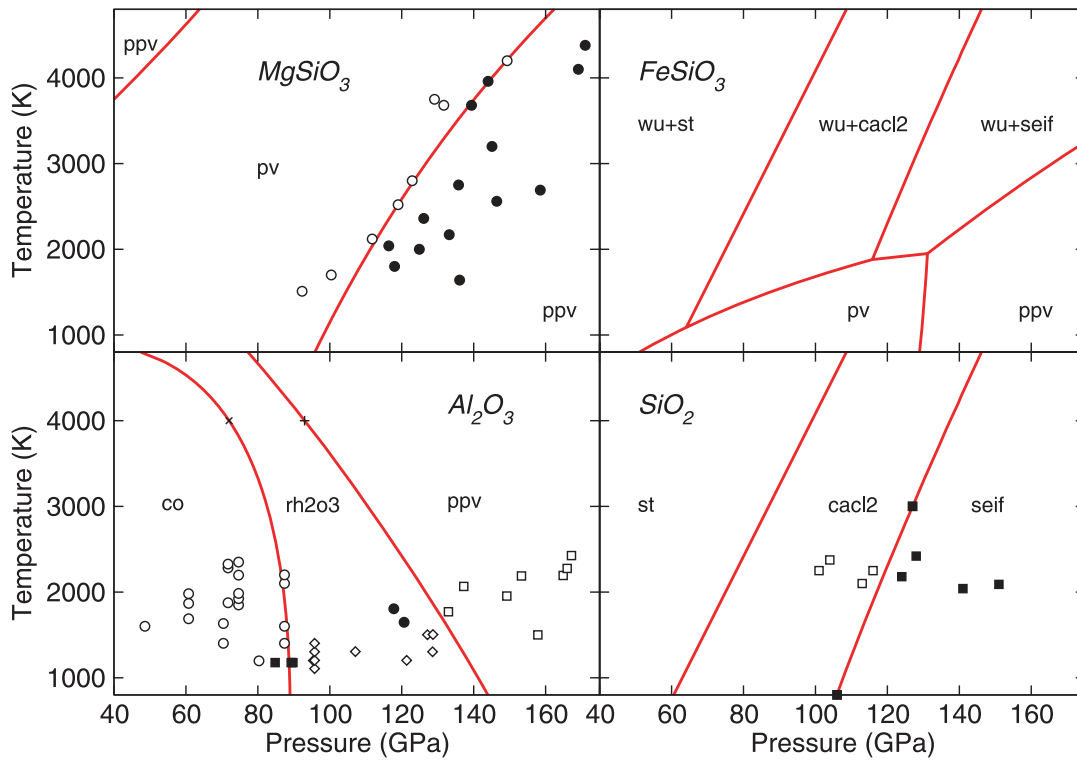


**Figure 13.** Phase diagrams computed with our model (red) compared with experimental observations as follows.  $\text{MgSiO}_3$  diagram:  $pv$   $\circ$ ;  $ppv$   $\bullet$  (Tateno *et al.* 2009).  $\text{Al}_2\text{O}_3$ :  $co$  only  $\circ$ ;  $rh2o3+co$  on compression  $\diamond$ ;  $rh2o3+co$  on decompression  $\blacksquare$ ; (Lin *et al.* 2004)  $rh2o3$  only  $\bullet$ ;  $ppv$  only  $\square$  (Ono *et al.* 2006).  $\text{SiO}_2$ :  $cac12$   $\square$ ;  $seif$   $\blacksquare$  (Murakami *et al.* 2003). The cross and square represent, respectively, the location of the  $co = rh2o3$  and  $rh2o3 = appv$  transformations at 4000 K in the first principles calculations of Tsuchiya *et al.* (2005). Note that the secondary  $ppv$  stability field at extreme supersolidus conditions and relatively low pressure in  $\text{MgSiO}_3$ , cannot be ruled out by present experimental data, but is also not likely to be robust as its position and existence depend on extrapolations of the Gibbs free energies of  $pv$  and  $ppv$  far beyond the regime of experimental constraints.

Phase equilibria at lower mantle conditions illustrate the scope of our approach, which encompasses the entire mantle regime of pressure and temperature (Fig. 13). Because of the large pressure and temperature ranges involved, several phase boundaries are noticeably curved. The curvature originates in the self-consistency of our approach. Because the phase equilibria and physical properties are computed self-consistently, changes in the volume and entropy contrasts between two phases will alter the Clapeyron slope of the phase boundary between them. Thus changes in the difference between the volume and entropy of  $pv$  and  $ppv$  with  $P$  and  $T$  lead to marked curvature of the  $pv = ppv$  phase boundary. The curvature that we find in our model matches the experimental phase equilibria somewhat better than the straight-line approximation assumed by the experimentalists (Tateno *et al.* 2009). Our computed phase diagram of  $\text{Al}_2\text{O}_3$  is consistent with experimental data even though no experiments were used to constrain the relative energetics of the three phases. The reason we did not use experimental data in this case is that for  $co = rh2o3$ , no experiments have produced pure  $rh2o3$  in the vicinity of this transition, while in the case of  $rh2o3 = ppv$ , the data are still too widely separated to constrain even the sign of the Clapeyron slope. Instead we relied on first principles predictions of the phase diagram (Tsuchiya *et al.* 2005). The  $\text{FeSiO}_3$  phase diagram at lower mantle conditions is constrained primarily by Mg–Fe partitioning between the pairs:  $pv$ – $fp$  (Martinez *et al.* 1997; Sinmyo *et al.* 2008) and  $pv$ – $ppv$  (Hirose *et al.* 2008). The calculated stability field of  $pv$  in the  $\text{FeSiO}_3$  system has not been seen experimentally, as Fe enrichment favours the oxides at the expense of  $pv$  (Ito & Takahashi 1989), yet it is consistent with present

knowledge: 1) The computed Clapeyron slope of the oxides =  $pv$  boundary shows that  $\text{FeSiO}_3$  is increasingly stabilized in  $pv$  with increasing pressure, consistent with the experimental observation that the maximum solubility of  $\text{FeSiO}_3$  in  $pv$  increases with increasing pressure. 2) The calculated pressure of the oxides =  $pv$  boundary is consistent with the largest observed  $\text{FeSiO}_3$  content in  $pv$  ( $X_{\text{Fe}} = 30$  per cent) at 40 GPa, which sets a lower bound on the pressure of the transition (Tange *et al.* 2009). Our results for  $\text{FeSiO}_3$  contrast with the results of first principles calculations that show  $ppv$  to be more stable than  $pv$  at all pressures (Caracas & Cohen 2005; Stackhouse *et al.* 2006a). The likely reason for this discrepancy is approximations in the first principles calculations. The calculations neglect the local Hubbard type repulsion of Fe 3d electrons, which can have an important influence on phase stability (Stackhouse *et al.* 2010).

Phase diagrams on the  $\text{MgSiO}_3$ – $\text{FeSiO}_3$  and  $\text{MgSiO}_3$ – $\text{Al}_2\text{O}_3$  joins illustrate the influence of solid solution on phase stability in the lower mantle (Fig. 14). In agreement with observations on the  $\text{MgSiO}_3$ – $\text{FeSiO}_3$  join (Ohtani *et al.* 1991) we find a  $mj$  stability field spanning a substantial range of composition. The presence of this field illustrates our choice of species. On this join, Al-free Mg–Fe majorites have the composition:  $\text{mgmj} + \frac{4X_{\text{Fe}}}{3}\text{al} - \frac{4X_{\text{Fe}}}{3}\text{py}$  with  $X_{\text{Fe}} \leq 3/4$ , where the inequality arises from the non-negativity conditions (eq. 47). Thus the Gibbs free energy minimization algorithm automatically produces majorite on this join without the need to introduce an additional garnet species such as Fe-majorite. In agreement with previous studies, we find that the solubility of  $\text{FeSiO}_3$  in  $pv$  increases markedly over the mantle pressure regime

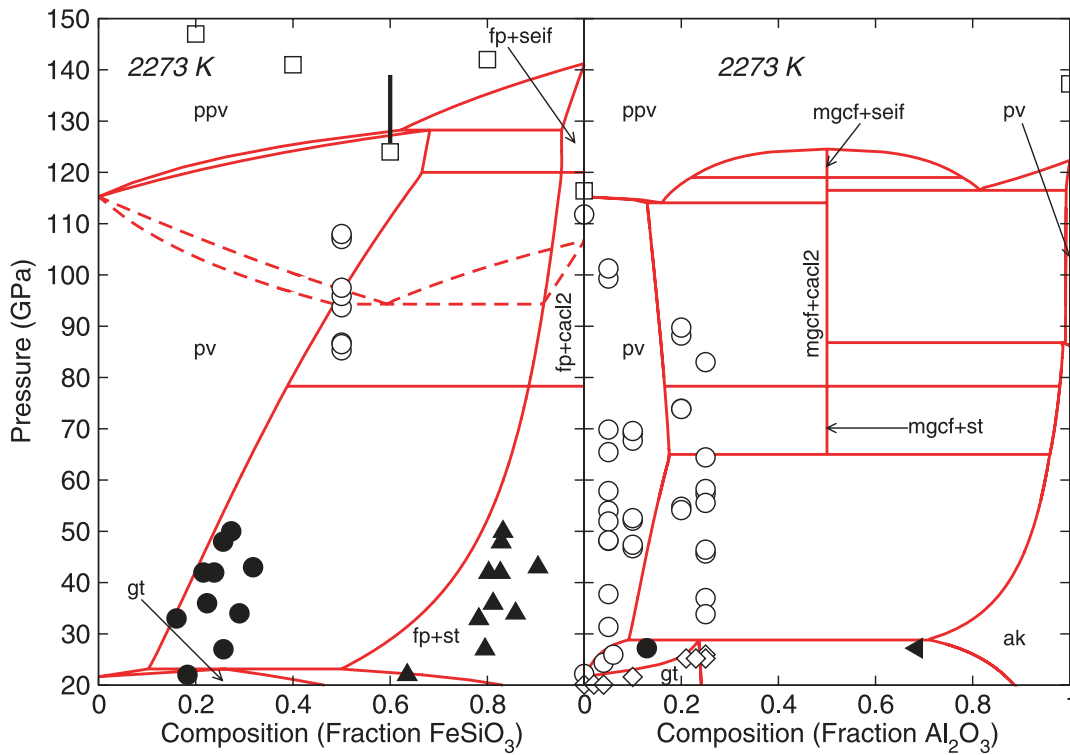


**Figure 14.** Phase diagrams computed with our model at 2273 K (red) compared with experimental observations of compositions in divariant coexistence (closed symbols) or stability (open symbols). In the left-hand diagram two computed results are shown: our standard model (solid red lines) and an alternative model discussed in the text (dashed). Left-hand diagram: *pv* (circles); *fp+st* (triangles); *ppv* (squares). Experimental data: *pv* and *fp+st* compositions (Tange *et al.* 2009); *pv* stability at 1800–2330 K (Tateno *et al.* 2007); *ppv* stability at 2000 K and vertical bar indicating possible uncertainty in pressure calibration (Mao *et al.* 2005). Composition is plotted as the mole fraction  $\text{FeSiO}_3/(\text{MgSiO}_3 + \text{FeSiO}_3)$ . Right-hand diagram: *gt* (diamonds); *pv* (circles); *ak* (left-pointing triangle); *ppv* (squares). Experimental data: *gt* and *pv* stability at  $P < 30$  GPa with pressure based on the Au scale as corrected by Fei *et al.* (2004) (Hirose *et al.* 2001a); *pv* stability at  $30 < P < 100$  GPa and 2000–2600 K (Walter *et al.* 2004); *pv* and *ppv* stability at  $P > 100$  GPa and 2000–2200 K (Tateno *et al.* 2009); *pv* and *co-rich ak* compositions at 2173 K (Kubo & Akaogi 2000). Composition is plotted as the mole fraction  $\text{Al}_2\text{O}_3/(\text{MgSiO}_3 + \text{Al}_2\text{O}_3)$ .

(Mao *et al.* 1997). Indeed, the trend computed by our method underestimates the solubility at high pressure somewhat as compared with the most recent experimental results (Tange *et al.* 2009). This discrepancy may be related to spin-pairing transitions which we have not attempted to include in our model. We also find a wide stability field of *ppv* on this join, in agreement with previous studies (Mao *et al.* 2005). The magnitude and even the sense of Mg–Fe partitioning between *pv* and *ppv* is currently highly uncertain with several conflicting experimental results. Our *pv* = *ppv* phase loop is constrained primarily by the partitioning data of Hirose *et al.* (2008). To illustrate the uncertainties, we have performed an alternative global inversion, this time using the *ppv* = *fp* Mg–Fe partitioning datum of Auzende *et al.* (2008) instead of that from Hirose *et al.* (2008) (Fig. 14 left, dashed lines). The alternative datum has the effect of stabilizing *ppv* at the expense of *pv* with increasing iron content, and reversing the sign of the  $dP/dX_{\text{Fe}}$  slope of the *pv* = *ppv* coexistence loop. The  $\text{MgSiO}_3$ – $\text{Al}_2\text{O}_3$  phase diagram shows a wide stability field of *mgcf* + silica coexisting with either Mg-rich or Al-rich *pv* or *ppv*, or Al-rich *ak*, depending on pressure and composition. The *mgcf* + *st* assemblage is stabilized at high pressure by its greater density: the volume of the reaction  $\text{mgpv} + \text{co} = \text{mgcf} + \text{st}$  is negative at lower mantle pressures. Previous estimates of this phase diagram are very different as they have not considered the possibility of the *mgcf* + silica assemblages (Tsuchiya & Tsuchiya 2008; Ohtani & Sakai 2008).

## 8 APPLICATIONS

The variation of temperature with depth over much of the convecting mantle is governed by the effects of isentropic compression. Deviations from isentropic temperature profiles occur in thermal boundary layers, and due to the effects of radioactive heating, phase transformations, and spherical geometry. Isentropic temperature profiles serve as a useful reference state from which to measure radial and lateral temperature variations in the mantle. The potential temperature  $T_p$  is the temperature that a material parcel cools to on isentropic ascent. Conventionally, the definition of potential temperature neglects the influence of decompression melting near the surface. This makes our melt-free formulation ideal for computing mantle isentropes.

We have used our method to compute self-consistently the isentropes of a six-component pyrolite model of the MORB source region (Workman & Hart 2005) (Fig. 15). The computed isentropes show the well-known property of diverging on compression: the difference in temperature between the  $T_p = 1000$  and 2000 K isentropes reaches 1730 K at the core–mantle boundary. The origin of this divergence is readily seen by writing the isentropic gradient of a homogeneous material

$$\left(\frac{\partial T}{\partial P}\right)_S = \frac{\gamma T}{K_S} \quad (48)$$

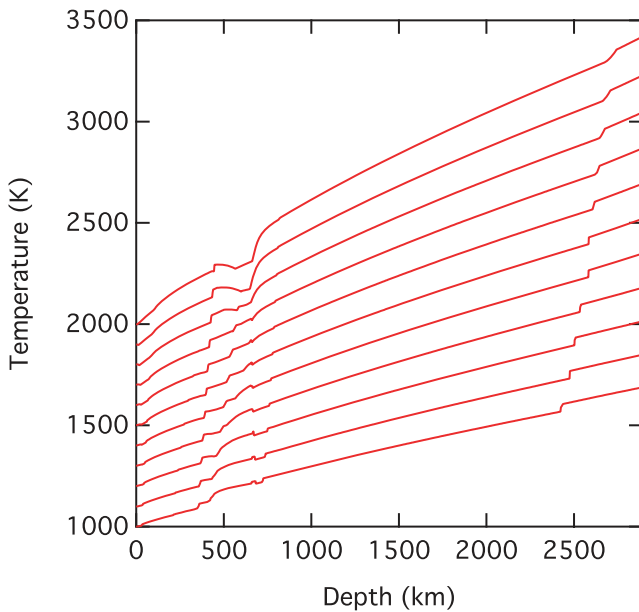


**Figure 15.** Isentropes of a model pyrolite composition computed with our method.

which shows that the gradient increases with increasing temperature at a given pressure. The sense of curvature of the isentropes is also easily rationalized from eq. (48) and the following comparison

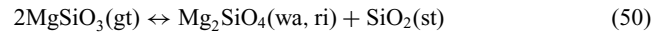
$$\left( \frac{\partial \ln K_S}{\partial \ln \rho} \right)_s \sim K' > \left( \frac{\partial \ln T}{\partial \ln \rho} \right)_s = \gamma \quad (49)$$

so that along a given isentrope, the gradient diminishes with increasing pressure because  $K_S$  increases more rapidly than  $T$  on compression: for mantle materials typical values are  $K' \sim 4 > \gamma \sim 1.5$ . The value of  $\gamma$  also decreases on compression, further contributing to the negative curvature. Isentropes are deflected at phase transformations according to the Verhoogen effect (Verhoogen 1965): the temperature increment is related to the latent heat of transformation.

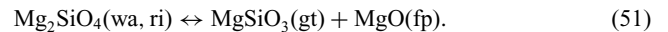
The phase diagram of whole rock mantle compositions is an essential element of mantle convection models and our interpretation of seismological mantle structure. We apply our method to the computation of the phase diagram of a six-component pyrolite model of the MORB source region (Workman & Hart 2005) (Fig. 16). Along the self-consistently computed 1600 K isentrope, the phase diagram reveals the familiar transitions from *plg*- to *sp*- to *gt*-bearing peridotite, the transitions among the olivine polymorphs (*ol*, *wa*, *ri*) and the formation of assemblages dominated by *pv* at lower mantle conditions. The phase diagram is shaded according to the density of the assemblage at ambient conditions. Using the ambient density, rather than the density at pressure and temperature serves to highlight the contributions of phase transformations and variations in phase composition to the physical properties of the mantle (Akaogi & Akimoto 1977). For example, the increase in zero pressure density with increasing pressure within the *ol*+*gt*+*cpx*+*opx* field is due mostly to pressure induced variations in the equilibrium composition of the garnet phase as it absorbs the  $\text{MgSiO}_3$  component from the pyroxenes. The variation with pressure of the composition of *gt*, *opx* and *cpx* in peridotites is further illustrated in Fig. 4, which shows that the shear modulus of garnet is also significantly affected by variations in equilibrium composition. The zero pressure shear modulus of garnets varies by 10 per cent over the range of compositions expected in the mantle, a change in the shear modulus

comparable to the change caused by changing the temperature by 1000 K or the pressure by 7 GPa.

The computed diagram highlights an important feature of mantle phase equilibria that has not been widely recognized (Fig. 16). Akaogi & Akimoto (1979) showed that, along typical mantle geotherms, mantle phase equilibria in much of the upper mantle and transition zone could be described in terms of two subsystems that couple weakly: (1) the olivine subsystem, consisting of olivine and its higher-pressure polymorphs and (2) the residuum, consisting of all phases other than the olivine polymorphs, and including *gt*, *opx*, *cpx* and *capv*. In this picture, the two subsystems can be studied separately, greatly simplifying the design of phase equilibrium experiments. Coupling due to Mg–Fe partitioning between the two subsystems does not depend strongly on pressure, although it does have an important influence on the width of phase transformations, with important implications for understanding mantle discontinuities (Stixrude 1997; Irifune & Isshiki 1998). We find that the division of whole rock compositions into two subsystems applies only to a narrow range of temperatures about the typical geotherm defined by the 1600 K isentrope. This range is bounded at lower temperatures by the appearance of *st* via the reaction



and at higher temperature by the appearance of *fp* via



These reactions are apparent in the end-member  $\text{MgSiO}_3$  and  $\text{Mg}_2\text{SiO}_4$  phase diagrams (Fig. 9) and are shifted in pressure and temperature in the whole rock composition by the influence of other components. The *fp*-forming reaction is shifted to lower temperature by the addition of  $\text{Al}_2\text{O}_3$ , which tends to stabilize *gt*, and the *st*-forming reaction is shifted to higher temperature by the addition of FeO, which tends to stabilize *ri*+*st* at the expense of *gt*. Experimental studies on whole rock peridotite compositions have also found evidence for *gt*+*fp*-bearing assemblages at high temperature (Hirose 2002), and *st*-bearing assemblages at low temperatures (Irifune & Ringwood 1987).

The variation of the shear wave velocity of pyrolite along the 1600 K adiabat illustrates the influence of phase transformations on mantle structure (Fig. 17). Substantial jumps in velocity occur over narrow depth ranges near 410, 520, 660 and 2610 km depth, associated with the *ol* = *wa*, *wa* = *ri*, *ri* = *pv*+*fp* and *pv* = *ppv* reactions, respectively. The enhanced velocity gradient from 660 to 790 km depth, due to the dissolution of *gt* into *pv*, is also a feature of many global seismological models (Dziewonski & Anderson 1981). A smaller velocity jump occurs at the *opx*=*hpcpx* transition and broader velocity increases are associated with transitions from *plg*- to *sp*- to *gt*-bearing peridotite assemblages in the upper 100 km. A further velocity jump near 790 km depth is unlikely to be realistic. This feature is associated with a *gt*=*cf* reaction that is unlikely to exist in the mantle as *pv*, rather than *cf* will become the dominant Na-bearing phase in pyrolite compositions, while *cf* dominates in basaltic compositions. We have not yet included a Na-bearing *pv* species in our model because experimental constraints on its properties are essentially non-existent. Other than the appearance of *cf*, our computed phase diagram is consistent with experimental phase equilibrium data (Irifune 1994; Irifune & Isshiki 1998).

## 9 CONCLUSIONS

Developments in the computation of phase diagrams have been driven primarily by a need to understand relatively low pressure

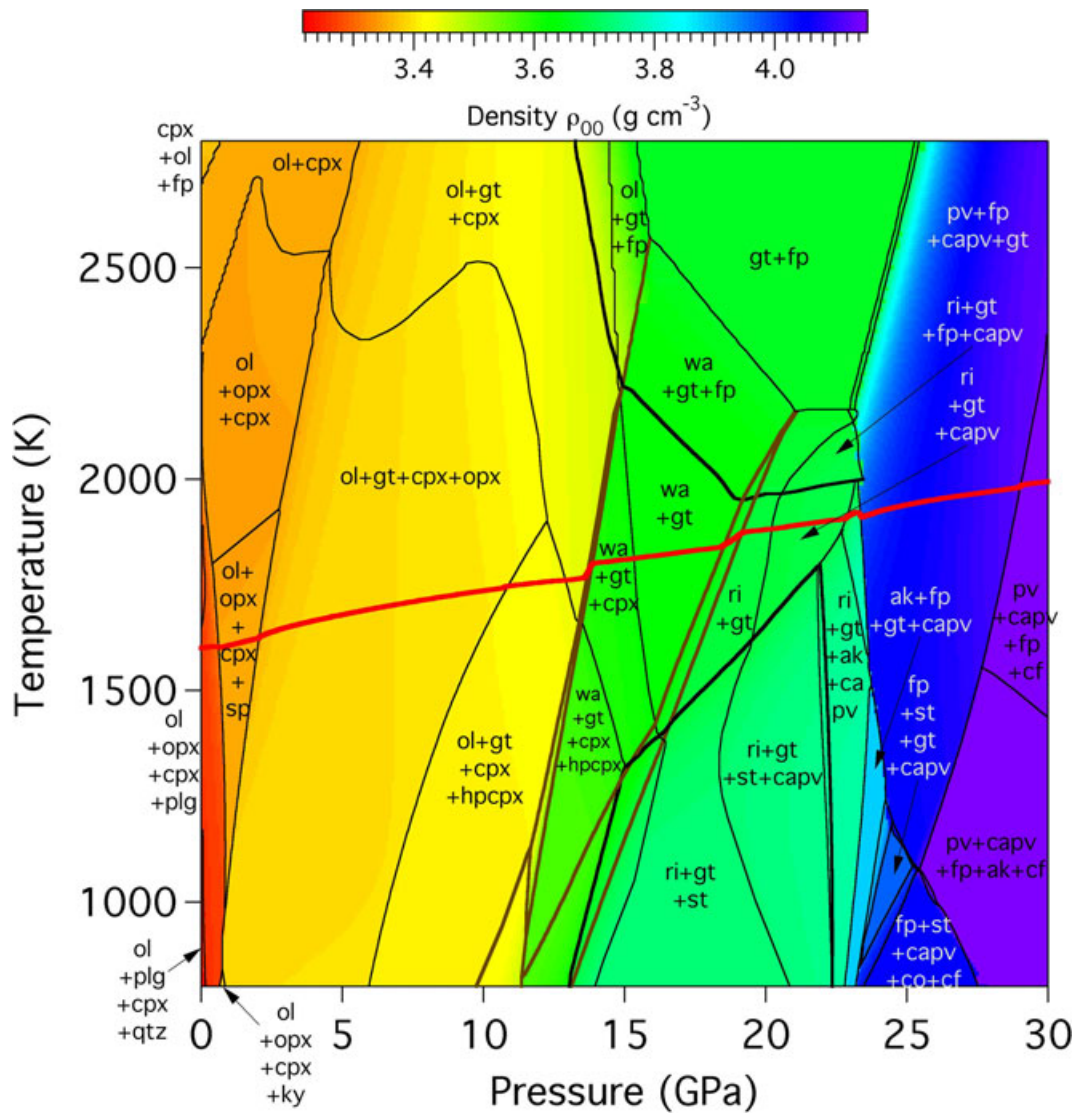


**Figure 16.** Phase diagram of a model pyrolite composition computed from our model showing phase boundaries and the zero-pressure density of the assemblage according to the scale bar at the top. Phase boundaries are shown as thin black lines except those among the olivine polymorphs (brown lines), and the reactions forming *st* and *fp* in the transition zone (bold black lines). Also plotted (bold red) is the 1600 K isentrope.

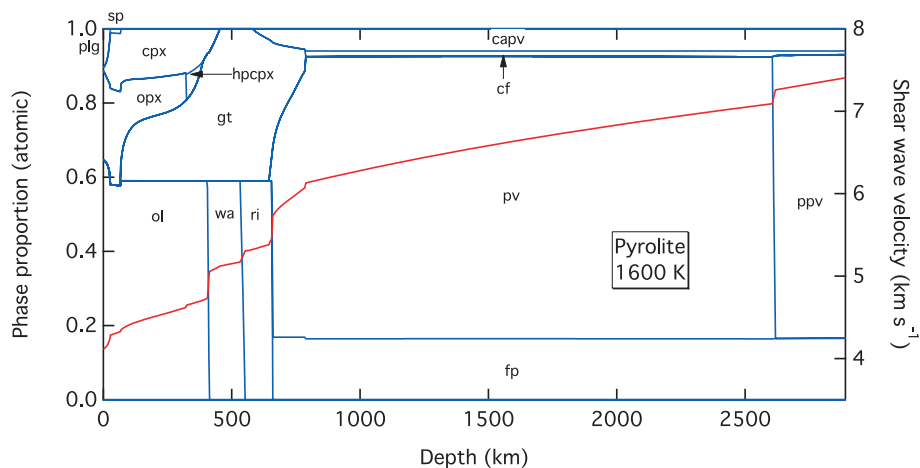


**Figure 17.** Phase proportions (as atomic fraction, blue lines, left-hand axis) and shear wave velocity (red line, right-hand axis) for pyrolite along the 1600 K isentrope, computed with our method.

processes, such as the manufacture of steels and propellants, or the genesis of igneous and metamorphic rocks (Smith & Missen 1982). It is only over the past few decades that developments in high pressure technology have produced most of what we know of phase equilibria in the subcrustal Earth. Recent breakthroughs show that phase transitions extend throughout the mantle including at the core–mantle boundary. It is the challenges posed by the thermodynamic description of multiphase assemblages at extreme pressure–temperature conditions, and the need to make contact with geophysical observations, and dynamical models of Earth's evolution, that have motivated us to develop our thermodynamic method. Our approach emphasizes simple functional forms that have wide applicability in  $P$ – $T$  space, yet require the minimum possible number of free parameters, permitting compact description of material behaviour in a regime in which there remain important gaps in our knowledge. Indeed, within the framework of our model, values of many parameters, especially of high pressure phases, must be regarded as provisional, and we anticipate that future developments in experiment and theory will motivate redeterminations.

This paper completes the description and specification of our method begun in Paper I. We have shown that the method is capable of capturing physical behaviour over the entire mantle pressure–temperature regime. To our knowledge, our method is unique in encompassing phase equilibria and physical properties of multiphase assemblages including the full elastic constant tensor. Looking forward to future developments of the model itself, these are likely to include the addition of more components, phases and species, and the description of important physics such as the spin-pairing transition.

## ACKNOWLEDGMENTS

We thank J. A. D. Connolly and an anonymous reviewer for their comments which have improved the manuscript, and the former for checking our phase diagrams; responsibility for any remaining errors rests solely with the authors. This work was partly supported by the CSEDI program of the National Science Foundation under grant EAR-0079980.

## REFERENCES

- Akaogi, M. & Akimoto, S., 1977. Pyroxene-garnet solid-solution equilibria in systems  $\text{Mg}_4\text{Si}_4\text{O}_{12}$ – $\text{Mg}_3\text{Al}_2\text{Si}_3\text{O}_{12}$  and  $\text{Fe}_4\text{Si}_4\text{O}_{12}$ – $\text{Fe}_3\text{Al}_2\text{Si}_3\text{O}_{12}$  at high-pressures and temperatures, *Phys. Earth planet. Inter.*, **15**(1), 90–106.
- Akaogi, M. & Akimoto, S., 1979. High-pressure phase-equilibria in a garnet lherzolite, with special reference to  $\text{Mg}^{2+}$ – $\text{Fe}^{2+}$  partitioning among constituent minerals, *Phys. Earth planet. Inter.*, **19**(1), 31–51.
- Akaogi, M., Yusa, H., Shiraishi, K. & Suzuki, T., 1995. Thermodynamic properties of alpha-quartz, coesite, and stishovite and equilibrium phase-relations at high-pressures and high-temperatures, *J. geophys. Res.*, **100**(B11), 22 337–22 347.
- Akaogi, M., Hamada, Y., Suzuki, T., Kobayashi, M. & Okada, M., 1999. High pressure transitions in the system  $\text{MgAl}_2\text{O}_4$ – $\text{CaAl}_2\text{O}_4$ : a new hexagonal aluminous phase with implication for the lower mantle, *Phys. Earth planet. Inter.*, **115**(1), 67–77.
- Akaogi, M., Yano, M., Tejima, Y., Iijima, M. & Kojitani, H., 2004. High-pressure transitions of diopside and wollastonite: phase equilibria and thermochemistry of  $\text{CaMgSi}_2\text{O}_6$ ,  $\text{CaSiO}_3$  and  $\text{CaSi}_2\text{O}_5$ – $\text{CaTiSiO}_5$  system, *Phys. Earth planet. Inter.*, **143–44**, 145–156.
- Akimoto, S. & Syono, Y., 1970. High-pressure decomposition of the system  $\text{FeSiO}_3$ – $\text{MgSiO}_3$ , *Phys. Earth planet. Inter.*, **3**, 186–188.
- Alberty, R.A., 2001. Use of legendre transforms in chemical thermodynamics—(IUPAC technical report), *Pure appl. Chem.*, **73**(8), 1349–1380.
- Ammann, M.W., Brodholt, J.P., Wookey, J. & Dobson, D.P., 2010. First-principles constraints on diffusion in lower-mantle minerals and a weak D'' layer, *Nature*, **465**(7297), 462–465.
- Anderson, D.L., 1987. Thermally induced phase-changes, lateral heterogeneity of the mantle, continental roots, and deep slab anomalies, *J. geophys. Res.*, **92**(B13), 13968–13980.
- Anderson, O.L., 1995. *Equations of State of Solids for Geophysics and Ceramic Science*, Oxford University Press, Oxford.
- Anderson, O.L. & Isaak, D.G., 1995. Elastic constants of mantle minerals at high temperature, in *Mineral Physics and Crystallography: A Handbook of Physical Constants*, pp. 64–97, ed. Ahrens, T.J., American Geophysical Union, Washington, DC.
- Anderson, O.L., Isaak, D.G. & Yamamoto, S., 1989. Anharmonicity and the equation of state for gold, *J. appl. Phys.*, **65**(4), 1534–1543.
- Andrault, D., Fiquet, G. & Hanfland, M., 1998. Pressure-induced landau-type transition in stishovite, *Science*, **282**, 720–723.
- Angel, R.J., Hazen, R.M., McCormick, T.C., Prewitt, C.T. & Smyth, J.R., 1988. Comparative compressibility of end-member feldspars, *Phys. Chem. Miner.*, **15**(4), 313–318.
- Aranovich, L.Y. & Newton, R.C., 1999. Experimental determination of  $\text{CO}_2$ – $\text{H}_2\text{O}$  activity-composition relations at 600–1000 degrees C and 6–14 kbar by reversed decarbonation and dehydration reactions, *Am. Mineral.*, **84**(9), 1319–1332.
- Asimow, P.D. & Ghiorso, M.S., 1998. Algorithmic modifications extending MELTS to calculate subsolidus phase relations, *Am. Miner.*, **83**(9–10), 1127–1132.
- Auzende, A.L., Badro, J., Ryerson, F.J., Weber, P.K., Fallon, S.J., Addad, A., Siebert, J. & Fiquet, G., 2008. Element partitioning between magnesium silicate perovskite and ferropericlae: new insights into bulk lower-mantle geochemistry, *Earth planet. Sci. Lett.*, **269**(1–2), 164–174.
- Badro, J., Fiquet, G., Guyot, F., Rueff, J.P., Struzhkin, V.V., Vanko, G. & Monaco, G., 2003. Iron partitioning in earth's mantle: toward a deep lower mantle discontinuity, *Science*, **300**(5620), 789–791.
- Badro, J., Rueff, J.P., Vanko, G., Monaco, G., Fiquet, G. & Guyot, F., 2004. Electronic transitions in perovskite: possible nonconvecting layers in the lower mantle, *Science*, **305**(5682), 383–386.
- Barron, T.H.K., Berg, W.T. & Morrison, J.A., 1957. The thermal properties of alkali halide crystals. 2: analysis of experimental results, *Proc. R. Soc. Lond., A-Math. Phys. Sci.*, **242**(1231), 478–492.
- Bass, J.D., 1995. Elasticity of minerals, glasses, and melts, in *Mineral Physics and Crystallography: A Handbook of Physical Constants*, pp. 45–63, ed. Ahrens, T.J., AGU, Washington, DC.
- Bass, J.D. & Anderson, D.L., 1984. Composition of the upper mantle—geophysical tests of 2 petrological models, *Geophys. Res. Lett.*, **11**, 237–240.
- Bengtson, A., Li, J. & Morgan, D., 2005. Mössbauer modeling to interpret the spin state of iron in  $(\text{Mg}, \text{Fe})\text{SiO}_3$  perovskite, *Am. Mineral.*, **90**, 199–205.
- Benisek, A., Kroll, H., Cemic, L., Kohl, V., Breit, U. & Heying, B., 2003. Enthalpies in (Na, Ca)- and (K, Ca)-feldspar binaries: a high-temperature solution calorimetric study, *Contr. Mineral. Petrol.*, **145**(1), 119–129.
- Benisek, A., Etzel, K. & Cemic, L., 2007. Thermodynamic mixing behavior of synthetic Ca-Tschermak-diopside pyroxene solid solutions: II. Heat of mixing and activity-composition relationships, *Phys. Chem. Miner.*, **34**(10), 747–755.
- Berman, R.G., 1988. Internally-consistent thermodynamic data for minerals in the system  $\text{Na}_2\text{O}$ – $\text{K}_2\text{O}$ – $\text{CaO}$ – $\text{MgO}$ – $\text{FeO}$ – $\text{Fe}_2\text{O}_3$ – $\text{Al}_2\text{O}_3$ – $\text{SiO}_2$ – $\text{TiO}_2$ – $\text{H}_2\text{O}$ – $\text{CO}_2$ , *J. Petrol.*, **29**(2), 445–522.
- Bina, C.R., 1998. Free energy minimization by simulated annealing with applications to lithospheric slabs and mantle plumes, *Pure appl. Geophys.*, **151**(2–4), 605–618.
- Bina, C.R. & Kumazawa, M., 1993. Thermodynamic coupling of phase and chemical-boundaries in planetary interiors, *Phys. Earth planet. Inter.*, **76**(3–4), 329–341.
- Birch, F., 1947. Finite elastic strain of cubic crystals, *Phys. Rev.*, **71**, 809–824.

- Birch, F., 1978. Finite strain isotherm and velocities for single-crystal and polycrystalline NaCl at high-pressure and 300°K, *J. geophys. Res.*, **83**, 1257–1268.
- Boehler, R., 1982. Adiabats of quartz, coesite, olivine, and magnesium-oxide to 50 kbar and 1000 K, and the adiabatic gradient in the Earth's mantle, *J. geophys. Res.*, **87**(Nb7), 5501–5506.
- Bohlen, S.R., Essene, E.J. & Boettcher, A.L., 1980. Reinvestigation and application of olivine-quartz-orthopyroxene barometry, *Earth planet. Sci. Lett.*, **47**(1), 1–10.
- Born, M., 1939. Thermodynamics of crystals and melting, *J. Chem. Phys.*, **7**, 591–603.
- Born, M. & Huang, K., 1954. *Dynamical Theory of Crystal Lattices*, Clarendon Press, Oxford.
- Bosenick, A., Geiger, C.A. & Cemic, L., 1996. Heat capacity measurements of synthetic pyrope-grossular garnets between 320 and 1000 K by differential scanning calorimetry, *Geochim. Cosmochim. Acta*, **60**(17), 3215–3227.
- Bouhifd, M.A., Andrault, D., Fiquet, G. & Richet, P., 1996. Thermal expansion of forsterite up to the melting point, *Geophys. Res. Lett.*, **23**(10), 1143–1146.
- Boyd, F.R. & England, J.L., 1963. Effect of pressure on melting of diopside,  $\text{CaMgSi}_2\text{O}_6$ , and albite,  $\text{NaAlSi}_3\text{O}_8$ , in range up to 50 kilobars, *J. geophys. Res.*, **68**(1), 311–323.
- Boyd, F.R., England, J.L. & Davis, B.T.C., 1964. Effects of pressure on the melting and polymorphism of enstatite,  $\text{MgSiO}_3$ , *J. geophys. Res.*, **69**(10), 2101–2106.
- Brey, G.P., Doroshev, A.M., Gurnis, A.V. & Turkin, A.I., 1999. Garnet-spinel-olivine-orthopyroxene equilibria in the  $\text{FeO-MgO-Al}_2\text{O}_3\text{-SiO}_2\text{-Cr}_2\text{O}_3$  system: I. Composition and molar volumes of minerals, *Eur. J. Mineral.*, **11**(4), 599–617.
- Brosh, E., Shneck, R.Z. & Makov, G., 2008. Explicit Gibbs free energy equation of state for solids, *J. Phys. Chem. Solids*, **69**, 1912–1922.
- Brown, J.M., Abramson, E.H. & Angel, R.J., 2006. Triclinic elastic constants for low albite, *Phys. Chem. Miner.*, **33**(4), 256–265.
- Callen, H.B., 1960. *Thermodynamics*, John Wiley and Sons, New York.
- Cammarano, F., Goes, S., Vacher, P. & Giardini, D., 2003. Inferring upper-mantle temperatures from seismic velocities, *Phys. Earth planet. Inter.*, **138**(3–4), 197–222.
- Cammarano, F., Romanowicz, B., Stixrude, L., Lithgow-Bertelloni, C. & Xu, W.B., 2009. Inferring the thermochemical structure of the upper mantle from seismic data, *Geophys. J. Int.*, **179**(2), 1169–1185.
- Canil, D., 1994. Stability of clinopyroxene at pressure–temperature conditions of the transition region, *Phys. Earth planet. Inter.*, **86**, 25–34.
- Canup, R.M., 2004. Dynamics of lunar formation, *Ann. Rev. Astron. Astrophys.*, **42**, 441–475.
- Caracas, R. & Cohen, R.E., 2005. Effect of chemistry on the stability and elasticity of the perovskite and post-perovskite phases in the  $\text{MgSiO}_3\text{-FeSiO}_3\text{-Al}_2\text{O}_3$  system and implications for the lowermost mantle, *Geophys. Res. Lett.*, **32**, L16310, doi:10.1029/2005GL023164.
- Carlson, W.D. & Lindsley, D.H., 1988. Thermochemistry of pyroxenes on the join  $\text{Mg}_2\text{Si}_2\text{O}_6\text{-CaMgSi}_2\text{O}_6$ , *Am. Mineral.*, **73**(3–4), 242–252.
- Carpenter, M.A., Salje, E.K.H., Graeme-Barber, A., Wruck, B., Dove, M.T. & Knight, K.S., 1998. Calibration of excess thermodynamic properties and elastic constant variations associated with the  $\alpha \leftrightarrow \beta$  phase transition in quartz, *Am. Mineral.*, **83**, 2–22.
- Carpenter, M.A., Hemley, R.J. & Mao, H.K., 2000. High-pressure elasticity of stishovite and the  $\text{P}_4(2)/\text{mmn} \leftrightarrow \text{pnmm}$  phase transition, *J. geophys. Res.*, **105**(B5), 10807–10816.
- Chaplot, S.L., Choudhury, N., Ghose, S., Rao, M.N., Mittal, R. & Goel, P., 2002. Inelastic neutron scattering and lattice dynamics of minerals, *Eur. J. Mineral.*, **14**(2), 291–329.
- Chatterjee, N.D., Kruger, R., Haller, G. & Olbricht, W., 1998. The Bayesian approach to an internally consistent thermodynamic database: theory, database, and generation of phase diagrams, *Contrib. Mineral. Petrol.*, **133**, 149–168.
- Christensen, U., 1995. Effects of phase transitions on mantle convection, *Ann. Rev. Earth planet. Sci.*, **23**, 65–87.
- Cobden, L., Goes, S., Cammarano, F. & Connolly, J.A.D., 2008. Thermochemical interpretation of one-dimensional seismic reference models for the upper mantle: evidence for bias due to heterogeneity, *Geophys. J. Int.*, **175**(2), 627–648.
- Cobden, L., Goes, S., Ravenna, M., Styles, E., Cammarano, F., Gallagher, K. & Connolly, J.A.D., 2009. Thermochemical interpretation of 1-D seismic data for the lower mantle: the significance of nonadiabatic thermal gradients and compositional heterogeneity, *J. geophys. Res.*, **114**, B11309, doi:10.1029/2008JB006262.
- Cohen, R.E., 1986. Thermodynamic solution properties of aluminous clinopyroxenes: non-linear least squares refinements, *Geochim. Cosmochim. Acta*, **50**, 563–575.
- Cohen, R.E. & Gong, Z., 1994. Melting and melt structure of MgO at high pressures, *Phys. Rev. B*, **50**, 12 301–12 311.
- Comodi, P., Zanazzi, P.F., Poli, S. & Schmidt, M.W., 1997. High-pressure behavior of kyanite: compressibility and structural deformations, *Am. Mineral.*, **82**(5–6), 452–459.
- Connolly, J.A.D., 1990. Multivariable phase-diagrams - an algorithm based on generalized thermodynamics, *Am. J. Sci.*, **290**(6), 666–718.
- Connolly, J.A.D., 2005. Computation of phase equilibria by linear programming: a tool for geodynamic modeling and its application to subduction zone decarbonation, *Earth planet. Sci. Lett.*, **236**(1–2), 524–541.
- Connolly, J.A.D., 2009. The geodynamic equation of state: what and how, *Geochim. Geophys. Geosyst.*, **10**, Q10014, doi:10.1029/2009GC002540.
- Connolly, J.A.D. & Kerrick, D.M., 1987. An algorithm and computer-program for calculating composition phase-diagrams, *Calphad-Comput. Coupl. Phase Diag. Thermochem.*, **11**(1), 1–55.
- Danckwerth, P.A. & Newton, R.C., 1978. Experimental determination of the spinel peridotite to garnet peridotite reaction in the system  $\text{MgO-Al}_2\text{O}_3\text{-SiO}_2$  in the range 900°–1100°C and  $\text{Al}_2\text{O}_3$  isopleths of enstatite in the spinel field, *Contrib. Mineral. Petrol.*, **66**(2), 189–201.
- Dasilva, C.R.S., Karki, B.B., Stixrude, L. & Wentzcovitch, R.M., 1999. Ab initio study of the elastic behavior of  $\text{MgSiO}_3$  ilmenite at high pressure, *Geophys. Res. Lett.*, **26**(7), 943–946.
- Davies, G.F., 1974. Effective elastic-moduli under hydrostatic stress. 1: quasi-harmonic theory, *J. Phys. Chem. Solids*, **35**(11), 1513–1520.
- Davies, P.K. & Navrotsky, A., 1983. Quantitative correlations of deviations from ideality in binary and pseudobinary solid-solutions, *J. Solid State Chem.*, **46**(1), 1–22.
- Dorogokupets, P.I., 1995. Equation of state for lambda-transition in quartz, *J. geophys. Res.*, **100**(B5), 8489–8499.
- Duan, W.H., Karki, B.B. & Wentzcovitch, R.M., 1999. High-pressure elasticity of alumina studied by first principles, *Am. Mineral.*, **84**(11–12), 1961–1966.
- Duffy, T.S. & Anderson, D.L., 1989. Seismic velocities in mantle minerals and the mineralogy of the upper mantle, *J. geophys. Res.*, **94**(B2), 1895–1912.
- Dziewonski, A.M. & Anderson, D.L., 1981. Preliminary reference Earth model, *Phys. Earth planet. Inter.*, **25**, 297–356.
- Eriksson, G., 1971. Thermodynamics studies of high temperature equilibria 3: SOLGAS, a computer program for calculating composition and heat condition of an equilibrium mixture, *Acta Chem. Scand.*, **25**(7), 2651–2658.
- Etzel, K., Benisek, A., Dachs, E. & Cemic, L., 2007. Thermodynamic mixing behavior of synthetic Ca-Tschermak-diopside pyroxene solid solutions: I. Volume and heat capacity of mixing, *Phys. Chem. Miner.*, **34**(10), 733–746.
- Fabrichnaya, O.B., 1999. The phase relations in the  $\text{FeO-MgO-Al}_2\text{O}_3\text{-SiO}_2$  system: assessment of thermodynamic properties and phase equilibria at pressures up to 30 GPa, *Calphad-Comput. Coupl. Phase Diag. Thermochem.*, **23**(1), 19–67.
- Fei, Y., 1995. Thermal expansion, in *Mineral Physics and Crystallography: A Handbook of Physical Constants*, pp. 29–44, ed. Ahrens, T.J., AGU, Washington, DC.
- Fei, Y., Mao, H.K. & Mysen, B.O., 1991. Experimental-determination of element partitioning and calculation of phase-relations in the  $\text{MgO-FeO-SiO}_2$  system at high-pressure and high-temperature, *J. geophys. Res.*, **96**(B2), 2157–2169.

- Fei, Y. *et al.*, 2004. Experimentally determined postspinel transformation boundary in  $\text{Mg}_2\text{SiO}_4$  using MgO as an internal pressure standard and its geophysical implications, *J. geophys. Res.*, **109**(B2), B02305, doi:10.1029/2003JB002562.
- Fei, Y.W., Saxena, S.K. & Navrotsky, A., 1990. Internally consistent thermodynamic data and equilibrium phase-relations for compounds in the system  $\text{MgO-SiO}_2$  at high-pressure and high-temperature, *J. geophys. Res.*, **95**(B5), 6915–6928.
- Fei, Y.W., Mao, H.K., Shu, J.F., Parthasarathy, G., Bassett, W.A. & Ko, J.D., 1992. Simultaneous high-P, high-T X-ray diffraction study of  $\beta$ - $(\text{Mg}, \text{Fe})_2\text{SiO}_4$  to 26 GPa and 900 K, *J. geophys. Res.*, **97**(B4), 4489–4495.
- Fei, Y.W. *et al.*, 2004. A critical evaluation of pressure scales at high temperatures by in situ X-ray diffraction measurements, *Phys. Earth planet. Inter.*, **143–44**, 515–526.
- Fiquet, G., Richet, P. & Montagnac, G., 1999. High-temperature thermal expansion of lime, periclase, corundum and spinel, *Phys. Chem. Miner.*, **27**(2), 103–111.
- Fiquet, G., Dewaele, A., Andrault, D., Kunz, M. & Bihan, T.L., 2000. Thermoelastic properties and crystal structure of  $\text{MgSiO}_3$  perovskite at lower mantle pressure and temperature conditions, *Geophys. Res. Lett.*, **27**, 21–24.
- Flesch, L.M., Li, B.S. & Liebermann, R.C., 1998. Sound velocities of polycrystalline  $\text{MgSiO}_3$ -orthopyroxene to 10 GPa at room temperature, *Am. Mineral.*, **83**(5–6), 444–450.
- Frost, D.J., 2003a.  $\text{Fe}^{2+}$ -Mg partitioning between garnet, magnesio-wustite, and  $(\text{Mg}, \text{Fe})_2\text{SiO}_4$  phases of the transition zone, *Am. Mineral.*, **88**(2–3), 387–397.
- Frost, D.J., 2003b. The structure and sharpness of  $(\text{Mg}, \text{Fe})_2\text{SiO}_4$  phase transformations in the transition zone, *Earth planet. Sci. Lett.*, **216**(3), 313–328.
- Frost, D.J., Langenhorst, F. & van Aken, P.A., 2001. Fe-Mg partitioning between ringwoodite and magnesio-wustite and the effect of pressure, temperature and oxygen fugacity, *Phys. Chem. Miner.*, **28**(7), 455–470.
- Funamori, N. *et al.*, 1998. High-pressure transformations in  $\text{MgAl}_2\text{O}_4$ , *J. geophys. Res.*, **103**(B9), 20 813–20 818.
- Ganguly, J., 2001. Thermodynamic modeling of solid solutions, in *Solid Solutions in Silicate and Oxide Systems*, pp. 37–70, ed. Geiger, C.A., European Mineralogical Union Notes in Mineralogy, Etv's University Press, Budapest.
- Ganguly, J. & Ghose, S., 1979. Aluminous orthopyroxene: order-disorder, thermodynamic properties, and petrologic implications, *Contrib. Mineral. Petrol.*, **69**, 375–385.
- Ganguly, J., Freed, A.M. & Saxena, S.K., 2009. Density profiles of oceanic slabs and surrounding mantle: integrated thermodynamic and thermal modeling, and implications for the fate of slabs at the 660 km discontinuity, *Phys. Earth planet. Inter.*, **172**(3–4), 257–267.
- Gasparik, T., 1984a. Experimentally determined stability of clinopyroxene + garnet + corundum in the system  $\text{CaO-MgO-Al}_2\text{O}_3\text{-SiO}_2$ , *Am. Mineral.*, **69**(11–1), 1025–1035.
- Gasparik, T., 1984. 2-pyroxene thermobarometry with new experimental data in the system  $\text{CaO-MgO-Al}_2\text{O}_3\text{-SiO}_2$ , *Contrib. Mineral. Petrol.*, **87**(1), 87–97.
- Gasparik, T., 1985. Experimental study of subsolidus phase relations and mixing properties of pyroxene and plagioclase in the system  $\text{Na}_2\text{O-CaO-Al}_2\text{O}_3\text{-SiO}_2$ , *Contrib. Mineral. Petrol.*, **89**(4), 346–357.
- Gasparik, T., 1989. Transformation of enstatite – diopside – jadeite pyroxenes to garnet, *Contrib. Mineral. Petrol.*, **102**(4), 389–405.
- Gasparik, T., 1990a. Phase-relations in the transition zone, *J. geophys. Res.*, **95**(B10), 15 751–15 769.
- Gasparik, T., 1990b. A thermodynamic model for the enstatite-diopside join, *Am. Mineral.*, **75**(9–10), 1080–1091.
- Gasparik, T., 1992. Enstatite-jadeite join and its role in the Earth's mantle, *Contrib. Mineral. Petrol.*, **111**(3), 283–298.
- Gasparik, T., 1996. Melting experiments on the enstatite-diopside join at 70–224 kbar, including the melting of diopside, *Contrib. Mineral. Petrol.*, **124**(2), 139–153.
- Gasparik, T. & Newton, R.C., 1984. The reversed alumina contents of orthopyroxene in equilibrium with spinel and forsterite in the system  $\text{MgO-Al}_2\text{O}_3\text{-SiO}_2$ , *Contrib. Mineral. Petrol.*, **85**(2), 186–196.
- Gatta, G.D., Nestola, F. & Walter, J.M., 2006. On the thermo-elastic behaviour of kyanite: a neutron powder diffraction study up to 1200° C, *Mineral. Mag.*, **70**(3), 309–317.
- Geiger, C.A., 1999. Thermodynamics of  $(\text{Fe}^{2+}, \text{Mn}^{2+}, \text{Mg}, \text{Ca})_3\text{-Al}_2\text{Si}_3\text{O}_{12}$  garnet: a review and analysis, *Mineral. Petrol.*, **66**(4), 271–299.
- Gerya, T.V., Podlesskii, K.K., Perchuk, L.L. & Maresch, W.V., 2004. Semi-empirical Gibbs free energy formulations for minerals and fluids for use in thermodynamic databases of petrological interest, *Phys. Chem. Miner.*, **31**, 429–455.
- Ghiorso, M.S., 1994. Algorithms for the estimation of phase-stability in heterogeneous thermodynamic systems, *Geochim. Cosmochim. Acta*, **58**(24), 5489–5501.
- Ghiorso, M.S. & Sack, R.O., 1995. Chemical mass-transfer in magmatic processes. 4: a revised and internally consistent thermodynamic model for the interpolation and extrapolation of liquid-solid equilibria in magmatic systems at elevated-temperatures and pressures, *Contrib. Mineral. Petrol.*, **119**(2–3), 197–212.
- Ghiorso, M.S., Hirschmann, M.M., Reiners, P.W. & Kress, V.C., 2002. The pmelts: a revision of MELTS for improved calculation of phase relations and major element partitioning related to partial melting of the mantle to 3 GPa, *Geochim. Geophys. Geosyst.*, **3**, doi:10.1029/2001GC000217.
- Gieske, J.H. & Barsch, G.R., 1968. Pressure dependence of elastic constants of single crystalline aluminum oxide, *Phys. Status Solidi*, **29**(1), 121–131.
- Goldsmith, J.R., 1980. The melting and breakdown reactions of anorthite at high-pressures and temperatures, *Am. Mineral.*, **65**(3–4), 272–284.
- Gottschalk, M., 1997. Internally consistent thermodynamic data for rock-forming minerals in the system  $\text{SiO}_2\text{-TiO}_2\text{-Al}_2\text{O}_3\text{-Fe}_2\text{O}_3\text{-CaO-MgO-FeO-K}_2\text{O-Na}_2\text{O-H}_2\text{O-CO}_2$ , *Eur. J. Mineral.*, **9**, 175–223.
- Grover, J., 1972. The stability of low-clinoenstatite in the system  $\text{Mg}_2\text{Si}_2\text{O}_6\text{-CaMgSi}_2\text{O}_6$  (abstract), *EOS, Trans. Am. geophys. Un.*, **53**, 539.
- Grüneisen, E., 1912. Theorie des festen zustandes einatomiger elemente, *Annalen der Physik*, **39**, 257–306.
- Guignot, N., Andrault, D., Morard, G., Bolfan-Casanova, N. & Mezouar, M., 2007. Thermoelastic properties of post-perovskite phase  $\text{MgSiO}_3$  determined experimentally at core-mantle boundary P-T conditions, *Earth planet. Sci. Lett.*, **256**(1–2), 162–168.
- Haar, L., Gallagher, J.S. & Kell, G.S., 1984. *NBS/NRC Steam Tables: Thermodynamic and Transport Properties and Computer Programs for Vapor and Liquid States of Water in SI Units*, Hemisphere, Washington.
- Hacker, B.R., Abers, G.A. & Peacock, S.M., 2003. Subduction factory—I. Theoretical mineralogy, densities, seismic wave speeds, and  $\text{H}_2\text{O}$  contents, *J. geophys. Res.*, **108**(B1), 2029, doi:10.1029/2001JB001127.
- Hackler, R.T. & Wood, B.J., 1989. Experimental-determination of Fe and Mg exchange between garnet and olivine and estimation of Fe-Mg mixing properties in garnet, *Am. Mineral.*, **74**(9–10), 994–999.
- Hama, J. & Suito, K., 2001. Thermoelastic models of minerals and the composition of the Earth's lower mantle, *Phys. Earth planet. Inter.*, **125**(1–4), 147–166.
- Harlov, D.E. & Milke, R., 2002. Stability of corundum plus quartz relative to kyanite and sillimanite at high temperature and pressure, *Am. Mineral.*, **87**(4), 424–432.
- Harrison, R.J., Redfern, S.A.T. & O'Neill, H.S.C., 1998. The temperature dependence of the cation distribution in synthetic hercynite ( $\text{FeAl}_2\text{O}_4$ ) from in-situ neutron structure refinements, *Am. Mineral.*, **83**(9–10), 1092–1099.
- Harvie, C.E., Greenberg, J.P. & Weare, J.H., 1987. A chemical-equilibrium algorithm for highly nonideal multiphase systems—free-energy minimization, *Geochim. Cosmochim. Acta*, **51**(5), 1045–1057.
- Haselton, H.T. & Newton, R.C., 1980. Thermodynamics of pyrope-grossular garnets and their stabilities at high-temperatures and high-pressures, *J. geophys. Res.*, **85**(NB12), 6973–6982.
- Haselton, H.T. & Westrum, E.F., 1980. Low-temperature heat-capacities of synthetic pyrope, grossular, and pyrope60grossular40, *Geochim. Cosmochim. Acta*, **44**(5), 701–709.

- Haselton, H.T., Hemingway, B.S. & Robie, R.A., 1984. Low-temperature heat-capacities of  $\text{CaAl}_2\text{SiO}_6$  glass and pyroxene and thermal-expansion of  $\text{CaAl}_2\text{SiO}_6$  pyroxene, *Am. Mineral.*, **69**(5-6), 481–489.
- Hazen, R.M., Downs, R.T., Finger, L.W., Conrad, P.G. & Gasparik, T., 1994. Crystal-chemistry of Ca-bearing majorite, *Am. Mineral.*, **79**(5-6), 581–584.
- Hazen, R.M., Weinberger, M.B., Yang, H.X. & Prewitt, C.T., 2000. Comparative high-pressure crystal chemistry of wadsleyite,  $\beta\text{-(Mg}_{1-x}\text{Fe}_x)_2\text{SiO}_4$ , with  $x = 0$  and  $0.25$ , *Am. Mineral.*, **85**(5-6), 770–777.
- Heinemann, R., Kroll, H., Kirfel, A. & Barbier, B., 2007. Order and anti-order in olivine: III. Variation of the cation distribution in the Fe, Mg olivine solid solution series with temperature and composition, *Eur. J. Mineral.*, **19**(1), 15–27.
- Helgeson, H.C., Delany, J.M., Nesbitt, H.W. & Bird, D.K., 1978. Summary and critique of the thermodynamic properties of rock-forming minerals, *Am. J. Sci.*, **278**, 1–229.
- Hemingway, B.S., Robie, R.A., Evans, H.T. & Kerrick, D.M., 1991. Heat-capacities and entropies of sillimanite, fibrolite, andalusite, kyanite, and quartz and the  $\text{Al}_2\text{SiO}_5$  phase-diagram, *Amer. Mineral.*, **76**(9-10), 1597–1613.
- Hemingway, B.S., Bohlen, S.R., Hankins, W.B., Westrum, E.F. & Kuskov, O.L., 1998. Heat capacity and thermodynamic properties for coesite and jadeite, reexamination of the quartz-coesite equilibrium boundary, *Am. Mineral.*, **83**(5-6), 409–418.
- Higo, Y., Inoue, T., Irifune, T., Funakoshi, K.I. & Li, B.S., 2008. Elastic wave velocities of  $(\text{Mg}_{0.91}\text{Fe}_{0.09})_2\text{SiO}_4$  ringwoodite under P-T conditions of the mantle transition region, *Phys. Earth planet. Inter.*, **166**(3-4), 167–174.
- Hillert, M. & Staffansson, L.I., 1970. Regular solution model for stoichiometric phases and ionic melts, *Acta Chem. Scand.*, **24**(10), 3618–3626.
- Hirose, K., 2002. Phase transitions in pyrolitic mantle around 670-km depth: implications for upwelling of plumes from the lower mantle, *J. geophys. Res.*, **107**(B4), 2078, doi:10.1029/2001JB000597.
- Hirose, K., Fei, Y.W., Ono, S., Yagi, T. & Funakoshi, K., 2001a. In situ measurements of the phase transition boundary in  $\text{Mg}_3\text{Al}_2\text{Si}_3\text{O}_{12}$ : implications for the nature of the seismic discontinuities in the Earth's mantle, *Earth planet. Sci. Lett.*, **184**(3-4), 567–573.
- Hirose, K., Komabayashi, T., Murakami, M. & Funakoshi, K., 2001b. In situ measurements of the majorite-akimotoite-perovskite phase transition boundaries in  $\text{MgSiO}_3$ , *Geophys. Res. Lett.*, **28**(23), 4351–4354.
- Hirose, K., Takafuji, N., Sata, N. & Ohishi, Y., 2005. Phase transition and density of subducted MORB crust in the lower mantle, *Earth planet. Sci. Lett.*, **237**(1-2), 239–251.
- Hirose, K., Sinmyo, R., Sata, N. & Ohishi, Y., 2006. Determination of post-perovskite phase transition boundary in  $\text{MgSiO}_3$  using Au and MgO pressure standards, *Geophys. Res. Lett.*, **33**(1), L01310.
- Hirose, K., Takafuji, N., Fujino, K., Shieh, S.R. & Duffy, T.S., 2008. Iron partitioning between perovskite and post-perovskite: a transmission electron microscope study, *Am. Mineral.*, **93**(10), 1678–1681.
- Holland, T.J.B., 1980. Reaction albite = jadeite + quartz determined experimentally in the range 600–1200°C, *Am. Mineral.*, **65**(1-2), 129–134.
- Holland, T.J.B., 1983. The experimental determination of activities in disordered and short-range ordered jadeitic pyroxenes, *Contrib. Mineral. Petrol.*, **82**(2-3), 214–220.
- Holland, T.J.B., 1989. Dependence of entropy on volume for silicate and oxide minerals - a review and a predictive model, *Am. Mineral.*, **74**(1-2), 5–13.
- Holland, T.J.B. & Powell, R., 1990. An enlarged and updated internally consistent thermodynamic dataset with uncertainties and correlations—the system  $\text{K}_2\text{O}-\text{Na}_2\text{O}-\text{CaO}-\text{MgO}-\text{MnO}-\text{FeO}-\text{Fe}_2\text{O}_3-\text{Al}_2\text{O}_3-\text{TiO}_2-\text{SiO}_2-\text{C}-\text{H}_2-\text{O}_2$ , *J. Metamor. Geol.*, **8**(1), 89–124.
- Holland, T.J.B. & Powell, R., 1998. An internally consistent thermodynamic data set for phases of petrological interest, *J. Metamor. Geol.*, **16**(3), 309–343.
- Holland, T. & Powell, R., 2003. Activity-composition relations for phases in petrological calculations: an asymmetric multicomponent formulation, *Contrib. Mineral. Petrol.*, **145**(4), 492–501.
- Holland, T.J.B. & Powell, R., 2006. Mineral activity-composition relations and petrological calculations involving cation equipartition in multisite minerals: a logical inconsistency, *J. Metamor. Geol.*, **24**, 851–861.
- Holland, T.J.B., Navrotsky, A. & Newton, R.C., 1979. Thermodynamic parameters of  $\text{CaMgSi}_2\text{O}_6$ - $\text{Mg}_2\text{Si}_2\text{O}_6$  pyroxenes based on regular solution and cooperative disordering models, *Contrib. Mineral. Petrol.*, **69**(4), 337–344.
- Holm, J.L., Kleppa, O.J. & Westrum, E.F., 1967. Thermodynamics of polymorphic transformations in silica. Thermal properties from 5 to 1070°K and pressure-temperature stability fields for coesite and stishovite, *Geochim. Cosmochim. Acta*, **31**(12), 2289–2307.
- Hovis, G.L., Crelling, J., Watters, D., Dreibeis, B., Dennison, A., Keohane, M. & Brennan, S., 2003. Thermal expansion of nepheline-kalsilite crystalline solutions, *Mineral. Mag.*, **67**, 535–546.
- Hovis, G.L., Mott, A. & Roux, J., 2009. Thermodynamic, phase equilibrium, and crystal chemical behavior in the nepheline-kalsilite system, *Am. J. Sci.*, **309**, 397–419.
- HughJones, D., 1997. Thermal expansion of  $\text{MgSiO}_3$  and  $\text{FeSiO}_3$  ortho- and clinopyroxenes, *Am. Mineral.*, **82**(7-8), 689–696.
- HughJones, D., Sharp, T., Angel, R. & Woodland, A., 1996. The transition of orthoferrosilite to high-pressure  $\text{C}_2/\text{C}$  clinoferrosilite at ambient temperature, *Eur. J. Mineral.*, **8**(6), 1337–1345.
- HughJones, D.A. & Angel, R.J., 1997. Effect of  $\text{Ca}^{2+}$  and  $\text{Fe}^{2+}$  on the equation of state of  $\text{MgSiO}_3$  orthopyroxene, *J. geophys. Res.*, **102**(B6), 12333–12340.
- Hunt, S.A., Dobson, D.P., Li, L., Weidner, D.J. & Brodholt, J.P., 2010. Relative strength of the pyrope-majorite solid solution and the flow-law of majorite containing garnets, *Phys. Earth planet. Inter.*, **179**(1-2), 87–95.
- Irifune, T., 1987. An experimental investigation of the pyroxene garnet transformation in a pyrolite composition and its bearing on the constitution of the mantle, *Phys. Earth planet. Inter.*, **45**(4), 324–336.
- Irifune, T., 1994. Absence of an aluminous phase in the upper part of the earth's lower mantle, *Nature*, **370**(6485), 131–133.
- Irifune, T. & Isshiki, M., 1998. Iron partitioning in a pyrolite mantle and the nature of the 410-km seismic discontinuity, *Nature*, **392**(6677), 702–705.
- Irifune, T. & Ringwood, A.E., 1987. Phase-transformations in a harzburgite composition to 26 GPa - implications for dynamical behavior of the subducting slab, *Earth planet. Sci. Lett.*, **86**(2-4), 365–376.
- Irifune, T., Sekine, T., Ringwood, A.E. & Hibberson, W.O., 1986. The eclogite-garnetite transformation at high-pressure and some geophysical implications, *Earth planet. Sci. Lett.*, **77**(2), 245–256.
- Ita, J. & Stixrude, L., 1992. Petrology, elasticity, and composition of the mantle transition zone, *J. geophys. Res.*, **97**(B5), 6849–6866.
- Ito, E. & Navrotsky, A., 1985.  $\text{MgSiO}_3$  ilmenite - calorimetry, phase-equilibria, and decomposition at atmospheric-pressure, *Am. Mineral.*, **70**(9-10), 1020–1026.
- Ito, E. & Takahashi, E., 1989. Postspinel transformations in the system  $\text{Mg}_2\text{SiO}_4$ - $\text{Fe}_2\text{SiO}_4$  and some geophysical implications, *J. geophys. Res.*, **94**(B8), 10637–10646.
- Ito, E. & Yamada, H., 1982. Stability relations of silicate spinels, ilmenites, and perovskites, in *High-Pressure Research in Geophysics*, pp. 405–420, eds Akimoto, S. & Manghnani, M.H., Advances in Earth and Planetary Sciences, Center for Academic Publications Japan, Tokyo.
- Jackson, I. & Niesler, H., 1982. The elasticity of periclase to 3 GPa and some geophysical implications, in *High-Pressure Research in Geophysics*, pp. 93–133, eds Akimoto, S. & Manghnani, M.H., Center for Academic Publications, Tokyo.
- Jackson, I., Khanna, S.K., Revcolevschi, A. & Berthon, J., 1990. Elasticity, shear-mode softening and high-pressure polymorphism of wustite ( $\text{Fe}_{1-x}\text{O}$ ), *J. geophys. Res.*, **95**(B13), 21671–21685.
- Jackson, J.M., Sinogeikin, S.V. & Bass, J.D., 1999. Elasticity of  $\text{MgSiO}_3$  orthoenstatite, *Am. Mineral.*, **84**(4), 677–680.
- Jackson, J.M., Palko, J.W., Andrault, D., Sinogeikin, S.V., Lakshtanov, D.L., Wang, J.Y., Bass, J.D. & Zha, C.S., 2003. Thermal expansion of natural orthoenstatite to 1473 K, *Eur. J. Mineral.*, **15**(3), 469–473.
- Jackson, J.M., Sinogeikin, S.V., Carpenter, M.A. & Bass, J.D., 2004. Novel phase transition in orthoenstatite, *Am. Mineral.*, **89**(1), 239–244.

- Jackson, J.M., Sinogeikin, S.V. & Bass, J.D., 2007. Sound velocities and single-crystal elasticity of orthoenstatite to 1073 K at ambient pressure, *Phys. Earth planet. Inter.*, **161**(1–2), 1–12.
- Jacobs, M.H.G. & de Jong, B.H.W.S., 2007. Placing constraints on phase equilibria and thermophysical properties in the system MgO-SiO<sub>2</sub> by a thermodynamically consistent vibrational method, *Geochim. Cosmochim. Acta*, **71**, 3630–3655.
- Jacobsen, S.D., Reichmann, H.J., Spetzler, H.A., Mackwell, S.J., Smyth, J.R., Angel, R.J. & McCammon, C.A., 2002. Structure and elasticity of single-crystal (Mg, Fe)O and a new method of generating shear waves for gigahertz ultrasonic interferometry, *J. geophys. Res.*, **107**(B2), 2037, doi:10.1029/2001JB000490.
- Jamieson, H.E. & Roeder, P.L., 1984. The distribution of Mg and Fe<sup>2+</sup> between olivine and spinel at 1300°C, *Am. Mineral.*, **69**(3–4), 283–291.
- Jeanloz, R., 1987. Coexistence curves and equilibrium boundaries for high-pressure phase-transformations, *J. geophys. Res.*, **92**(B10), 10352–10362.
- Jeanloz, R. & Thompson, A.B., 1983. Phase transitions and mantle discontinuities, *Rev. Geophys.*, **21**, 51–74.
- Jiang, F.M., Speziale, S. & Duffy, T.S., 2004. Single-crystal elasticity of grossular- and almandine-rich garnets to 11 GPa by Brillouin scattering, *J. geophys. Res.*, **109**(B10), B10210, doi:10.1029/2004JB003081.
- Jung, D.Y., Vinograd, V.L., Fabrichnaya, O.B., Oganov, A.R., Schmidt, M.W. & Winkler, B., 2010. Thermodynamics of mixing in MgSiO<sub>3</sub>-Al<sub>2</sub>O<sub>3</sub> perovskite and ilmenite from ab initio calculations, *Earth planet. Sci. Lett.*, **295**, 477–486.
- Kandelin, J. & Weidner, D.J., 1988a. The single-crystal elastic properties of jadeite, *Phys. Earth planet. Inter.*, **50**(3), 251–260.
- Kandelin, J. & Weidner, D.J., 1988b. Elastic properties of hedenbergite, *J. geophys. Res.*, **93**(B2), 1063–1072.
- Karki, B.B. & Crain, J., 1998. First-principles determination of elastic properties of CaSiO<sub>3</sub> perovskite at lower mantle pressures, *Geophys. Res. Lett.*, **25**(14), 2741–2744.
- Karki, B.B., Warren, M.C., Stixrude, L., Ackland, G.J. & Crain, J., 1997a. Ab initio studies of high-pressure structural transformations in silica, *Phys. Rev. B*, **55**, 3465–3471.
- Karki, B.B., Warren, M.C., Stixrude, L., Ackland, G.J. & Crain, J., 1997b. Erratum: Ab initio studies of high-pressure structural transformations in silica, *Phys. Rev. B*, **56**, 2884–2884.
- Karpov, I.K., Chudnenko, K.V. & Kulik, D.A., 1997. Modeling chemical mass transfer in geochemical processes: thermodynamic relations, conditions of equilibria, and numerical algorithms, *Am. J. Sci.*, **297**(8), 767–806.
- Katsura, T., Ueda, Y., Ito, E. & Morooka, K., 1998. Post-spinel transition in Fe<sub>2</sub>SiO<sub>4</sub>, in *Properties of Earth and Planetary Materials*, pp. 435–440, eds Manghnani, M.H. & Yagi, T., Geophysical Monograph Series, AGU, Washington, DC.
- Katsura, T. *et al.*, 2004. Olivine-wadsleyite transition in the system (Mg, Fe)<sub>2</sub>SiO<sub>4</sub>, *J. geophys. Res.*, **109**(B2), B02209, doi:10.1029/2003JB002438.
- Katsura, T. *et al.*, 2009. P-V-T relations of MgSiO<sub>3</sub> perovskite determined by in situ X-ray diffraction using a large-volume high-pressure apparatus, *Geophys. Res. Lett.*, **36**, L01305, doi:10.1029/2008GL035658.
- Kavner, A. & Walker, D., 2006. Core/mantle-like interactions in an electric field, *Earth planet. Sci. Lett.*, **248**, 316–329.
- Kerrick, D.M. & Darken, L.S., 1975. Statistical thermodynamic models for ideal oxide and silicate solid-solutions, with application to plagioclase, *Geochim. Cosmochim. Acta*, **39**(10), 1431–1442.
- Khan, A., Connolly, J.A.D. & Olsen, N., 2006. Constraining the composition and thermal state of the mantle beneath Europe from inversion of long-period electromagnetic sounding data, *J. geophys. Res.*, **111**(B10), doi:10.1029/2006JB004270.
- Khan, A., Boschi, L. & Connolly, J.A.D., 2009. On mantle chemical and thermal heterogeneities and anisotropy as mapped by inversion of global surface wave data, *J. geophys. Res.*, **114**, B09305, doi:10.1029/2009JB006399.
- Kiefer, B., Stixrude, L. & Wentzcovitch, R.M., 2002. Elasticity of (Mg, Fe)SiO<sub>3</sub>-perovskite at high pressures, *Geophys. Res. Lett.*, **29**(11), 1539, doi:10.1029/2002GL014683.
- Kieffer, S.W., 1980. Thermodynamics and lattice-vibrations of minerals 4: application to chain and sheet silicates and orthosilicates, *Rev. Geophys.*, **18**, 862–886.
- Kimizuka, H., Ogata, S., Li, J. & Shibutani, Y., 2007. Complete set of elastic constants of alpha-quartz at high pressure: a first-principles study, *Phys. Rev. B*, **75**(5), 054109, doi:10.1103/PhysRevB.75.054109.
- Klemme, S. & O'Neill, H.S.C., 2000. The near-solidus transition from garnet to hercynite to spinel hercynite, *Contrib. Mineral. Petrol.*, **138**(3), 237–248.
- Knittle, E., 1995. Static compression measurements of equations of state, in *Mineral Physics and Crystallography: A Handbook of Physical Constants*, pp. 98–142, ed. Ahrens, T.J., AGU, Washington, DC.
- Kroll, H., Lueder, T., Schlenz, H., Kirfel, A. & Vad, T., 1997. The Fe<sup>2+</sup>, Mg distribution in orthopyroxene: a critical assessment of its potential as a geospeedometer, *Eur. J. Mineral.*, **9**(4), 705–733.
- Krupka, K.M., Robie, R.A. & Hemingway, B.S., 1979. High-temperature heat-capacities of corundum, periclase, anorthite, CaAl<sub>2</sub>Si<sub>2</sub>O<sub>8</sub> glass, muscovite, pyrophyllite, KAlSi<sub>3</sub>O<sub>8</sub> glass, grossular, and NaAlSi<sub>3</sub>O<sub>8</sub> glass, *Am. Mineral.*, **64**(1–2), 86–101.
- Krupka, K.M., Robie, R.A., Hemingway, B.S., Kerrick, D.M. & Ito, J., 1985. Low-temperature heat-capacities and derived thermodynamic properties of anthophyllite, diopside, enstatite, bronzite, and wollastonite, *Am. Mineral.*, **70**(3–4), 249–260.
- Kubo, A. & Akaogi, M., 2000. Post-garnet transitions in the system Mg<sub>4</sub>Si<sub>4</sub>O<sub>12</sub>-Mg<sub>3</sub>Al<sub>2</sub>Si<sub>3</sub>O<sub>12</sub> up to 28 GPa: phase relations of garnet, ilmenite and perovskite, *Phys. Earth planet. Inter.*, **121**(1–2), 85–102.
- Kubo, T., Ohtani, E., Kato, T., Kondo, T., Hosoya, T., Sano, A. & Kikegawa, T., 2008. Kinetics of the post-garnet transformation: implications for density and rheology of subducting slabs, *Phys. Earth planet. Inter.*, **170**(3–4), 181–192.
- Kubo, T., Kaneshima, S., Torii, Y. & Yoshioka, S., 2009. Seismological and experimental constraints on metastable phase transformations and rheology of the Mariana slab, *Earth planet. Sci. Lett.*, **287**(1–2), 12–23.
- Kung, J., Li, B.S., Uchida, T. & Wang, Y.B., 2005. In-situ elasticity measurement for the unquenchable high-pressure clinopyroxene phase: Implication for the upper mantle, *Geophys. Res. Lett.*, **32**(1), L01307, doi:10.1029/2004GL021661.
- Kushiro, I. & Yoder, H.S., 1966. Anorthite-forsterite and anorthite-enstatite reactions and their bearing on basalt-eclogite transformation, *J. Petrol.*, **7**(3), 337–362.
- Kuskov, O.L., 1995. Constitution of the moon. 3. Composition of middle mantle from seismic data, *Phys. Earth planet. Inter.*, **90**(1–2), 55–74.
- Latimer, W.M., 1951. Methods of estimating the entropies of solid compounds, *J. Am. Chem. Soc.*, **73**(4), 1480–1482.
- Levien, L. & Prewitt, C.T., 1981. High-pressure structural study of diopside, *Am. Mineral.*, **66**(3–4), 315–323.
- Li, B.S., Liebermann, R.C. & Weidner, D.J., 2001. P-V-Vp-Vs-T measurements on wadsleyite to 7 GPa and 873 K: implications for the 410-km seismic discontinuity, *J. geophys. Res.*, **106**(B12), 30579–30591.
- Li, L. & Weidner, D.J., 2008. Effect of phase transitions on compressional-wave velocities in the Earth's mantle, *Nature*, **454**(7207), 984–986.
- Limadefaria, J., Hellner, E., Liebau, F., Makovicky, E. & Parthe, E., 1990. Nomenclature of inorganic structure types—report of the International Union of Crystallography Commission on Crystallographic Nomenclature Subcommittee on the nomenclature of inorganic structure types, *Acta Crystallogr. Sect. A*, **46**, 1–11.
- Lin, J.F., Degtyareva, O., Prewitt, C.T., Dera, P., Sata, N., Gregoryanz, E., Mao, H.K. & Hemley, R.J., 2004. Crystal structure of a high-pressure/high-temperature phase of alumina by in situ X-ray diffraction, *Nat. Mater.*, **3**(6), 389–393.
- Lindsley, D.H., 1983. Pyroxene thermometry, *Am. Mineral.*, **68**(5–6), 477–493.
- Liu, J., Topor, L., Zhang, J., Navrotsky, A. & Liebermann, R.C., 1996. Calorimetric study of the coesite stishovite transformation and calculation of the phase boundary, *Phys. Chem. Miner.*, **23**(1), 11–16.
- Liu, J., Zhang, J.Z., Flesch, L., Li, B.S., Weidner, D.J. & Liebermann, R.C., 1999. Thermal equation of state of stishovite, *Phys. Earth planet. Inter.*, **112**(3–4), 257–266.

- Liu, X., 2006. Phase relations in the system  $\text{KAlSi}_3\text{O}_8$ – $\text{NaAlSi}_3\text{O}_8$  at high pressure–temperature conditions and their implications for the petrogenesis of lingunite, *Earth planet. Sci. Lett.*, **246**, 317–325.
- Macdonald, J.R., 1969. Review of some experimental and analytical equations of state, *Rev. Modern Phys.*, **41**(2), 316–349.
- Mao, H.K., Takahashi, T., Bassett, W.A. & Weaver, J.S., 1969. Effect of pressure and temperature on molar volumes of wustite and of 3 (Fe Mg) $_2$ SiO $_4$  spinel solid solutions, *J. geophys. Res.*, **74**(4), 1061–1069.
- Mao, H.K., Shen, G.Y. & Hemley, R.J., 1997. Multivariable dependence of Fe–Mg partitioning in the lower mantle, *Science*, **278**(5346), 2098–2100.
- Mao, W.L. *et al.*, 2005. Iron-rich silicates in the Earth's D'' layer, *Proc. Natl. Acad. Sci. U.S.A.*, **102**(28), 9751–9753.
- Marquardt, H., Speziale, S., Reichmann, H.J., Frost, D.J., Schilling, F.R. & Garnero, E.J., 2009. Elastic shear anisotropy of ferropericlase in Earth's lower mantle, *Science*, **324**(5924), 224–226.
- Martinez, I., Wang, Y.B., Guyot, F., Liebermann, R.C. & Doukhan, J.C., 1997. Microstructures and iron partitioning in (Mg, Fe)SiO $_3$  perovskite (Mg, Fe)O magnesiowustite assemblages: an analytical transmission electron microscopy study, *J. geophys. Res.*, **102**(B3), 5265–5280.
- Matas, J., 1999. Modélisation Thermochimique des Propriétés de Solides à Hautes Températures et Hautes Pressions. Applications Géophysiques, *PhD thesis*, École Normale Supérieure de Lyon.
- Matsuzaka, K., Akaogi, M., Suzuki, T. & Suda, T., 2000. Mg–Fe partitioning between silicate spinel and magnesiowustite at high pressure: experimental determination and calculation of phase relations in the system Mg $_2$ SiO $_4$ –Fe $_2$ SiO $_4$ , *Phys. Chem. Miner.*, **27**(5), 310–319.
- Mattern, E., Matas, J., Ricard, Y. & Bass, J., 2005. Lower mantle composition and temperature from mineral physics and thermodynamic modelling, *Geophys. J. Int.*, **160**(3), 973–990.
- Mirwald, P.W. & Massone, H.-J., 1980. The low-high quartz and quartz-coesite transition to 40 kbar between 600 and 1600 °C and some reconnaissance data on the effect of NaAlO $_2$  component on the low quartz-coesite transition, *J. geophys. Res.*, **85**(NB12), 6983–6990.
- Miyake, A., Shimobayashi, N. & Kitamura, M., 2004. Isosymmetric structural phase transition of orthoenstatite: molecular dynamics simulation, *Am. Mineral.*, **89**(11–12), 1667–1672.
- Mookherjee, M., 2010. Structure, energetics, and elasticity of aluminous phases at high pressures, *Earth planet. Sci. Lett.*, submitted.
- Morishima, H., Kato, T., Suto, M., Ohtani, E., Urakawa, S., Utsumi, W., Shimomura, O. & Kikegawa, T., 1994. The phase-boundary between Alpha-Mg $_2$ SiO $_4$  and Beta-Mg $_2$ SiO $_4$  determined by in-situ X-ray observation, *Science*, **265**(5176), 1202–1203.
- Murakami, M., Hirose, K., Ono, S. & Ohishi, Y., 2003. Stability of CaCl $_2$ -type and alpha PbO $_2$ -type SiO $_2$  at high pressure and temperature determined by in situ X-ray measurements, *Geophys. Res. Lett.*, **30**(5), 1207.
- Murakami, M., Sinogeikin, S.V., Bass, J.D., Sata, N., Ohishi, Y. & Hirose, K., 2007. Sound velocity of MgSiO $_3$  post-perovskite phase: a constraint on the D'' discontinuity, *Earth planet. Sci. Lett.*, **259**(1–2), 18–23.
- Murakami, M., Ohishi, Y., Hirao, N. & Hirose, K., 2009. Elasticity of MgO to 130 GPa: implications for lower mantle mineralogy, *Earth planet. Sci. Lett.*, **277**(1–2), 123–129.
- Murnaghan, F.D., 1944. The compressibility of media under extreme pressure, *Proc. Natl. Acad. Sci. U.S.A.*, **30**, 244–247.
- Nakagawa, T., Tackley, P.J., Deschamps, F. & Connolly, J.A.D., 2009. Incorporating self-consistently calculated mineral physics into thermochemical mantle convection simulations in a 3-D spherical shell and its influence on seismic anomalies in Earth's mantle, *Geochim. Geophys. Geosyst.*, **10**, Q03004, doi:10.1029/2008GC002280
- Newton, R.C., Charlu, T.V. & Kleppa, O.J., 1977. Thermochemistry of high-pressure garnets and clinopyroxenes in system CaO–MgO–Al $_2$ O $_3$ –SiO $_2$ , *Geochim. Cosmochim. Acta*, **41**(3), 369–377.
- Oganov, A.R. & Ono, S., 2005. The high-pressure phase of alumina and implications for Earth's D'' layer, *Proc. Natl. Acad. Sci. U.S.A.*, **102**(31), 10828–10831.
- Ohi, S., Miyake, A., Shimobayashi, N., Yashima, M. & Kitamura, M., 2008. An isosymmetric phase transition of orthopyroxene found by high-temperature X-ray diffraction, *Am. Mineral.*, **93**(10), 1682–1685.
- Ohno, I., Harada, K. & Yoshitomi, C., 2006. Temperature variation of elastic constants of quartz across the alpha-beta transition, *Phys. Chem. Miner.*, **33**(1), 1–9.
- Ohtani, E. & Sakai, T., 2008. Recent advances in the study of mantle phase transitions, *Phys. Earth planet. Inter.*, **170**(3–4), 240–247.
- Ohtani, E., Kagawa, N. & Fujino, K., 1991. Stability of majorite (Mg, Fe)SiO $_3$  at high pressures and 1800 °C, *Earth planet. Sci. Lett.*, **102**(2), 158–166.
- Okamura, F.P., Ghose, S. & Ohashi, H., 1974. Structure and crystal chemistry of calcium tschermak's pyroxene, CaAlAlSiO $_6$ , *Am. Mineral.*, **59**, 549–557.
- O'Neill, H.S.C., McCammon, C.A., Canil, D., Rubie, D.C., Ross, C.R. & Seifert, F., 1993. Mossbauer-spectroscopy of mantle transition zone phases and determination of minimum Fe $^{3+}$  content, *Am. Mineral.*, **78**(3–4), 456–460.
- Ono, S., Hirose, K., Murakami, M. & Isshiki, M., 2002. Post-stishovite phase boundary in SiO $_2$  determined by in situ X-ray observations, *Earth planet. Sci. Lett.*, **197**(3–4), 187–192.
- Ono, S., Oganov, A.R., Koyama, T. & Shimizu, H., 2006. Stability and compressibility of the high-pressure phases of Al $_2$ O $_3$  up to 200 GPa: implications for the electrical conductivity of the base of the lower mantle, *Earth planet. Sci. Lett.*, **246**(3–4), 326–335.
- Ono, S., Brodholt, J.P. & Price, G.D., 2008. First-principles simulation of high-pressure polymorphs in MgAl $_2$ O $_4$ , *Phys. Chem. Miner.*, **35**(7), 381–386.
- Pacalo, R.E.G. & Gasparik, T., 1990. Reversals of the orthoenstatite-clinoenstatite transition at high-pressures and high-temperatures, *J. geophys. Res.*, **95**(B10), 15 853–15 858.
- Panero, W.R., Akber-Knutson, S. & Stixrude, L., 2006. Al $_2$ O $_3$  incorporation in MgSiO $_3$  perovskite and ilmenite, *Earth planet. Sci. Lett.*, **252**(1–2), 152–161.
- Perkins, D. & Newton, R.C., 1980. The compositions of coexisting pyroxenes and garnet in the system CaO–MgO–Al $_2$ O $_3$ –SiO $_2$  at 900 °–1,100 °C and high-pressures, *Contrib. Mineral. Petrol.*, **75**(3), 291–300.
- Perkins, D., Holland, T.J.B. & Newton, R.C., 1981. The Al $_2$ O $_3$  contents of enstatite in equilibrium with garnet in the system MgO–Al $_2$ O $_3$ –SiO $_2$  at 15–40 kbar and 900 °C–1600 °C, *Contrib. Mineral. Petrol.*, **78**(1), 99–109.
- PERPLEX, 2010. <http://www.perplex.ethz.ch/>.
- Persson, K., Ceder, G., Berta, A. & Morgan, D., 2006. Ab initio study of the composition dependence of the pressure-induced spin transition in the (Mg $_{1-x}$ , Fe $_x$ )O system, *Geophys. Res. Lett.*, **33**, L16306, doi:10.1029/2006GL026621.
- Piazzoni, A.S., Steinle-Neumann, G., Bunge, H.P. & Dolejs, D., 2007. A mineralogical model for density and elasticity of the Earth's mantle, *Geochim. Geophys. Geosyst.*, **8**(11), Q11010, doi:10.1029/2007GC001697.
- Powell, R., 1974. Comparison of some mixing models for crystalline silicate solid-solutions, *Contrib. Mineral. Petrol.*, **46**(4), 265–274.
- Powell, R. & Holland, T., 1993. On the formulation of simple mixing models for complex phases, *Am. Mineral.*, **78**(11–12), 1174–1180.
- Presnall, D.C., Weng, Y.H., Milholland, C.S. & Walter, M.J., 1998. Liquidus phase relations in the system MgO–MgSiO $_3$  at pressures up to 25 GPa—constraints on crystallization of a molten Hadean mantle, *Phys. Earth planet. Inter.*, **107**(1–3), 83–95.
- Press, W.H., Teukolsky, S.A., Vetterling, W.T. & Flannery, B.P., 1992. *Numerical Recipes in FORTRAN: The Art of Scientific Computing*, Cambridge University Press, New York.
- Putnis, A., 1992. *Introduction to Mineral Sciences*, Cambridge University Press, Cambridge.
- Redlich, O. & Kister, A.T., 1948. Algebraic representation of thermodynamic properties and the classification of solutions, *Ind. Eng. Chem.*, **40**(2), 345–348.
- Reichmann, H.J., Sinogeikin, S.V., Bass, J.D. & Gasparik, T., 2002. Elastic moduli of jadeite-enstatite majorite, *Geophys. Res. Lett.*, **29**(19), 1936.
- Ricard, Y., Mattern, E. & Matas, J., 2005. Synthetic tomographic images of slabs from mineral physics, in *Earth's Deep Mantle: Structure, Composition, and Evolution*, pp. 283–300, eds Hilst, R.v.d., Bass, J.D., Matas, J. & Trampert, J., AGU, Washington, DC.

- Ricard, Y., Matas, J. & Chambat, F., 2009. Seismic attenuation in a phase change coexistence loop, *Phys. Earth planet. Inter.*, **176**(1–2), 124–131.
- Richet, P., Bottinga, Y., Denielou, L., Petitot, J.P. & Tequi, C., 1982. Thermodynamic properties of quartz, cristobalite, and amorphous SiO<sub>2</sub>—drop calorimetry measurements between 1000 K and 1800 K and a review from 0 K to 2000 K, *Geochim. Cosmochim. Acta*, **46**(12), 2639–2658.
- Ringwood, A.E., 1959. On the chemical evolution and densities of the planets, *Geochim. Cosmochim. Acta*, **15**, 257–283.
- Ringwood, A.E., 1991. Phase transformations and their bearing on the constitution and dynamics of the mantle, *Geochim. Cosmochim. Acta*, **55**, 2083–2110.
- Robie, R.A. & Hemingway, B.S., 1995. *Thermodynamic Properties of Minerals and Related Substances at 298.15 K and 1 Bar (10<sup>5</sup> Pascals) Pressure and at Higher Temperature*, Vol. 2131 of U.S. Geological Survey Bulletin, United States Geological Survey, Washington, DC.
- Robie, R.A., Hemingway, B.S. & Fisher, J.R., 1978. *Thermodynamic Properties of Minerals and Related Substances at 298.15 K and 1 bar (10<sup>5</sup> pascals) Pressure and at Higher Temperatures*, U.S. Geological Survey Bulletin, United States Geological Survey, Washington, DC.
- Saikia, A., Frost, D.J. & Rubie, D.C., 2008. Splitting of the 520-kilometer seismic discontinuity and chemical heterogeneity in the mantle, *Science*, **319**(5869), 1515–1518.
- Saxena, S.K., 1996. Earth mineralogical model: Gibbs free energy minimization computation in the system MgO-FeO-SiO<sub>2</sub>, *Geochim. Cosmochim. Acta*, **60**(13), 2379–2395.
- Saxena, S.K. & Fei, Y., 1988. Fluid mixtures in the C-H-O system at high-pressure and temperature, *Geochim. Cosmochim. Acta*, **52**(2), 505–512.
- Sen, G., 1985. Experimental-determination of pyroxene compositions in the system CaO-MgO-Al<sub>2</sub>O<sub>3</sub>-SiO<sub>2</sub> at 900–1200°C and 10–15 kbar using PbO and H<sub>2</sub>O fluxes, *Am. Mineral.*, **70**(7–8), 678–695.
- Shieh, S.R., Duffy, T.S., Kubo, A., Shen, G.Y., Prakapenka, V.B., Sata, N., Hirose, K. & Ohishi, Y., 2006. Equation of state of the postperovskite phase synthesized from a natural (Mg, Fe)SiO<sub>3</sub> orthopyroxene, *Proc. Natl. Acad. Sci. U.S.A.*, **103**(9), 3039–3043.
- Shim, S.H. & Duffy, T.S., 2000. Constraints on the P-V-T equation of state of MgSiO<sub>3</sub> perovskite, *Am. Mineral.*, **85**(2), 354–363.
- Shim, S.H., Duffy, T.S. & Shen, G.Y., 2000. The stability and P-V-T equation of state of CaSiO<sub>3</sub> perovskite in the Earth's lower mantle, *J. geophys. Res.*, **105**(B11), 25 955–25 968.
- Shimobayashi, N. & Kitamura, M., 1991. Phase-transition in Ca-Poor clinopyroxenes—a high-temperature transmission electron-microscopic study, *Phys. Chem. Miner.*, **18**(3), 153–160.
- Sinmyo, R., Hirose, K., Nishio-Hamane, D., Seto, Y., Fujino, K., Sata, N. & Ohishi, Y., 2008. Partitioning of iron between perovskite/postperovskite and ferropericlasite in the lower mantle, *J. geophys. Res.*, **113**(B11), B11204, doi:10.1029/2008JB005730.
- Sinogeikin, S.V. & Bass, J.D., 2000. Single-crystal elasticity of pyrope and MgO to 20 GPa by brillouin scattering in the diamond cell, *Phys. Earth planet. Inter.*, **120**(1–2), 43–62.
- Sinogeikin, S.V. & Bass, J.D., 2002a. Elasticity of majorite and a majorite-pyrope solid solution to high pressure: implications for the transition zone, *Geophys. Res. Lett.*, **29**(2), 1017, doi:10.1029/2001GL013937.
- Sinogeikin, S.V. & Bass, J.D., 2002b. Elasticity of pyrope and majorite-pyrope solid solutions to high temperatures, *Earth planet. Sci. Lett.*, **203**(1), 549–555.
- Sinogeikin, S.V., Katsura, T. & Bass, J.D., 1998. Sound velocities and elastic properties of Fe-bearing wadsleyite and ringwoodite, *J. geophys. Res.*, **103**(B9), 20 819–20 825.
- Sinogeikin, S.V., Bass, J.D. & Katsura, T., 2001. Single-crystal elasticity of gamma-(Mg<sub>0.91</sub>Fe<sub>0.09</sub>)<sub>2</sub>SiO<sub>4</sub> to high pressures and to high temperatures, *Geophys. Res. Lett.*, **28**(22), 4335–4338.
- Sinogeikin, S.V., Bass, J.D. & Katsura, T., 2003. Single-crystal elasticity of ringwoodite to high pressures and high temperatures: implications for 520 km seismic discontinuity, *Phys. Earth planet. Inter.*, **136**(1–2), 41–66.
- Sinogeikin, S.V., Zhang, J.Z. & Bass, J.D., 2004. Elasticity of single crystal and polycrystalline MgSiO<sub>3</sub> perovskite by brillouin spectroscopy, *Geophys. Res. Lett.*, **31**(6), L06620, doi:10.1029/2004GL019559.
- Smith, W.R. & Missen, R.W., 1982. *Chemical Reaction Equilibrium Analysis*, John Wiley and Sons, New York.
- Smyth, J.R. & McCormick, T.C., 1995. Crystallographic data for minerals, in *Mineral Physics and Crystallography: A Handbook of Physical Constants*, pp. 1–17, ed. Ahrens, T.J., AGU, Washington, DC.
- Sobolev, S.V. & Babeyko, A.Y., 1994. Modeling of mineralogical composition, density and elastic-wave velocities in anhydrous magmatic rocks, *Surveys in Geophysics*, **15**(5), 515–544.
- Stackhouse, S., Brodholt, J.P. & Price, G.D., 2005a. High temperature elastic anisotropy of the perovskite and post-perovskite Al<sub>2</sub>O<sub>3</sub>, *Geophys. Res. Lett.*, **32**(13), L13305, doi:10.1029/2005GL023163.
- Stackhouse, S., Brodholt, J.P., Wookey, J., Kendall, J.M. & Price, G.D., 2005b. The effect of temperature on the seismic anisotropy of the perovskite and post-perovskite polymorphs of MgSiO<sub>3</sub>, *Earth planet. Sci. Lett.*, **230**(1–2), 1–10.
- Stackhouse, S., Brodholt, J.P., Dobson, D.P. & Price, G.D., 2006a. Electronic spin transitions and the seismic properties of ferrous iron-bearing MgSiO<sub>3</sub> post-perovskite, *Geophys. Res. Lett.*, **33**(12), L12S03, doi:10.1029/2005GL025589.
- Stackhouse, S., Brodholt, J.P. & Price, G.D., 2006b. Elastic anisotropy of FeSiO<sub>3</sub> end-members of the perovskite and post-perovskite phases, *Geophys. Res. Lett.*, **33**(1), L01304, doi:10.1029/2005GL023887.
- Stackhouse, S., Stixrude, L. & Karki, B.B., 2010. Determination of the high-pressure properties of fayalite from first-principles calculations, *Earth planet. Sci. Lett.*, **289**(3–4), 449–456.
- Stixrude, L., 1997. Structure and sharpness of phase transitions and mantle discontinuities, *J. geophys. Res.*, **102**(B7), 14 835–14 852.
- Stixrude, L. & Bukowinski, M.S.T., 1990. Fundamental thermodynamic relations and silicate melting with implications for the constitution of D'', *J. geophys. Res.*, **95**, 19 311–19 325.
- Stixrude, L. & Bukowinski, M.S.T., 1993. Thermodynamic analysis of the system MgO-FeO-SiO<sub>2</sub> at high pressure and the structure of the lowermost mantle, in *Evolution of the Earth and Planets*, pp. 131–142, eds Takahashi, E., Jeanloz, R. & Rubie, D., International Union of Geodesy and Geophysics, Washington, DC.
- Stixrude, L. & Lithgow-Bertelloni, C., 2005a. Thermodynamics of mantle minerals—I. Physical properties, *Geophys. J. Int.*, **162**(2), 610–632.
- Stixrude, L. & Lithgow-Bertelloni, C., 2005b. Mineralogy and elasticity of the oceanic upper mantle: origin of the low-velocity zone, *J. geophys. Res.*, **110**(B3), B03204, doi:10.1029/2004JB002965.
- Stixrude, L. & Lithgow-Bertelloni, C., 2007. Influence of phase transformations on lateral heterogeneity and dynamics in Earth's mantle, *Earth planet. Sci. Lett.*, **263**(1–2), 45–55.
- Stolen, S., Glockner, R., Gronvold, F., Atake, T. & Izumisawa, S., 1996. Heat capacity and thermodynamic properties of nearly stoichiometric wustite from 13 to 450 K, *Am. Mineral.*, **81**(7–8), 973–981.
- Sundman, B. & Agren, J., 1981. A regular solution model for phases with several components and sub-lattices, suitable for computer-applications, *J. Phys. Chem. Solids*, **42**(4), 297–301.
- Suzuki, A. *et al.*, 2000. In situ determination of the phase boundary between wadsleyite and ringwoodite in Mg<sub>2</sub>SiO<sub>4</sub>, *Geophys. Res. Lett.*, **27**(6), 803–806.
- Takafuji, N., Yagi, T., Miyajima, N. & Sumita, T., 2002. Study on Al<sub>2</sub>O<sub>3</sub> content and phase stability of aluminous-CaSiO<sub>3</sub> perovskite at high pressure and temperature, *Phys. Chem. Miner.*, **29**(8), 532–537.
- Tange, Y., Takahashi, E., Nishihara, Y., Funakoshi, K.I. & Sata, N., 2009. Phase relations in the system MgO-FeO-SiO<sub>2</sub> to 50 GPa and 2000°C: an application of experimental techniques using multianvil apparatus with sintered diamond anvils, *J. geophys. Res.*, **114**, B02214, doi:10.1029/2008JB005891.
- Tateno, S., Hirose, K., Sata, N. & Ohishi, Y., 2007. Solubility of FeO in (Mg, Fe)SiO<sub>3</sub> perovskite and the post-perovskite phase transition, *Phys. Earth planet. Inter.*, **160**(3–4), 319–325.
- Tateno, S., Hirose, K., Sata, N. & Ohishi, Y., 2009. Determination of post-perovskite phase transition boundary up to 4400 K and implications for thermal structure in D'' layer, *Earth planet. Sci. Lett.*, **277**(1–2), 130–136.
- Thieblot, L., Roux, J. & Richet, P., 1998. High-temperature thermal expansion and decomposition of garnets, *Eur. J. Mineral.*, **10**(1), 7–15.

- Thieblot, L., Tequi, C. & Richet, P., 1999. High-temperature heat capacity of grossular ( $\text{Ca}_3\text{Al}_2\text{Si}_3\text{O}_{12}$ ), enstatite ( $\text{MgSiO}_3$ ), and titanite ( $\text{CaTiSiO}_5$ ), *Am. Mineral.*, **84**(5–6), 848–855.
- Thompson, J.B., 1969. Chemical reactions in crystals, *Am. Mineral.*, **54**(3–4), 341–375.
- Tsuchiya, J. & Tsuchiya, T., 2008. Postperovskite phase equilibria in the  $\text{MgSiO}_3$ – $\text{Al}_2\text{O}_3$  system, *Proc. Natl. Acad. Sci. U.S.A.*, **105**(49), 19160–19164.
- Tsuchiya, J., Tsuchiya, T. & Wentzcovitch, R.M., 2005. Transition from the  $\text{Rh}_2\text{O}_3$ (II)-to- $\text{CaIrO}_3$  structure and the high-pressure-temperature phase diagram of alumina, *Phys. Rev. B*, **72**(2), 020103, doi:10.1103/PhysRevB.72.020103.
- Tsuchiya, T., Tsuchiya, J., Umemoto, K. & Wentzcovitch, R.A., 2004. Phase transition in  $\text{MgSiO}_3$  perovskite in the Earth's lower mantle, *Earth planet. Sci. Lett.*, **224**(3–4), 241–248.
- Ulbrich, H.H. & Waldbaum, D.R., 1976. Structural and other contributions to 3rd-law entropies of silicates, *Geochim. Cosmochim. Acta*, **40**(1), 1–24.
- Valencia, D., O'Connell, R.J. & Sasselov, D., 2006. Internal structure of massive terrestrial planets, *Icarus*, **181**(2), 545–554.
- Verhooogen, J., 1965. Physics of convection currents in earth's mantle. 22. phase changes and convection in earth's mantle, *Phil. Trans. R. Soc. Lond., A*, **258**(1088), 276–283.
- Vinograd, V.L., Winkler, B., Putnis, A., Kroll, H., Milman, V., Gale, J.D. & Fabrichnaya, O.B., 2006. Thermodynamics of pyrope-majorite,  $\text{Mg}_3\text{Al}_2\text{Si}_3\text{O}_{12}$ – $\text{Mg}_4\text{Si}_4\text{O}_{12}$ , solid solution from atomistic model calculations, *Mol. Simul.*, **32**(2), 85–99.
- Wallace, D.C., 1972. *Thermodynamics of Crystals*, 1st edn, John Wiley and Sons, New York.
- Walter, M.J., Kubo, A., Yoshino, T., Brodholt, J., Koga, K.T. & Ohishi, Y., 2004. Phase relations and equation-of-state of aluminous Mg-silicate perovskite and implications for Earth's lower mantle, *Earth planet. Sci. Lett.*, **222**(2), 501–516.
- Wang, J.W., Kalinichev, A.G. & Kirkpatrick, R.J., 2004. Molecular modeling of the 10-angstrom phase at subduction zone conditions, *Earth planet. Sci. Lett.*, **222**(2), 517–527.
- Wang, Y., Weidner, D.J. & Guyot, F., 1996. Thermal equation of state of  $\text{CaSiO}_3$  perovskite, *J. geophys. Res.*, **101**, 661–672.
- Wang, Y.B., Weidner, D.J., Zhang, J.Z., Gwanresnia, G.D. & Liebermann, R.C., 1998. Thermal equation of state of garnets along the pyrope-majorite join, *Phys. Earth planet. Inter.*, **105**(1–2), 59–71.
- Weidner, D.J., 1985. A mineral physics test of a pyrolite mantle, *Geophys. Res. Lett.*, **12**(7), 417–420.
- Weidner, D.J. & Carleton, H.R., 1977. Elasticity of coesite, *J. geophys. Res.*, **82**(8), 1334–1346.
- Weidner, D.J., Bass, J.D., Ringwood, A.E. & Sinclair, W., 1982. The single-crystal elastic moduli of stishovite, *J. geophys. Res.*, **87**, 4740–4746.
- Wentzcovitch, R.M., Karki, B.B., Cococcioni, M. & de Gironcoli, S., 2004a. Thermoelectric properties of  $\text{MgSiO}_3$ -perovskite: insights on the nature of the earth's lower mantle, *Phys. Rev. Lett.*, **92**(1), 018501, doi:10.1103/PhysRevLett.92.018501.
- Wentzcovitch, R.M., Stixrude, L., Karki, B.B. & Kiefer, B., 2004b. Akimotoite to perovskite phase transition in  $\text{MgSiO}_3$ , *Geophys. Res. Lett.*, **31**(10), L10611, doi:10.1029/2004GL019704.
- Wiser, N.M. & Wood, B.J., 1991. Experimental-determination of activities in Fe-Mg olivine at 1400-K, *Contrib. Mineral. Petrol.*, **108**(1–2), 146–153.
- Wood, B.J. & Holloway, J.R., 1984. A thermodynamic model for subsolidus equilibria in the system  $\text{CaO}$ – $\text{MgO}$ – $\text{Al}_2\text{O}_3$ – $\text{SiO}_2$ , *Geochim. Cosmochim. Acta*, **48**(1), 159–176.
- Woodland, A.B. & Angel, R.J., 1997. Reversal of the orthoferrosilite-high-P clinoferrosilite transition, a phase diagram for  $\text{FeSiO}_3$  and implications for the mineralogy of the Earth's upper mantle, *Eur. J. Mineral.*, **9**(2), 245–254.
- Workman, R.K. & Hart, S.R., 2005. Major and trace element composition of the depleted MORB mantle (DMM), *Earth planet. Sci. Lett.*, **231**(1–2), 53–72.
- Xu, W.B., Lithgow-Bertelloni, C., Stixrude, L. & Ritsema, J., 2008. The effect of bulk composition and temperature on mantle seismic structure, *Earth planet. Sci. Lett.*, **275**(1–2), 70–79.
- Yagi, A., Suzuki, T. & Akaogi, M., 1994. High-pressure transitions in the system  $\text{KAlAl}_3\text{O}_8$ – $\text{NaAlSi}_3\text{O}_8$ , *Phys. Chem. Miner.*, **21**(1–2), 12–17.
- Yagi, T., Akaogi, M., Shimomura, O., Suzuki, T. & Akimoto, S., 1987. In situ observation of the olivine-spinel phase-transformation in  $\text{Fe}_2\text{SiO}_4$  using synchrotron radiation, *J. geophys. Res.*, **92**(B7), 6207–6213.
- Yamada, H., Matsui, Y. & Ito, E., 1983. Crystal-chemical characterization of  $\text{NaAlSiO}_4$  with the  $\text{CaFe}_2\text{O}_4$  structure, *Mineral. Mag.*, **47**(343), 177–181.
- Yang, H.X. & Ghose, S., 1995. High-temperature single-crystal X-ray-diffraction studies of the ortho-ortho phase-transition in enstatite,  $\text{Mg}_2\text{Si}_2\text{O}_6$  at 1360 K, *Phys. Chem. Miner.*, **22**(5), 300–310.
- Yoneda, A., 1990. Pressure derivatives of elastic-constants of single-crystal  $\text{MgO}$  and  $\text{MgAl}_2\text{O}_4$ , *J. Phys. Earth*, **38**(1), 19–55.
- Zha, C.S., Duffy, T.S., Downs, R.T., Mao, H.K. & Hemley, R.J., 1996. Sound velocity and elasticity of single-crystal forsterite to 16 GPa, *J. geophys. Res.*, **101**(B8), 17 535–17 545.
- Zha, C.S., Duffy, T.S., Mao, H.K., Downs, R.T., Hemley, R.J. & Weidner, D.J., 1997. Single-crystal elasticity of beta- $\text{Mg}_2\text{SiO}_4$  to the pressure of the 410 km seismic discontinuity in the Earth's mantle, *Earth planet. Sci. Lett.*, **147**(1–4), E9–E15.
- Zha, C.S., Duffy, T.S., Downs, R.T., Mao, H.K. & Hemley, R.J., 1998. Brillouin scattering and X-ray diffraction of San Carlos Olivine: direct pressure determination to 32 GPa, *Earth planet. Sci. Lett.*, **159**(1–2), 25–33.
- Zhang, J., Li, B., Utsumi, W. & Liebermann, R.C., 1996. In situ X-ray observations of the coesite stishovite transition: reversed phase boundary and kinetics, *Phys. Chem. Miner.*, **23**(1), 1–10.
- Zhao, Y., Dreele, J.V., Zhang, J. & Weidner, D.J., 1998. Thermoelastic equation of state of monoclinic pyroxene:  $\text{CaMgSi}_2\text{O}_6$ , *Rev. High Pressure Sci. Technol.*, **7**, 25–27.
- Zhao, Y.S., VonDreele, R.B., Shankland, T.J., Weidner, D.J., Zhang, J.Z., Wang, Y.B. & Gasparik, T., 1997. Thermoelastic equation of state of jadeite  $\text{NaAlSi}_2\text{O}_6$ : an energy-dispersive reitveld refinement study of low symmetry and multiple phases diffraction, *Geophys. Res. Lett.*, **24**(1), 5–8.

## APPENDIX A: GLOBAL INVERSION

Our strategy for estimating the parameters is based on a two-part iterative global least-squares inversion of a wide variety of experimental data. The first step of our inversion is discussed in Paper I in which we describe our method for the determination of the parameters  $V_0$ ,  $K_{T0}$ ,  $K'_{T0}$ ,  $\gamma_0$ ,  $q_0$ ,  $G_0$ ,  $G'_0$ ,  $\eta_{S0}$  and  $\theta_0$  for those phases for which thermochemical determinations of the high temperature entropy exist.

Here we focus on the determination of the parameters  $\mathcal{F}_0$ ,  $W_{\alpha\beta}$  and  $\theta_0$  for those phases for which experimental measurements of the high temperature entropy do not exist. The determination is based on the inversion of phase equilibria data. In order to communicate likely uncertainties in the individual parameters, parameter values are listed to significant precision in Tables A1–A3. Note however that because uncertainties in the parameters are correlated, higher precision is needed to reproduce our results, particularly at high pressure. Parameters at full precision are available from the authors on request.

In selecting experimental data to include in the inversion, we have followed the general strategy of Holland & Powell (1990) in selecting the minimal possible set of data that constrain the relevant parameters (Tables A4 and A5). This strategy makes it much easier to recognize *a posteriori* if systematic biases have crept into the global inversion, an important consideration especially at high pressure where many data sets are mutually inconsistent. Some of the considerations that have gone into choosing different experimental data sets include: sample characterization, demonstration of

Table A1. Properties of mantle species.

Phase	Species	Formula	$\mathcal{F}_0$ (kJ mol <sup>-1</sup> )	$V_0$ (cm <sup>3</sup> mol <sup>-1</sup> )	$K_{70}$ (GPa)	$K'_{70}$	$\theta_0$ (K)	$\gamma_0$	$q_0$	$G_0$ (GPa)	$G'_0$	$\eta_{80}$	Ref.
feldspar (plg)	Anorthite (an)	Ca [Al <sub>2</sub> Si <sub>2</sub> ] O <sub>8</sub>	-4015 (4)	100.61	84 (5)	4.0 (10)	752 (2)	0.39 (5)	1.0 (10)	40 (3)	1.1 (5)	1.6 (10)	1-6
feldspar	Albite (ab)	Na [Al Si <sub>3</sub> ] O <sub>8</sub>	-3719 (5)	100.45	60 (5)	4.0 (10)	716 (13)	0.57 (3)	1.0 (10)	36 (5)	1.4 (5)	1.0 (10)	1,6,7
spinel (sp)	Spinel (sp)	(Mg <sub>3</sub> Al)(Al <sub>2</sub> Mg)O <sub>16</sub>	-8668 (32)	159.05	197 (1)	5.7 (2)	843 (33)	1.02 (4)	2.7 (6)	108 (10)	0.4 (5)	2.7 (6)	1,8-10
spinel	Hercynite (hc)	(Fe <sub>3</sub> Al)(Al <sub>2</sub> Fe)O <sub>16</sub>	-7324 (35)	163.37	209 (2)	5.7 (10)	763 (32)	1.22 (7)	2.7 (10)	84 (13)	0.4 (5)	2.8 (10)	1,2,11
olivine (ol)	Forsterite (fo)	Mg <sub>2</sub> Si O <sub>4</sub>	-2055 (2)	43.60	128 (2)	4.2 (2)	809 (1)	0.99 (3)	2.1 (2)	82 (2)	1.5 (1)	2.3 (1)	1,10,12-14
olivine	Fayalite (fa)	Fe <sub>2</sub> Si O <sub>4</sub>	-1371 (1)	46.29	135 (2)	4.2 (10)	619 (2)	1.06 (7)	3.6 (10)	51 (2)	1.5 (1)	1.0 (6)	1,2,6,10,13,15,16
wadsleyite (wa)	Mg-Wadsleyite (mgwa)	Mg <sub>2</sub> Si O <sub>4</sub>	-2028 (2)	40.52	169 (3)	4.3 (2)	844 (7)	1.21 (9)	2.0 (10)	112 (2)	1.4 (2)	2.6 (4)	1,6,17-20
wadsleyite	Fe-Wadsleyite (fewa)	Fe <sub>2</sub> Si O <sub>4</sub>	-1365 (7)	42.80	169 (13)	4.3 (10)	665 (21)	1.21 (30)	2.0 (10)	72 (12)	1.4 (5)	1.0 (10)	17,21
ringwoodite (ri)	Mg-Ringwoodite (mgr)	Mg <sub>2</sub> Si O <sub>4</sub>	-2017 (2)	39.49	185 (2)	4.2 (10)	878 (8)	1.11 (10)	2.4 (4)	123 (2)	1.4 (1)	2.3 (5)	1,6,22-24
ringwoodite	Fe-Ringwoodite (fer)	Fe <sub>2</sub> Si O <sub>4</sub>	-1363 (2)	41.86	213 (7)	4.2 (10)	679 (8)	1.27 (23)	2.4 (10)	92 (10)	1.4 (5)	1.8 (10)	22,25,26
orthopyroxene	Enstatite (en)	Mg Mg Si <sub>2</sub> O <sub>6</sub>	-2913 (2)	62.68	107 (2)	7.0 (4)	812 (4)	0.78 (4)	3.4 (4)	77 (1)	1.5 (1)	2.5 (1)	1,27-32
(opx)													
orthopyroxene	Ferrosilite (fs)	Fe Fe Si <sub>2</sub> O <sub>6</sub>	-2226 (4)	65.94	101 (4)	7.0 (5)	674 (10)	0.72 (8)	3.4 (10)	52 (5)	1.5 (5)	1.1 (10)	1,2,27,33,34
orthopyroxene	Mg-Tschermaks (mgs)	Mg Al [Si Al] O <sub>6</sub>	-3003 (9)	59.14	107 (10)	7.0 (10)	784 (24)	0.78 (30)	3.4 (10)	97 (10)	1.5 (5)	2.5 (10)	35
orthopyroxene	Ortho-Diopside (odi)	Ca Mg Si <sub>2</sub> O <sub>6</sub>	-3016 (3)	68.05	107 (10)	7.0 (10)	745 (9)	0.78 (30)	3.4 (10)	60 (10)	1.5 (5)	1.4 (10)	36
clinopyroxene	Diopside (di)	Ca Mg Si <sub>2</sub> O <sub>6</sub>	-3030 (2)	66.04	112 (5)	5.2 (18)	782 (3)	0.96 (5)	1.5 (20)	67 (2)	1.4 (5)	1.6 (10)	1,2,6,13,37,38
(cpx)													
clinopyroxene	Hedenbergite (he)	Ca Fe Si <sub>2</sub> O <sub>6</sub>	-2677 (45)	67.87	119 (4)	5.2 (10)	702 (2)	0.94 (6)	1.5 (10)	61 (1)	1.2 (5)	1.6 (10)	1,6,13,16,39
clinopyroxene	Clinoenstatite (cen)	Mg Mg Si <sub>2</sub> O <sub>6</sub>	-2906 (3)	62.50	112 (10)	5.2 (10)	805 (10)	0.96 (30)	1.5 (10)	81 (10)	1.7 (5)	1.7 (10)	36
clinopyroxene	Ca-Tschermaks (cats)	Ca Al (Si Al)O <sub>6</sub>	-3120 (5)	63.57	112 (10)	5.2 (10)	804 (5)	0.78 (0)	1.5 (10)	76 (10)	1.6 (5)	2.0 (10)	40,41
clinopyroxene	Jadeite (jd)	Na Al Si <sub>2</sub> O <sub>6</sub>	-2855 (3)	60.51	142 (2)	5.2 (10)	821 (12)	0.90 (8)	0.4 (14)	85 (2)	1.4 (5)	2.2 (10)	1,6,42-44
HP-clinopyroxene	HP-Clinoenstatite (hpcen)	Mg <sub>2</sub> Si <sub>2</sub> O <sub>6</sub>	-2905 (3)	60.76	116 (1)	6.2 (3)	824 (7)	1.12 (5)	0.2 (5)	88 (1)	1.8 (1)	2.1 (5)	45
(hpcpx)													
HP-clinopyroxene	HP-Clinoferrosilite (hpcf)	Fe <sub>2</sub> Si <sub>2</sub> O <sub>6</sub>	-2222 (4)	63.85	116 (10)	6.2 (10)	692 (11)	1.12 (30)	0.2 (10)	71 (10)	1.8 (5)	0.8 (10)	46
Ca-perovskite	Ca-Perovskite (capv)	Ca Si O <sub>3</sub>	-1463 (8)	27.45	236 (4)	3.9 (2)	796 (44)	1.89 (7)	0.9 (16)	157 (12)	2.2 (5)	1.3 (10)	1,47-49
(cpv)													
akimotoite (ak)	Mg-Akimotoite (mgak)	Mg Si O <sub>3</sub>	-1410 (2)	26.35	211 (4)	5.6 (8)	934 (12)	1.19 (13)	2.3 (8)	132 (8)	1.6 (5)	2.8 (10)	1,2,6,50,51
akimotoite	Fe-Akimotoite (feak)	Fe Si O <sub>3</sub>	-1068 (21)	26.85	211 (10)	5.6 (10)	888 (120)	1.19 (30)	2.3 (10)	150 (10)	1.6 (5)	3.5 (10)	52
akimotoite	Corundum (co)	Al O <sub>3</sub>	-1582 (1)	25.58	253 (5)	4.3 (2)	933 (3)	1.32 (4)	1.3 (2)	163 (2)	1.6 (1)	2.8 (2)	1,6,10,13,53
garnet (gt,mj)	Pyrope (py)	Mg <sub>3</sub> Al Al Si <sub>3</sub> O <sub>12</sub>	-5936 (10)	113.08	170 (2)	4.1 (3)	823 (4)	1.01 (6)	1.4 (5)	94 (2)	1.4 (2)	1.0 (3)	1,13,54-56
garnet	Almandine (al)	Fe <sub>3</sub> Al Al Si <sub>3</sub> O <sub>12</sub>	-4935 (29)	115.43	174 (2)	4.9 (2)	741 (5)	1.06 (6)	1.4 (10)	96 (1)	1.4 (1)	2.1 (10)	1,13,55,57
garnet	Grossular (gr)	Ca <sub>3</sub> Al Al Si <sub>3</sub> O <sub>12</sub>	-6278 (11)	125.12	167 (1)	3.9 (2)	823 (2)	1.05 (6)	1.9 (2)	109 (4)	1.2 (1)	2.4 (1)	1,10,29,55,57,58
garnet	Mg-Majorite (mgmj)	Mg <sub>3</sub> Mg Si <sub>3</sub> O <sub>12</sub>	-5691 (10)	114.32	165 (3)	4.2 (3)	822 (4)	0.98 (7)	1.5 (5)	85 (2)	1.4 (2)	1.0 (3)	1,13,23,56,59,60
garnet	Jd-Majorite (jdmj)	(Na <sub>2</sub> Al)Al Si <sub>3</sub> O <sub>12</sub>	-5519 (14)	110.94	177 (7)	4.1 (10)	896 (18)	1.07 (30)	1.4 (10)	125 (4)	1.4 (5)	3.3 (10)	61
quartz (qtz)	Quartz (qtz)	Si O <sub>2</sub>	-859 (1)	23.67	50 (1)	4.3 (1)	816 (31)	0.00 (5)	1.0 (10)	45 (1)	1.0 (1)	2.4 (10)	1,6,62-64
coesite (coes)	Coesite (coes)	Si O <sub>2</sub>	-855 (1)	20.66	114 (1)	4.0 (10)	857 (9)	0.39 (5)	1.0 (10)	62 (1)	1.2 (5)	2.4 (10)	1,6,65
stishovite (st)	Stishovite (st)	Si O <sub>2</sub>	-819 (1)	14.02	314 (8)	3.8 (1)	1108 (13)	1.37 (17)	2.8 (22)	220 (12)	1.9 (1)	4.6 (10)	1,6,66-68
seifertite (seif)	Seifertite (seif)	Si O <sub>2</sub>	-794 (2)	13.67	328 (2)	4.0 (1)	1141 (16)	1.37 (30)	2.8 (10)	227 (2)	1.8 (1)	5.0 (10)	36,67
perovskite (pv)	Mg-Perovskite (mgpv)	Mg Si O <sub>3</sub>	-1368 (1)	24.45	251 (3)	4.1 (1)	905 (5)	1.57 (5)	1.1 (3)	173 (2)	1.7 (0)	2.6 (3)	1,69-74
perovskite	Fe-Perovskite (fepv)	Fe Si O <sub>3</sub>	-1041 (6)	25.49	272 (40)	4.1 (10)	871 (26)	1.57 (30)	1.1 (10)	133 (40)	1.4 (0)	2.3 (10)	52,75,76
perovskite	Rh <sub>2</sub> O <sub>3</sub> -II (rh2o3)	Al O <sub>3</sub>	-1534 (2)	24.94	258 (10)	4.1 (5)	886 (7)	1.57 (30)	1.1 (10)	171 (10)	1.5 (1)	2.5 (5)	77-79
post-perovskite	Mg-Post-Perovskite (mppv)	Mg Si O <sub>3</sub>	-1348 (3)	24.42	231 (1)	4.0 (1)	855 (7)	1.89 (3)	1.1 (1)	150 (4)	2.0 (1)	1.2 (2)	80-82
(ppv)													
post-perovskite	Fe-Post-Perovskite (fppv)	Fe Si O <sub>3</sub>	-982 (21)	25.46	231 (10)	4.0 (10)	782 (52)	1.89 (30)	1.1 (10)	129 (5)	1.4 (1)	1.4 (10)	83,84

Table A1. (Continued.)

Phase	Species	Formula	$\mathcal{F}_0$ (kJ mol <sup>-1</sup> )	$V_0$ (cm <sup>3</sup> mol <sup>-1</sup> )	$K_{T0}$ (GPa)	$K'_{T0}$	$\theta_0$ (K)	$\gamma_0$	$q_0$	$G_0$ (GPa)	$G'_0$	$\eta_{50}$	Ref.
post-perovskite	Al-Post-Perovskite (appv)	Al Al O <sub>3</sub>	-1378 (4)	23.85	249 (20)	4.0 (1)	762 (9)	1.65 (2)	1.1 (10)	92 (10)	1.8 (1)	2.8 (2)	79,85,86
magnesiowüstite	Periclase (pc)	Mg O	-569	11.24	161 (3)	3.8 (2)	767 (9)	1.36 (5)	1.7 (2)	131 (1)	2.1 (1)	2.8 (2)	1,9,10,13,54,87,88
magnesiowüstite	Wüstite (wu)	Fe O	-242 (1)	12.26	179 (1)	4.9 (2)	454 (21)	1.53 (13)	1.7 (10)	59 (1)	1.4 (1)	-0.1 (10)	6,13,89-92
Ca-ferrite (cf)	Mg-Ca-Ferrite (mgcf)	Mg Al Al O <sub>4</sub>	-2122 (4)	36.18	211 (1)	4.1 (1)	838 (16)	1.31 (30)	1.0 (10)	130 (1)	1.8 (1)	2.1 (10)	93,94
Ca-ferrite	Fe-Ca-Ferrite (fcf)	Fe Al Al O <sub>4</sub>	-1790 (25)	37.26	211 (10)	4.1 (10)	804 (69)	1.31 (30)	1.0 (10)	152 (10)	1.8 (5)	3.0 (10)	36
Ca-ferrite	Na-Ca-Ferrite (nacf)	Na Al Si O <sub>4</sub>	-1851 (11)	36.27	158 (1)	4.3 (1)	812 (51)	1.17 (30)	1.0 (10)	121 (1)	2.1 (1)	1.6 (10)	94,95
kyanite (ky)	Kyanite (ky)	Al <sub>2</sub> Si O <sub>5</sub>	-2446 (4)	44.23	160 (1)	4.0 (0)	943 (7)	0.93 (7)	1.0 (10)	121 (10)	1.7 (5)	3.0 (10)	1,96-98
nepheline (neph)	Nepheline (neph)	Na Al Si <sub>3</sub> O <sub>8</sub>	-1993 (3)	54.67	53 (1)	4.0 (10)	701 (13)	0.69 (3)	1.0 (10)	31 (1)	1.3 (5)	0.6 (10)	2,13,100,101

1. Smyth & McCormick (1995) 3. Bass (1995) 4. Krupka *et al.* (1999) 5. Robie *et al.* (1979) 6. Fei (1995) 7. Brown *et al.* (2006) 8. Yoneda (1990) 9. Fiquet *et al.* (1999) 10. Anderson & Isaak (1995) 11. Harrison *et al.* (1998) 12. Zha *et al.* (1996) 13. Robie & Hemingway (1995) 14. Bouchard *et al.* (1995) 15. Zha *et al.* (1998) 16. Knittle (1995) 17. Sinogeikin *et al.* (1998) 18. Zha *et al.* (1997) 19. Fei *et al.* (1992) 20. Li *et al.* (2001) 21. Hazen *et al.* (2000) 22. Sinogeikin *et al.* (2003) 23. Higo *et al.* (2008) 24. Sinogeikin *et al.* (2001) 25. O'Neill *et al.* (1993) 26. Mao *et al.* (1993) 27. Jackson *et al.* (1999) 28. Flesch *et al.* (1999) 29. Thieblot *et al.* (1999) 30. Krupka *et al.* (1985) 31. Jackson *et al.* (2003) 32. Jackson *et al.* (2007) 33. Hugh-Jones & Angel (1997) 34. Hugh-Jones (1997) 35. Danekwerth & Newton (1978) 36. This work 37. Levien & Prewitt (1981) 38. Zha *et al.* (1998) 39. Kandelin & Weidner (1988b) 40. Haselton *et al.* (1984) 41. Ezel *et al.* (2007) 42. Kandelin & Weidner (1988a) 43. Hemingway *et al.* (1998) 44. Zha *et al.* (1997) 45. Kung *et al.* (2005) 46. Hugh-Jones *et al.* (1996) 47. Shim *et al.* (2000) 48. Wang *et al.* (1996) 49. Karki & Crain (1998) 50. Wang *et al.* (2004) 51. Dasilva *et al.* (1999) 52. Jeanloz & Thompson (1983) 53. Gieske & Bursch (1968) 54. Sinogeikin & Bass (2000) 55. Thieblot *et al.* (1998) 56. Sinogeikin & Bass (2002b) 57. Jiang *et al.* (2004) 58. Haselton & Westrum (1980) 59. Sinogeikin & Bass (2002a) 60. Wang *et al.* (1998) 61. Reichmann *et al.* (2002) 62. Ohno *et al.* (2006) 63. Kimizuka *et al.* (1982) 65. Weidner & Carleton (1977) 66. Weidner *et al.* (1982) 67. Karki *et al.* (1997b) 68. Liu *et al.* (1999) 69. Sinogeikin *et al.* (2004) 70. Murakami *et al.* (2004) 71. Wentzcovitch *et al.* (2004a) 72. Shim & Duffy (2000) 73. Fiquet *et al.* (2000) 74. Katsura *et al.* (2009) 75. Kiefer *et al.* (2002) 76. Stackhouse *et al.* (2006a) 77. Oganov & Ono (2005) 78. Duan *et al.* (1999) 79. Stackhouse *et al.* (2005a) 80. Guignot *et al.* (2007) 81. Stackhouse *et al.* (2005b) 82. Tsuchiya *et al.* (2004) 83. Shieh *et al.* (2006) 84. Stackhouse *et al.* (2006b) 85. Ono *et al.* (2006) 86. Caracas & Cohen (2005) 87. Jackson & Niesler (1982) 88. Murakami *et al.* (2009) 89. Jacobsen *et al.* (2002) 90. Jackson *et al.* (1990) 91. Marquardt *et al.* (2009) 92. Stolen *et al.* (1996) 93. Funamori *et al.* (1998) 94. Mookherjee (2010) 95. Yamada *et al.* (1983) 96. Comodi *et al.* (1991) 98. Gatta *et al.* (2006) 99. Hovis *et al.* (2009) 100. Hovis *et al.* (2003).

Table A2. Interaction parameters.

Phase	Species 1	Species 2	$W_{12}$ (kJ mol <sup>-1</sup> )	Ref. <sup>a</sup>
plg	an	ab	26 (2)	Benisek <i>et al.</i> (2003)
ol	fo	fa	7.6 (22)	
wa	mgwa	fewa	16.5 (22)	Frost (2003a)
ri	mgri	feri	9.1 (22)	
fp	pe	wu	13 (1)	
sp	sp	hc	5 (5)	Holland <i>et al.</i> (1979)
cpx	di	cen	24.7 (20)	
cpx	di	cats	26 (4)	Benisek <i>et al.</i> (2007)
cpx	di	jd	24.3 (20)	
cpx	cen	he	24.7 (20)	Holland (1983)
cpx	cen	cats	60.6 (88)	
cpx	cats	jd	10 (4)	Cohen (1986)
opx	en	odi	32.1 (10)	
opx	mgts	odi	48 (11)	Haselton & Newton (1980)
gt	py	gr	30 (5)	
gt	py	mgmj	21.3 (65)	Panero <i>et al.</i> (2006)
gt	gr	mgmj	58 (17)	
ak	mgak	co	66 (10)	Tsuchiya & Tsuchiya (2008)
pv	mgpv	rh2o3	116 (10)	
ppv	mppv	appv	60 (10)	Tsuchiya & Tsuchiya (2008)

Note: Size parameters  $d_\alpha = 1$  for all species except  $d_{cats} = 3.5$  and  $d_{rh2o3} = 0.39$ .

<sup>a</sup>From our global inversion of phase equilibria unless otherwise noted.

<sup>b</sup>Assumed to be the same as  $W_{di-cen}$ .

Table A3. Landau parameters

Species	$T_{C0}$ (K)	$V_D$ (cm <sup>3</sup> mol <sup>-1</sup> )	$S_D$ (J mol <sup>-1</sup> K <sup>-1</sup> )	Ref. <sup>a</sup>
qtz	847	1.222	5.164	Mirwald & Massone (1980)
st	-4250	0.001 <sup>b</sup>	0.012	Andrault <i>et al.</i> (1998) and Ono <i>et al.</i> (2002)

<sup>a</sup>Sources of data in addition to those cited in Table A1.

<sup>b</sup>Values of  $V_D$  and  $S_D$  chosen to be vanishingly small.

equilibrium, type of experiment: synthesis vs. bracketing, homogeneity of pressure and temperature, and measurement of pressure and temperature. We exclude experimental observations that violate the phase rule, that is, synthesis experiments that produce two assemblages when the phase rule predicts that only one can be stable in equilibrium, except in those cases where the growth of one assemblage at the expense of the other is carefully monitored. We also exclude experimental data in which the charge experiences large temperature gradients. For example, in the experiments of Gasparik (1990a) a temperature gradient of several hundred degrees stabilized different phase assemblages at different ends of the capsule. In such a situation, equilibrium is very difficult to demonstrate. As a further example of many of our considerations, the measurements of Fei *et al.* (2004) of the perovskite forming reaction in Mg<sub>2</sub>SiO<sub>4</sub> were preferred to those of Ito & Takahashi (1989) because the former experiment featured: (1) better pressure calibration based on *in situ* X-ray diffraction of multiple pressure standards as opposed to room temperature load-pressure correlation with no heating correction; (2) longer run times of greater than one hour, as opposed to as little as 20 min in the latter experiment and (3) more thorough analysis of quenched products including probes of much higher

**Table A4.** Summary of phase equilibria data: stability.

Species	<i>N</i>	<i>P</i> <sub>min</sub> GPa	<i>P</i> <sub>max</sub> GPa	<i>T</i> <sub>min</sub> K	<i>T</i> <sub>max</sub> K	Ref.
fo	4	12.00	13.90	1063	1876	Morishima <i>et al.</i> (1994)
mgwa	18	14.88	18.08	1023	1773	Suzuki <i>et al.</i> (2000)
		12.10	14.30	1025	1624	Morishima <i>et al.</i> (1994)
		21.56	22.82	2173	2173	Fei <i>et al.</i> (2004)
mgri	16	14.98	19.50	923	1273	Suzuki <i>et al.</i> (2000)
		22.13	23.43	1673	2173	Fei <i>et al.</i> (2004)
mgpv+pe	6	22.82	25.56	1673	2173	Fei <i>et al.</i> (2004)
en	10	0.00	0.00	1360	1360	Yang & Ghose (1995)
		0.83	0.83	1823	1823	Boyd <i>et al.</i> (1964)
		7.70	10.30	1273	1973	Pacalo & Gasparik (1990)
		9.70	10.60	2333	2353	Presnall <i>et al.</i> (1998)
mgc2	15	8.20	14.20	1223	1973	Pacalo & Gasparik (1990)
		14.50	15.50	1273	1673	Ito & Navrotsky (1985)
		11.80	14.90	2373	2463	Presnall <i>et al.</i> (1998)
mgmj	2	16.50	16.50	2473	2473	Presnall <i>et al.</i> (1998)
		21.20	21.20	2273	2273	Hirose <i>et al.</i> (2001b)
mgil	3	20.00	20.00	1273	1873	Ito & Navrotsky (1985)
		22.13	22.13	1873	1873	Fei <i>et al.</i> (2004)
mgpv	22	21.56	24.56	1673	2173	Fei <i>et al.</i> (2004)
		21.54	21.54	2273	2273	Hirose <i>et al.</i> (2001b)
		119.00	149.30	2170	4200	Tateno <i>et al.</i> (2009)
		92.30	126.10	1510	2360	Hirose <i>et al.</i> (2006)
mgwa+st	5	16.00	18.00	1273	1873	Ito & Navrotsky (1985)
mgri+st	2	19.10	19.10	1373	1673	Ito & Navrotsky (1985)
fs	8	5.00	7.00	1173	1578	Woodland & Angel (1997)
		1.35	1.53	1173	1323	Bohlen <i>et al.</i> (1980)
fec2	10	5.50	7.50	1173	1568	Woodland & Angel (1997)
		8.30	9.40	1063	1483	Akimoto & Syono (1970)
feri+st	3	9.40	9.80	1063	1423	Akimoto & Syono (1970)
wu+st	4	17.40	19.80	1473	1873	Katsura <i>et al.</i> (1998)
fa	5	4.18	5.56	1073	1473	Yagi <i>et al.</i> (1987)
feri	18	4.32	6.28	773	1473	Yagi <i>et al.</i> (1987)
		14.80	17.20	1273	1673	Katsura <i>et al.</i> (1998)
di	8	0.00	0.00	1665	1665	Boyd & England (1963)
		14.00	14.00	2400	2400	Gasparik (1996)
		16.50	17.50	1273	2073	Akaogi <i>et al.</i> (2004)
capv+mgwa+st	4	17.50	19.00	1273	1673	Akaogi <i>et al.</i> (2004)
capv+mgri+st	4	19.00	20.50	1473	1673	Akaogi <i>et al.</i> (2004)
capv+mgil	6	20.50	22.50	1473	2073	Akaogi <i>et al.</i> (2004)
capv+mgpv	3	22.30	23.00	1873	2073	Akaogi <i>et al.</i> (2004)
capv+co	2	24.27	26.16	1673	1873	Takafuji <i>et al.</i> (2002)
fo+fa	6	12.62	14.68	1600	1900	Katsura <i>et al.</i> (2004)
mgwa+fewa	6	12.62	14.68	1600	1900	Katsura <i>et al.</i> (2004)
st	27	101.00	127.00	800	3000	Murakami <i>et al.</i> (2003)
		7.71	11.36	800	1803	Zhang <i>et al.</i> (1996)
seif	4	124.00	151.00	2040	2420	Murakami <i>et al.</i> (2003)
mppv	8	136.10	171.00	1640	4380	Tateno <i>et al.</i> (2009)
co	2	72.00	89.00	1	4000	Tsuchiya <i>et al.</i> (2005)
rh2o3	4	72.00	150.00	1	4000	Tsuchiya <i>et al.</i> (2005)
appv	2	93.00	150.00	1	4000	Tsuchiya <i>et al.</i> (2005)
pe+co	4	20.00	27.00	1473	1873	Akaogi <i>et al.</i> (1999)
		45.00	45.00	1	1	Ono <i>et al.</i> (2008)
mgcf	4	27.00	27.00	1873	2173	Akaogi <i>et al.</i> (1999)
		45.00	45.00	1	1	Ono <i>et al.</i> (2008)
jd+st	3	22.00	22.00	1073	1473	Yagi <i>et al.</i> (1994)
nacf+st	2	23.00	23.00	1273	1473	Yagi <i>et al.</i> (1994)
ab	12	1.60	3.30	873	1473	Holland (1980)
jd+qtz	1	1.65	1.65	873	873	Holland (1980)
coes	18	7.91	8.62	1258	1507	Zhang <i>et al.</i> (1996)
		2.65	3.77	875	1911	Mirwald & Massone (1980)
qtz	8	2.60	3.61	873	1788	Mirwald & Massone (1980)
cats	3	1.72	2.85	1573	1773	Gasparik (1984a)
gr+co	3	1.77	2.88	1573	1773	Gasparik (1984a)

**Table A4.** (Continued.)

Species	<i>N</i>	<i>P</i> <sub>min</sub> GPa	<i>P</i> <sub>max</sub> GPa	<i>T</i> <sub>min</sub> K	<i>T</i> <sub>max</sub> K	Ref.
fa+qtz	4	1.10	1.40	1073	1273	Bohlen <i>et al.</i> (1980)
ky	4	0.75	0.82	1073	1073	Harlov & Milke (2002)
qtz+co	2	0.70	0.75	1073	1073	Harlov & Milke (2002)
gr+ky+qtz	24	2.20	3.10	1373	1673	Goldsmith (1980)
an	1	3.00	3.00	1673	1673	Goldsmith (1980)
di+cats	1	3.24	3.24	1573	1573	Gasparik (1984a)
py+gr	1	3.30	3.30	1573	1573	Gasparik (1984a)
jd	1	2.38	2.38	1473	1473	Gasparik (1985)
neph+ab	1	2.33	2.33	1473	1473	Gasparik (1985)

**Table A5.** Summary of phase equilibrium data: reactions.

Species	<i>N</i>	<i>P</i> <sub>min</sub> GPa	<i>P</i> <sub>max</sub> GPa	<i>T</i> <sub>min</sub> K	<i>T</i> <sub>max</sub> K	Ref.
py+capv=gr+mgmj	1	19.90	19.90	1873	1873	Saikia <i>et al.</i> (2008)
mgc2=py+mgmj	1	12.50	12.50	1923	1923	Gasparik (1989)
en+odi=di+cen	14	3.00	3.00	1173	1773	Carlson & Lindsley (1988)
he+en=di+fs	1	1.50	1.50	1263	1263	Lindsley (1983)
fo+wu=fa+pe	15	6.00	6.00	1673	1673	Frost (2003b)
mgwa+wu=fewa+pe	3	15.00	15.00	1773	1773	Fei <i>et al.</i> (1991)
mgwa+wu=fewa+pe	15	13.00	14.50	1673	1673	Frost (2003b)
fo+al=fa+py	10	0.91	0.91	1273	1273	Hackler & Wood (1989)
mgri+wu=feri+pe	51	11.00	23.50	1273	1873	Frost <i>et al.</i> (2001)
mgpv+wu=fepv+pe	10	26.00	26.00	1573	1873	Martinez <i>et al.</i> (1997)
		36.00	107.70	1760	2170	Sinmyo <i>et al.</i> (2008)
mgil+fepv=feil+mgpv	2	25.50	25.50	1373	1373	Ito & Yamada (1982)
		24.00	24.00	2073	2073	Ohtani <i>et al.</i> (1991)
fo+hc=fa+sp	13	0.00	0.00	1573	1573	Jamieson & Roeder (1984)
mgts+en=co+py	1	1.65	1.65	1123	1123	Gasparik & Newton (1984)
mgts+en=py	23	2.07	4.01	1173	1773	Perkins <i>et al.</i> (1981)
en+sp=mgts+fo	6	0.99	2.56	1573	1773	Gasparik & Newton (1984)
mgts+di+cen=cats+en+odi	6	2.70	2.70	1773	1773	Klemme & O'Neill (2000)
		2.50	2.50	1173	1173	Perkins & Newton (1980)
gr+cen=py+di+cats	1	2.50	2.50	1173	1173	Perkins & Newton (1980)
mppv+fepv=fppv+mgpv	1	120.00	120.00	1750	1750	Hirose <i>et al.</i> (2008)
jd+di=qtz+ab	21	0.85	1.60	873	873	Holland (1983)
jd=jdmj+mgmj	2	20.70	20.70	1823	1923	Gasparik (1992)
fepv+mgcf=mgpv+fecf	2	60.00	60.00	2000	2400	Hirose <i>et al.</i> (2005)

spatial resolution (100×) and Raman spectroscopy in addition to X-ray diffraction and electron microprobe.

We addressed errors in pressure calibration by correcting older values when possible. Substantial progress over the last few years has revealed that many of the pressure standards used in the past are inaccurate. For example, the equation of state of gold of Anderson *et al.* (1989) is inaccurate because it does not accurately represent all available experimental data on the gold equation of state, particularly shock wave data. So, for example, the pressures reported by Hirose *et al.* (2001a) and Hirose *et al.* (2001b) using Anderson's gold scale have been redetermined based on the lattice parameters of gold reported in these studies and the most recent analysis of the gold equation of state (Fei *et al.* 2004).

We determine the values of the parameters by minimizing the misfit

$$\chi^2 = \sum_i^{\text{stability}} \frac{[\mathcal{G}(P_i, T_i, \vec{n}_i) - \mathcal{G}(P_i, T_i, \vec{n}_i^{\min})]^2}{\sigma_i^2} + \sum_i^{\text{reactions}} \frac{[\Delta\mu_i(P_i, T_i, \vec{n}_i)]^2}{\sigma_i^2}, \quad (\text{A1})$$

where the index *i* runs over the set of experimental phase equilibrium observations included in the fit, *P<sub>i</sub>*, *T<sub>i</sub>*, *n<sub>i</sub>* are the experimental pressure, temperature, and assemblage observed, *G* is the Gibbs free energy computed from our model, and *σ<sub>i</sub>* are the associated uncertainties. The quantity *n<sub>i</sub><sup>min</sup>* represents the phase assemblage with the same bulk composition as *n<sub>i</sub>* and with the minimum Gibbs free energy at *P<sub>i</sub>* and *T<sub>i</sub>* as computed from our model.

The stability term accounts for equilibria with variance *f* = *c* − *p* + 2 < 2, where *c* is the number of linearly independent components and *p* is the number of phases, for example *fo* = *mgwa* (*f* = 1). We have chosen to distinguish the stability term from the reaction term for two reasons: (1) Less than divariant coexistence is in principle unobservable experimentally. By definition no more than one of the two assemblages forming the equilibrium reaction can be present in equilibrium at a single *P*, *T*, except in the improbable case of experimentally hitting upon the phase boundary exactly. Observations of coexistence are of course common, but this is a phenomenon of either disequilibrium made possible by finite reaction rates, or inhomogeneity in sample conditions (*P*, *T*, or *b*). (2) At high pressure (*P* > 10 GPa) experimental brackets are rare and the position of the equilibrium boundary is often poorly

determined. In such cases, the fundamental experimental observable is that one assemblage is more stable than all others and this is the physics captured by the first term in eq. (A1).

To evaluate the stability term, we compare the computed Gibbs free energy of the experimentally observed assemblage to that of all other assemblages of the same composition. If no other assemblage has lower Gibbs free energy, then  $\vec{n}_i = \vec{n}_i^{\min}$  and the term vanishes. So for example, for an experimental observation of the stability of *mgpv*, we compare the Gibbs free energy of *mgpv* to that of: (1) all other MgO–SiO<sub>2</sub> metasilicate species (*en*, *cen*, *hpcen*, *mgmj*, *mgak*, *mppv*) (2) all possible combinations of orthosilicate (*fo*, *mgwa*, *mgri*) and free silica phases (*qtz*, *coes*, *st*, *seif*) and (3) all possible combinations of Mg (*pe*) and Si (*qtz*, *coes*, *st*, *seif*) oxides. The importance of such comparisons is illustrated by the MgO–SiO<sub>2</sub> system in the vicinity of the perovskite forming reactions where combinations of metasilicates, orthosilicates and silica, and oxide assemblages all have very similar free energies with a topologically rich network of reactions between them that are only sparsely constrained by experimental observations.

The reaction term involves experimentally observed assemblages that have greater than unit variance and which are permitted by the Gibbs phase rule. So for example, the Gibbs free energy of *mgts* is constrained by experimental observations of the composition of aluminous *opx* in coexistence with pyrope ( $f = 2$ )

$$\text{mgts}(\text{opx}) + \text{en}(\text{opx}) = \text{py}, \quad (\text{A2})$$

where the parentheses remind that the species *en* and *mgts* exist in solid solution, so that in equilibrium the quantity

$$\Delta\mu(P, T) = \mu_{\text{py}}(P, T) - \mu_{\text{mgts}}(P, T, x) - \mu_{\text{en}}(P, T, x) = 0 \quad (\text{A3})$$

vanishes, where  $x$  is the *mgts* mole fraction in the orthopyroxene. We compute the contribution to  $\chi^2$  by evaluating the quantity  $\Delta\mu(P, T)$  in our model at the experimentally observed values of  $P, T, x$ .

We treat the uncertainties in a very simple way. We assign a universal and nominal value of  $\sigma = 1 \text{ kJ mol}^{-1} \text{ atom}^{-1}$  to all stability observations. As argued above (eq. 40), this corresponds to an error in the transition pressure of 1 GPa for a volume of transition or  $1 \text{ cm}^3 \text{ mol}^{-1} \text{ atom}^{-1}$ . Such an error in pressure is probably a reasonable estimate of the accuracy in high pressure phase equilibria experiments; the accuracy in pressure in low pressure experiments is probably better. Since uncertainties in Gibbs free energy and transition pressure are related via  $\delta P = \delta G / \Delta V$ , our approach, in which we assume that the uncertainty in the Gibbs free energy is the same for all phase transformations, implies a narrower uncertainty in the pressure for those transitions with large  $\Delta V$ . This seems reasonable as such transitions will have a larger thermodynamic driving force and will require less overpressure to overcome kinetic hindrances. Moreover,  $\Delta V$  on average tends to be larger at low pressure than at high pressure, so assuming  $\sigma = \text{constant}$  does not bias against low pressure data. We assign  $\sigma = 3 \text{ kJ mol}^{-1} \text{ atom}^{-1}$  to all reactions, where the greater uncertainty as compared with that assumed for stability observations accounts for uncertainties in phase compositions in addition to those in  $P$ .

Phase equilibria constrain only differences in Gibbs free energy and must be supplemented by independent thermochemical measurements to constrain the absolute values of the  $\mathcal{F}_0$  parameters. These additional constraints must include at least one species representative of each component in the system of interest (Berman 1988). We have chosen to use as additional constraints the experimental thermochemical values of the Gibbs free energy at

$$T_G = 1000 \text{ K}$$

$$\mathcal{G}(0, T_G) = \Delta_f \mathcal{G}^0 + \mathcal{G}_T^0(0, T_G) - \mathcal{G}_T^0(0, T_0) \quad (\text{A4})$$

for *fo*, *fa*, *di*, *jd*, *co*, *qt* and *pe*. The inversion reproduces the thermochemical values of these seven species to within  $0.06 \text{ kJ mol}^{-1}$  rms. The inclusion of *fo* is in principle redundant with the inclusion of *pe* and *qtz* in this set. However, it was found to be necessary to constrain the Gibbs free energy of *fo* independently in order to accurately reproduce the properties of the CMAS *plg-sp-gt* peridotite system.

## APPENDIX B: COMPUTATIONAL ALGORITHM

Minimization of the Gibbs free energy is performed over the null space of the linear problem

$$\begin{pmatrix} r \\ r_a \end{pmatrix} \begin{pmatrix} n \end{pmatrix} = \begin{pmatrix} b \\ 0 \end{pmatrix}, \quad (\text{B1})$$

where the augmented stoichiometric coefficient matrix  $\hat{r}$  has dimension  $\hat{c} \times s$ , where  $\hat{c} = c + a$  and  $a$  is the number of absent species, and is divided into two submatrices,  $r$  containing the stoichiometric coefficients, and  $r_a$  which contains, for each absent species, one row with one non-zero element corresponding to that species. The augmented bulk composition vector  $\hat{b}$  has dimension  $\hat{c}$  and is divided into two portions,  $b$  containing the definition of the bulk composition, and the other part consisting of null entries for each absent species. Amounts of all species not present in the initial guess are set to zero in this way. Species are also removed as, during the course of the minimization, their amount falls below a small value  $n_i \leq \epsilon$  where the value of  $\epsilon$  depends on machine precision.

We perform singular value decomposition to identify the vectors that span the null space, which has dimensions

$$l = s - \hat{c}. \quad (\text{B2})$$

Any matrix may be written in terms of its singular value decomposition (SVD)

$$\hat{r} = U W V^T, \quad (\text{B3})$$

where  $U$  and  $V$  are orthogonal  $\hat{c} \times s$  matrices, and  $W$  is a diagonal  $s \times s$  matrix with  $l$  zero diagonal elements. The matrix

$$V = (V^0 | V^1) \quad (\text{B4})$$

contains the  $l$  vectors that span the null space in the columns  $V^1$ . The species vector is written

$$n_i = n_i^0 + V_{ij}^1 n_j^1, \quad (\text{B5})$$

where

$$n^0 = V W^{-1} U^T b \quad (\text{B6})$$

is a solution to eq. (B1) and  $n^1$  is a vector of length  $l$ . At equilibrium

$$\forall i : \frac{\partial \mathcal{G}}{\partial n_i^1} = 0 \quad (\text{B7})$$

which corresponds physically to the homogeneity of the chemical potential across the coexisting phases. The rms magnitude of the

left-hand side of eq. (B7) provides a measure of the quality of the numerical solution.

The minimization of  $\mathcal{G}$  now proceeds over the elements of  $n^1$ , for which we use either the conjugate gradient or quasi-Newton method. At the heart of either method are line minimizations along

$$n_i^{1,(k+1)} = n_i^{1,(k)} + \lambda^{(k)} V_{ij}^{-1} \chi_j, \quad (\text{B8})$$

where  $\mathcal{G}$  is to be minimized with respect to  $\lambda$  along a particular direction in the null space  $\chi_j$  and the parenthetical superscripts refer to the iteration number. The search direction  $\chi_j$  may be initially chosen arbitrarily, and is then updated according to information about the Hessian built up during the course of the minimization (Press *et al.* 1992). In detail, we have found that a combination of conjugate gradient and quasi-Newton methods is useful. As expected, the conjugate gradient scheme tends to be more stable for poor initial guesses, whereas the quasi-Newton method converges more rapidly once a solution near to the minimum has been found. Initial values of  $n_i^1$ , and values of  $\lambda$  that satisfy the non-negativity constraints are readily identified via the introduction of slack variables and linear programming (Press *et al.* 1992).

Once the minimum in  $\mathcal{G}$  is found, the least abundant species that satisfies  $n_i < \epsilon$  is removed. An additional constraint is added to the augmented linear problem (eq. B1), the singular value decomposition of the new matrix is performed and  $n^0$  recomputed (eq. B6). The new value of  $n^1$  is then found by solving

$$V^{1T}(n - n^0) = V^{1T}V^1n^1. \quad (\text{B9})$$

The Gibbs free energy is minimized again and if trace species remain, these are removed one at a time until all present species satisfy  $n_i > \epsilon$ .

We test for phase addition based on the chemical affinity

$$A_\phi = \min \left[ \sum_i^{s_\phi} x_i (\mu_i - r_{ij} \epsilon_j) \right], \quad (\text{B10})$$

where the sum is over the  $s_\phi$  species in phase  $\phi$  (all of which are absent), the notation  $\min []$  indicates the minimum value, and the component chemical potentials  $\epsilon_j$  are given by

$$r'_{ij} \epsilon_j = \mu'_i, \quad (\text{B11})$$

where the primes indicate that only species that are present are included. The phase with the lowest (most favourable) value of  $A_\phi$  per atom is added by removing the constraints on its species, recomputing  $V^1$  and  $n^0$  and finding the new  $n^1$  by solving

$$D\Delta = DV^1n^1, \quad (\text{B12})$$

where  $D$  is a matrix of dimension  $s \times s_\phi$  and contains non-zero elements corresponding only to the species of the phase to be added,  $\Delta_i = \alpha x_i$  is a vector of length  $s_\phi$  containing the amounts of the species of phase  $\phi$  to be added, and  $\alpha$  is small compared with the amounts of the present phases, but large compared with  $\epsilon$ .

As an example, consider a system of olivine and wadsleyite, with four species (Mg- and Fe-end members of each phase), and two components ( $\text{Mg}_2\text{SiO}_4$ ,  $\text{Fe}_2\text{SiO}_4$ ) (Fig. B1). The stoichiometric coefficient matrix is

$$r_{ij} = \begin{pmatrix} 2 & 0 & 2 & 0 \\ 0 & 2 & 0 & 2 \end{pmatrix}. \quad (\text{B13})$$

We set the composition to 0.9  $\text{Mg}_2\text{SiO}_4$ , 0.1  $\text{Fe}_2\text{SiO}_4$  and the initial guess to be olivine only with wadsleyite absent. At 13 GPa and 1500 K, the code finds that the chemical affinity of wadsleyite is

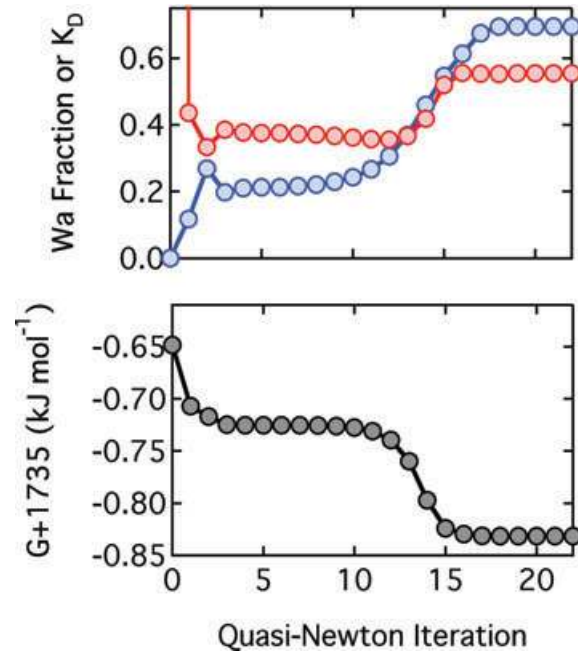


**Figure B1.** Top: evolution of (blue)  $wa$  fraction and (red) partition coefficient  $K = n_{fa}n_{mgwa}/n_{fo}n_{fewa}$ . Bottom: the Gibbs free energy with quasi-Newton iterations, for the example describe in the text, in which  $ol$  is adopted as the initial guess to the phase equilibria at conditions within the  $ol$ - $wa$  coexistence loop.

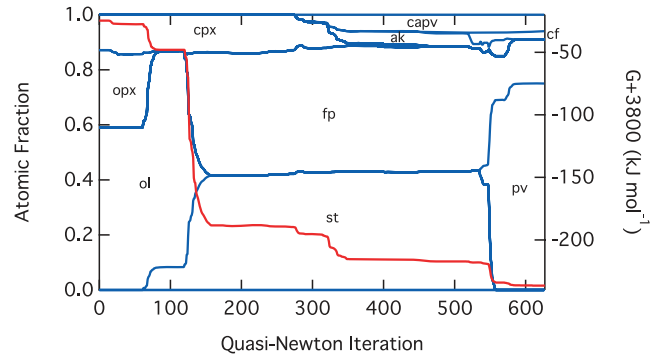


**Figure B2.** Evolution of (blue, left-hand axis) phase fractions and (red, right-hand axis) the Gibbs free energy with quasi-Newton iterations for the example describe in the text for which  $plg+opx+cpx+ol$  is adopted as the initial guess to the phase equilibria at lower mantle conditions.

$-0.218 \text{ kJ mol}^{-1}$  and adds wadsleyite with a composition  $X_{\text{Fe}} = 0.21$ . Singular value decomposition finds that the null space is spanned by the vectors corresponding to the reactions



By searching over the null space, the code rapidly finds the minimum value of the Gibbs free energy, which lies near the mid-point of the olivine-wadsleyite coexistence field.

Another example shows that the initial guess at the phases present need not be accurate (Fig. B2). As an extreme case, we assume a plagioclase peridotite assemblage ( $plg+opx+cpx+ol$ ) as the initial guess for the stable phase assemblage at 30 GPa and 1600 K. Typically one would initiate the calculation with a better guess based on one's knowledge of mantle phase equilibria, and indeed,

the code may be initiated with any initial guess that spans the bulk composition. On the other hand, the initial guess is not always obvious *a priori*, and this particular example has the advantage of exercising our algorithm for phase addition and subtraction to the full, and testing its robustness. Our routine successfully finds the global minimum of the Gibbs free energy, identical to that found with a more accurate initial guess. We have found that our strategy, in which  $\mathcal{G}$  is fully minimized after each removal of a single trace species, and each addition of a single phase is preferable to multiple additions and subtractions. Indeed, we find that if all phases with favourable chemical affinity are added at once, two problems develop. The first is that the addition of many species often causes violations of the phase rule. The second is that cycling of phase addition may become necessary, in which a phase previously added, is subtracted again, only to be added later when other phases have been subtracted. Controlling this cycling presents an algorithmic challenge without a unique solution. For this reason, we prefer the most gradual possible approach to changes in the species present.

Many other algorithms for minimizing  $\mathcal{G}$  have appeared in the literature and a comparison of their relative performance is beyond the scope of this paper. A summary of early work focused primarily on ideal solution and on systems of gases and pure solids appears in (Smith & Missen 1982). The development of our method draws most extensively from that of Harvie *et al.* (1987), who however use QR, rather than SVD decomposition. We prefer the SVD method because it yields more powerful and readily interpreted diagnostics

on the solution space. Harvie *et al.* (1987) show how the method can be extended to include other forms of constraint, for example, charge balance constraints that are important for modeling aqueous solutions. Ricard *et al.* (2005) have adopted a similar strategy, though with somewhat different methods for finding the vectors that span the null space and for treating phase addition and subtraction (Matas 1999). Eriksson (1971) apply mass balance constraints via the method of undetermined Lagrange multipliers, which does not reduce the dimensionality of the system as in our approach. The strategy of Ghiorso (1994) differs from ours in that for their application, one phase is always present (liquid), simplifying considerations of phase addition and removal, whereas in our application no phase is always present. The method of Ghiorso (1994) was generalized to subsolidus assemblages by Asimow & Ghiorso (1998). Bina (1998) used simulated annealing rather than the conjugate gradient or quasi-Newton scheme. Karpov *et al.* (1997) used a convex programming method. Connolly & Kerrick (1987) introduced the use of pseudocompounds: piecewise linear representations of compositional space, in order to increase the efficiency of the solution (Connolly 1990, 2005). This algorithm is implemented in the widely used PERPLEX package (PERPLEX 2010), which includes an option to use several previous versions of our thermodynamic model and parameterizations (Stixrude & Lithgow-Bertelloni 2005a, 2007; Xu *et al.* 2008), a combination that has been used to study mantle structure (Cobden *et al.* 2009; Khan *et al.* 2009) and dynamics (Nakagawa *et al.* 2009).